

Testing the strength of thin glass

Francisco Esteves de Oliveira Santos

Thesis to obtain the Master of Science Degree in
Civil Engineering

Supervisors:

Prof. Dr. ir. Pieter Christiaan Louter (TU Delft)

Prof. Dr. João Pedro Ramôa Ribeiro Correia (IST)

Examination Committee

Chairperson: Prof. Dr. José Joaquim Costa Branco de Oliveira Pedro

Supervisor: Prof. Dr. João Pedro Ramôa Ribeiro Correia

Members of the Committee:

Prof. Dr. Fernando António Baptista Branco

Prof. Dr. Luís Manuel Calado de Oliveira Martins

April 2017

The research hereby presented was developed
in collaboration with Delft University of Technology.



Abstract

Structural applications of glass are becoming increasingly more common, diverse and bold. Thin glass is a recent glass category, currently widespread in mobile devices and with great potential for applications in buildings due to its remarkable developments in strength, flexibility and dimensions available. However, there is neither a standard method able to determine its strength nor experimental data available on its mechanical behaviour.

In this context, experimental and numerical investigations were developed with two main goals: (i) to design or adapt setups to efficiently test the strength of thin glass and propose a new standard test to be used in structural design, and (ii) to characterize thin glass by using those tests, focusing on the ultimate strength and on particular behavioural aspects each test reveals more clearly. For this purpose, a set of non-destructive and destructive tests was carried out and a new test was proposed.

Two non-destructive tests were investigated: the tin side detector test and the scattered light polariscope test. Concerning the first test, the equipment applied was found to be unsuitable for this kind of glass. The second test indicated much lower surface stresses than those reported by the producers of the thin glasses tested and those measured in the destructive tests.

For destructive testing, another two tests were designed and assessed: the in-plane four-point bending test and the buckling test. While the first was prone to many geometrical instabilities, the second was able to cause failure of thin glass specimens, providing results for its strength, namely a lower bound imposed by the setup of 394 MPa (characteristic value) and 485 MPa (average value). In fact, the actual glass strength is expected to be significantly larger.

Finally, based on the difficulties encountered in the destructive tests performed, a tension test was proposed and numerically investigated, revealing many potential advantages compared to the former in terms of quality of results and possibility of standardization.

Keywords: thin glass; strength; non-destructive testing; destructive testing; numerical modelling.

Resumo

As aplicações de vidro estrutural são cada vez mais comuns, variadas e audazes. O vidro fino é uma nova categoria, presentemente utilizada em dispositivos móveis e com grande potencial para aplicações em edifícios, devido aos desenvolvimentos em termos de resistência, flexibilidade e dimensões disponíveis. Contudo, não há ensaios normalizados que permitam determinar a sua resistência, nem dados experimentais disponíveis sobre o seu comportamento mecânico.

Neste contexto, foi desenvolvido um estudo experimental e numérico com dois objetivos principais: (i) desenvolver ou adaptar ensaios para testar a resistência do vidro fino e propor um novo ensaio normalizado, cujos resultados possam ser utilizados em projetos de estruturas, e (ii) caracterizar o vidro fino recorrendo a esses ensaios, focando na resistência última e nos aspetos comportamentais que cada ensaio revela mais claramente. Com estes propósitos, foi realizado um conjunto de ensaios não-destrutivos e destrutivos e foi proposto um novo ensaio.

Foram estudados dois ensaios não-destrutivos: o *tin side detector test* e o *scattered light polariscope test*. Relativamente ao primeiro ensaio, concluiu-se que o equipamento utilizado não é apropriado para este tipo de vidro. Os resultados do segundo ensaio indicaram tensões superficiais com uma magnitude bastante menor do que o reportado por produtores e obtidos nos ensaios destrutivos.

Nos ensaios destrutivos, foram desenvolvidos e analisados dois ensaios: ensaio de flexão em quatro pontos no plano e ensaio de encurvadura. Enquanto o primeiro se revelou sujeito a muitas instabilidades geométricas, o segundo forneceu resultados sobre a resistência e o colapso do vidro fino, nomeadamente fornecendo um limite inferior para a resistência (imposto pelo próprio *setup*) de 394 MPa (valor característico) e 485 MPa (valor médio). Efetivamente, espera-se que o valor atual do vidro seja significativamente maior.

Finalmente, com base nos ensaios anteriores, foi proposto e investigado numericamente um ensaio de tração, que revelou bastantes vantagens potenciais sobre os ensaios destrutivos anteriores, em termos de qualidade de resultados e possibilidade de ser adotado como referência.

Palavras-chave: vidro fino; resistência; testes não destrutivos; testes destrutivos; modelação numérica.

Acknowledgements

The work hereby presented was developed at Instituto Superior Técnico (IST) in collaboration with Delft University of Technology (TU Delft). There are many people whose help was invaluable to develop this work; to all of them I express my gratitude:

To my supervisor at TU Delft, Professor Christian Louter, for his guidance and suggestions, and for providing me with the conditions to perform the experimental work in such an innovative field;

To my supervisor at IST, Professor João Ramôa Correia, for his exceptional dedication and availability, friendly and pragmatic advice, which was vital to improve the quality of the work hereby presented;

To Professor Frederic Veer, for his experienced suggestions and his help in the experimental work;

To Paul Vermeulen, for his suggestions, enthusiasm and guidance setting the strain gauges system;

To Dr. Luís Valarinho, for his friendship, availability and interesting discussions on the topic of structural glass;

To Asahi Glass Co. (AGC) for providing the samples of Leoflex thin glass for testing;

To Siim Hödemann, from the University of Tartu, Estonia, for the information provided regarding tests with SCALP.

Finally, my deepest gratitude to my family and friends for their irreplaceable support.

Contents

1. Introduction.....	1
1.1. Context	1
1.2. Motivation and objectives	1
1.3. Methodology and structure of the document.....	3
2. State of the art	4
2.1. Introductory remarks	4
2.2. Evolution of glass chemical composition up to thin glass	4
2.2.1. Soda-lime glass	4
2.2.2. Aluminosilicate glass.....	6
2.3. Production techniques	6
2.3.1. Float and micro-float processes.....	7
2.3.2. Overflow-fusion process	8
2.3.3. Down-draw process	8
2.4. Glass temper	9
2.4.1. Thermal temper	9
2.4.2. Chemical temper.....	10
2.5. Commercially available thin glass.....	11
2.6. Applications	12
2.7. Testing the strength of glass.....	14
2.7.1. European norm: EN ISO 1288	14
2.7.2. Studies on testing the strength of thin glass	17
2.7.3. Other tests for thin glass	20
2.8. Concluding remarks.....	21
3. Research program.....	22
3.1. Objective of the research program.....	22
3.2. Overview of research program.....	22
3.3. Materials	23
3.4. Concluding Remarks	25
4. Non-destructive testing.....	26
4.1. Introductory remarks	26
4.2. Tin side detector test	26
4.2.1. Objectives	26
4.2.2. Methodology	26
4.2.3. Results.....	27
4.3. SCALP test	27
4.3.1. Objectives	27
4.3.2. Test principle	28
4.3.3. Scattered light method.....	29

4.3.4.	Methodology	30
4.3.5.	Preliminary tests	31
4.3.6.	SCALP test results.....	31
4.4.	Concluding remarks.....	34
5.	Destructive testing	35
5.1.	Introductory remarks.....	35
5.2.	Assessment of in-plane four-point bending behaviour	35
5.2.1.	Objectives and methodology.....	35
5.2.2.	Experimental tests	36
5.2.2.3.	Experimental results	39
5.2.3.	Numerical analysis.....	41
5.2.4.	Proposed setup.....	48
5.3.	Assessment of buckling behaviour in compression	49
5.3.1.	Objectives	49
5.3.2.	Test setup	50
5.3.3.	Preparation of the tests.....	51
5.3.4.	Experimental results	54
5.3.5.	Numerical analysis.....	60
5.3.6.	Analytical assessment	65
5.3.7.	Proposed setup.....	66
5.4.	Proposal of a new test to assess the strength of thin glass: tension test	68
5.4.1.	Motivation	68
5.4.2.	Objectives of the new proposed test.....	68
5.4.3.	Description of the test method	69
5.4.4.	Numerical assessment of the test.....	70
5.4.5.	Summary	74
5.5.	Concluding remarks.....	74
6.	Conclusions and future developments.....	75
6.1.	Conclusions	75
6.2.	Future Developments	78
7.	Bibliography.....	80
	Appendix	85
A.	Specifications for commercial thin glass.....	85
A.1.	AGC Leoflex™ glass	85
A.2.	SCHOTT Xensation® glass	87
B.	SCALP – Preliminary tests.....	88
C.	In-plane four-point bending test.....	91
C.1.	Detailed analysis of the results for the first millimetres of deformation	91
C.2.	Numerical analysis with single line of nodes as lateral support	91
C.3.	Numerical analysis of lateral instability with aluminium – setup 3.....	93

D. Buckling test	94
D.1. Detailed analysis on the first millimetres	94
D.2. Video frames of the buckling test.....	95
E. Tension test	97
E.1. Glass adhesives: DYMAX Ultra Light-Weld® 431	97
E.2. Analysis of the principal stress in the glue	98

List of figures

Figure 1 – Principle of the standard float process (source: Schneider, 2015)	7
Figure 2 – Corning’s overflow-fusion process (source: Corning)	8
Figure 3 – SCHOTT’s down-draw fusion process (source: SCHOTT).....	9
Figure 4 – Ultra-thin glass on a roll (source: SCHOTT).....	9
Figure 5 – Comparison of the fracture pattern: annealed glass (1), heat strengthened glass (2), fully tempered glass (3) and structural implications (4) (source: Haldimann, 2006).....	10
Figure 6 – Comparison of the stress profiles obtained by thermal and chemical tempering. (source: Haldimann, 2006)	10
Figure 7 – Cold-bent thin glass elements, render (source: Leoflex brochure)	13
Figure 8 – Operable canopy composed of conical elements made with Gorilla Glass (source: Neugebauer, 2015)	13
Figure 9 –Illustration of several modes to bend a thin glass element to use in an adaptive façade (source: Silveira, 2016).....	14
Figure 10 – Render from design element developed for adaptive façades (source: Silveira, 2016).....	14
Figure 11 - Coaxial double ring test setup (source: EN 1288-2).....	16
Figure 12 - Radial and tangential stresses when loaded – small deformations (source: EN 1288-2)...	16
Figure 13 - Radial and tangential stresses when loaded – large deformations (source: EN 1288-2) ...	16
Figure 14 – Four-point bending test setup (source: EN 1288-3).....	17
Figure 15 – Channel shaped glass testing with four-point bending setup (source: EN 1288-4)	17
Figure 16 – Cross section of specimen (source: EN 1288-4)	17
Figure 17 - Coaxial double ring test R105	18
Figure 18 - FE simulation of the test with R 105 revealing the nonlinear effects (source: Neugebauer, 2016).....	18
Figure 19 - Experimental test of four-point bending in 2,00 mm thin glass with strength of 120 MPa (source: Holzinger, 2011)	19
Figure 20 – Horizontal force at supporting rollers due to large deflections (source: Maniatis et al., 2014)	19
Figure 21 – Scheme for the multiple-point bending setup (source: Siebert, 2013)	19
Figure 22 – Illustrative stresses developed on top and bottom surfaces (source: Siebert, 2013).....	19
Figure 23 – Buckling test setup (source: Spitzhüttl et al., 2014).....	20
Figure 24 – Comparison of numerical and experimental results (source: Maniatis et al., 2014).....	20
Figure 25 – Plot of the distribution of the main stresses with two FE softwares (source: Spitzhüttl et al., 2014).....	20
Figure 26 – Samples of aluminium (back) and Leoflex™ glass (front)	24
Figure 27 – Xensation® samples, 0.70 and 0.55 mm thick	24
Figure 28 – Marked corner on Leoflex™ samples.....	24
Figure 29 – Digital calliper measuring Leoflex™ height	24
Figure 30 - Scheme of the measurements: thickness and height.....	24

Figure 31 – Curvature radius as a function of the surface stress and specimen thickness, detail with critical area ($E = 74\text{GPa}$)	25
Figure 32 – Tin side detector, front and back side.....	27
Figure 33 – “Through glass” or “bottom side” testing (source: C.R.Laurence Co., Inc.)	27
Figure 34 – “Top side” method (source: C.R.Laurence Co., Inc.).....	27
Figure 35 – The three SCALP tests carried out – summary of goals and focus of the readings done..	28
Figure 36 – Side, profile and top view of the SCALP working principle (adapted from Aben et al., 2008)	29
Figure 37 – SCALP-05, front and bottom view	31
Figure 38 – Example of a reading, focusing on the immersion oil	31
Figure 39 – Surface stress and depth of layer along the whole length of the plate	32
Figure 40 – Detail of the video focused on the entrance spot of all readings	32
Figure 41 – Scheme of the stress results (MPa) with respective standard deviations and DOL (μm) for the area test.....	33
Figure 42 - SCALP tests on SCHOTT samples: a) to e) stress distribution (y-axis) vs. depth (x-axis) for different thicknesses and f) picture of measurement	33
Figure 43 – Setup of the in-plane four-point bending test used in all iterations, front and side view, no lateral constraint depicted.....	36
Figure 44 – Successive modifications introduced on the setup and results of preliminary tests.....	37
Figure 45 – In-plane four-point bending setup, front and side view, with focus on a) loading and b) lateral profile.....	39
Figure 46 – Force-displacement graph for all preliminary tests	40
Figure 47 – Glass plate after breakage, with marks on the supports (blue) and loads (red)	40
Figure 48 – Detail of a flaw on the edge of the sample (left tested and corresponding cracking pattern (right)).....	41
Figure 49 – Overview of the set of analyses comprised in the numerical study regarding goals and lateral boundary conditions.....	41
Figure 50 – Scheme of a plane stress element (source: DIANA)	42
Figure 51 – 2D model with plane stress elements.....	42
Figure 52 – Results of the numerical tests compared with the last preliminary tests (samples AL8 and GLASS)	42
Figure 53 – Comparison of behaviour of glass and aluminium (AL150 $\sigma_y=150\text{MPa}$) at 5,0 mm of displacement	43
Figure 54 – Comparison of the principal stresses S_1 due to one-point (fixed connection) and two-point loading (cylindrical).....	43
Figure 55 – Total applied force and maximum principal stress S_1 vs. cross-head displacement for 3- point and 4-point bending and experimental results for glass.....	43
Figure 56 – Scheme of the forces and bending moments supported in a curved shell element (source: DIANA)	44
Figure 57 – Nodes and internal axes in a Q20SH element (source: DIANA).....	44

Figure 58 – Model with shell elements and with supports in the out-of-plane direction: only outer supports (A) and both (B)	45
Figure 59 – Results for analysis 1: out-of-plane deformation and principal stress σ_1	45
Figure 60 – Comparison of the former plane stress elements analysis with analysis 1 (shell elements)	45
Figure 61 – Analyses 2 and 3: out-of-plane deformations and principal stresses on outer layers of the shell (cross-head displacement 12 mm)	46
Figure 62 – Analyses 2 and 3: out-of-plane deformations and principal stresses on outer layers of the shell (TZ=12mm at loads).....	47
Figure 63 – Analysis 4: out-of-plane deformation at 12 mm of vertical displacement and out-of-plane deformations vs. vertical displacement at loaded section.....	47
Figure 64 – Analysis 4: post-buckling principal stresses at 12 mm of vertical displacement and principal stresses in points highlighted with an arrow vs. vertical displacement at loaded section.	48
Figure 65 – Overall comparison of the applied force vs. vertical displacement at loaded sections.	48
Figure 66 – Principal stress vs. vertical displacement at loaded sections.	48
Figure 67 – Proposed setup for the in-plane four-point bending test, front and side view, with focus on the lateral constraint (red).....	49
Figure 68 – Pictures of the test setup with dimensions (mm)	50
Figure 69 – Buckling shape of (a) aluminium and (b) glass specimens.....	51
Figure 70 – Shatters of glass in the foil and roller	51
Figure 71 – Strain gauge and corresponding hardware and software	53
Figure 72 – Application of the strain gauges	53
Figure 73 – Two dispositions of cameras used to record the test.....	54
Figure 74 – Applied force in function of vertical displacement	55
Figure 75 – Stress at centre of outer surface (strain gauge) in function of the vertical displacement ...	55
Figure 76 – Vertical distribution of axial stress along the plate's longitudinal axis as a function of the vertical displacement (T3.V)	56
Figure 77 – Graphs of ultimate values of stress and force in function of the vertical displacement (T3.H)	56
Figure 78 – Stress rate of the overall test and detail of the near-breakage area	57
Figure 79 – Graphs of ultimate values of stress and force in function of the vertical displacement	58
Figure 80 – Parameter estimation plot for Weibull 2P distribution	58
Figure 81 – Weibull 2P cumulative distribution with estimated parameters ($\sigma_0=471,69$ MPa; $m=7,89$)	58
Figure 82 – Frames of GoPro video focusing on top roller - first seconds [camera 5]	59
Figure 83 – Frames of GoPro video focusing on top roller - collapse [camera 5]	59
Figure 84 – Shatters after breakage of glass: detail with a 6cm diameter lens cover and with a 1cm strain gauge.....	60
Figure 85 – Geometry, mesh and boundary conditions for the buckling model	60
Figure 86 – Study on the initial imperfection.....	61

Figure 87 – Out-of-plane deformation at the centre versus vertical deformation	61
Figure 88 – Side view of the plate deformation and 3D view of principal stress σ_1 along its vertical deformation	62
Figure 89 – Applied force vs. vertical displacement, comparison of numerical and experimental values	63
Figure 90 – Stress at centre of outer surface vs. vertical displacement, comparison with experimental values	63
Figure 91 – Ratio of numerical and experimental values.....	63
Figure 92 – Numerical and experimental vertical distribution of stress vs. vertical displacement; comparison and ratio (T3.V)	64
Figure 93 – Numerical and experimental horizontal distribution of axial stress vs. vertical displacement; comparison and ratio (T3.H).....	65
Figure 94 – Out-of-plane deformation as a function of the vertical displacement, comparison of numerical results and calculated results from experimental values.....	66
Figure 95 – Contact areas (red) between glass and metallic roller for different rotation angles	67
Figure 96 – Side view of the proposed roller with detail of insertion of neoprene band.....	67
Figure 97 – Tension test setup, front and side view	70
Figure 98 – Overall model, boundary conditions (bottom surface) and displacement loads (side view and perspective).....	71
Figure 99 – Deformation of the glue and development of the principal stresses vs. vertical displacement: side and front view ($\nu = 0,29$)	72
Figure 100 – Applied force vs. vertical displacement at the outer surface of the glue (half of cross-head displacement).....	72
Figure 101 – Evolution of centre (C) and edge (E) axial stresses in the glass, vertical profile ($\nu = 0,29$).....	73
Figure 102 – Evolution of centre (C) and edge (E) axial stresses in the glass, vertical profile ($\nu = 0,48$).....	73
Figure 103 – Evolution of centre (C) and edge (E) shear stresses in the glue, vertical profile ($\nu = 0,29$).....	73
Figure 104 – Evolution of centre (C) and edge (E) shear stresses in the glue, vertical profile ($\nu = 0,48$).....	73

Appendix

Figure A-1 Technical specifications for Leoflex™ glass produced by AGC (source: AGC Leoflex technical specifications).....	86
Figure A-2 - Detail of AGC Leoflex brochure: Depth of Layer (DOL) vs. compressive stress (CS) (source: AGC Leoflex brochure).....	86
Figure A-3 – Detail of AGC Leoflex brochure: material properties (source: AGC Leoflex brochure)	86

Figure A-4 – Technical specifications for Xensation® glass produced by SCHOTT (source: SCHOTT Xensation® technical specifications)	87
Figure B-1 - Screenshot of the video of reading 27 of Full-Length test, with DigInt activated [edited with +40% brightness]	88
Figure B-2 – Comparison of dispersion of the laser with the dry edge and with immersion liquid on the edge.....	89
Figure C-1 – Raw force-displacement graph of the in-plane four-point bending preliminary tests.....	91
Figure C-2 – Detail of the raw force-displacement graph of the in-plane four-point bending preliminary tests.....	91
Figure C-3 – Model with shell elements with supports in the out-of-plane direction, side and top view: only outer supports in one line of nodes	92
Figure C-4 – Absolute displacement for 100mm of vertical displacement at loads (TDtXYZ) [analysis 1,2,3]	92
Figure C-5 – Applied force and principal stresses vs. vertical displacement at loads for different finite elements, materials and loads applied	92
Figure C-6 – Distribution of the principal stress for the three layers of the shell element at 100 mm of displacement	93
Figure C-7 – Principal stress for the three layers of the shell element vs. vertical displacement at loads	93
Figure C-8 – Applied force vs. displacement at loads for aluminium	93
Figure D-1 – Detailed analysis on buckling: first millimetres of vertical displacement (instability)	94
Figure D-2 – Detailed analysis on buckling: first millimetres of vertical displacement with numerical analysis	94
Figure D-3 – Behaviour and collapse of glass – front view [camera 1].....	95
Figure D-4 – Behaviour and collapse of glass – side view [camera 2]	95
Figure D-5 – Behaviour and collapse of glass – top roller [camera 3]	95
Figure D-6 – Collapse of glass – bottom roller [camera 4].....	96
Figure D-7 – Original frames of GoPro video focusing on top roller - first seconds (fisheye effect not- corrected) [camera 5]	96
Figure D-8 – Collapse of the glass – visible the start at the rollers in the centre picture [camera: LG G4]	96
Figure E-1 – Product datasheet for DYMAX Ultra Light-Weld® 431 (source: DYMAX).....	97
Figure E-2 – Evolution of centre (C) and edge (E) principal stresses in the glue, vertical profile (Poisson ratio=0,29)	98
Figure E-3 – Evolution of centre (C) and edge (E) principal stresses in the glue, vertical profile (Poisson ratio=0,48)	98
Figure E-4 – Detail of the first nodes of the glued connection (d=60mm) revealing very high values of stress (plot $\nu=0,29$).....	99

List of tables

Table 1 – Comparison of the strength and depth of layer of the different types of glass (adapted: Haldimann et al., 2008; Schneider, 2015)	10
Table 2 – Summary of properties of commercially available thin glass (source: product sheets).....	11
Table 3 - Dimensions of loading ring and supporting ring (source: EN 1288-5)	17
Table 4 - Summary of tests and objectives of the research program	22
Table 5 - Summary of used samples: specifications and dimensions	23
Table 6 – Measurements of aluminium and glass samples: height and thickness according to position (in mm)	24
Table 7 – Results of SCALP readings for Xensation samples with 5 different thicknesses	34
Table 8 – Summary of the conditions for each of the preliminary tests and for the final test (yet to be performed).....	38
Table 9 – Maximum values of cross-head displacement, force and corresponding bending stress in all samples	40
Table 10 – Ultimate values of displacement, force, strain and stress for each test	57
Table 11 – Ultimate values of displacement, force, strain and stress for each test	72
Table 12 – Results of SCALP with varying gain	90
Table 13 – Indications from the preliminary tests regarding testing conditions.....	90

List of symbols and acronyms

<i>C</i>	Photoelastic constant	R_t	Relative retardation
DOL	Depth of Layer	σ	Principal stress
dof	Degree of freedom	σ_0	Characteristic stress (Weibull)
E	Young's modulus	σ_{bs}	Bending strength of glass
F	Applied force	σ_{sf}	Surface stress
G	Shear modulus	σ_a	strength of annealed glass
<i>n</i>	Refractive index	<i>t</i>	Thickness of the panel
<i>m</i>	Measure of strength variability	τ	Tensile compression shear
<i>k</i>	Empirical coefficient		glass-to-stainless steel

1. Introduction

1.1. Context

Nowadays, glass is nearly omnipresent, being applied in almost all industries. This is due to its transparency and aesthetic value, fairly low cost, chemical stability, ease to produce in a variety of shapes and sizes, many possibilities to adapt its composition and surface to the required properties, among many other advantages. Moreover, research activities are continuously striving to provide new and bolder uses for glass; also, current trends in various applications, for example in architecture and electronics, suggest that the influence of glass will be increasingly more important.

Regarding architecture and civil engineering, it is hard to conceive a building without using glass. While it is still mostly used in windows and covering of buildings, there has been a significant and successful effort to use glass as a load-bearing structural element and make use of its impressive strength in compression and improving resistance in tension. Currently, several investigations look into employing a wide range of glass elements effectively and safely. In fact, several studies, such as those by Louter (2011) and Valarinho (2016), extensively explore the possibilities of using glass beams; other ongoing investigations on structural glass revolve around a broad array of topics, such as glass columns (Nijse & Brincke, 2014), glass masonry (Oikonomopoulou *et al.*, 2014), curved applications (Timm & Chase, 2014), interlayers and lamination, adhesives and connections or fire behaviour.

Recently, driven by the demand for mobile devices, a new category of glass emerged: thin glass. This denomination usually refers to glasses with thicknesses below 2,00 mm (Albus & Robanus, 2015) and tempered to enhance the mechanical properties. The thermally tempered and, more notably, the chemically tempered thin glass is a material with very considerable potential, with some producers reporting strengths up to 900 MPa. The already widespread and ever growing use of this glass in many areas (particularly in electronics and mobile phones) has promoted a constant development in terms of quality, variety and dimensions. Over the last few years, an outstanding innovation has been revealed in the successive iterations of this type of glass product.

It seems likely that one of the next steps is the introduction of thin glass in structural and/or façade engineering, giving response to a trend towards lighter, more transparent and organic architecture. However, thin glass is a rather new and innovative material, whose composition, chemical tempering conditions and, thus, surface compressive stresses vary widely among manufacturers. Therefore, it is necessary to comprehensively investigate its behaviour prior to any real application in buildings.

1.2. Motivation and objectives

In general, the structural use of glass, as for any other material, depends significantly on its strength. The theoretical tensile strength of glass, based on molecular forces, can reach 32 GPa (Haldimann *et al.*, 2008); nonetheless, surface flaws compromise this value and in practice the actual strength is much lower. Strength values to be used in design are determined by applying standardized tests. These standard tests are employed according to the way glass will be loaded in real applications, which has

substantial impact on the strength value obtained. In fact, the function of the standards is to provide a strength value that matches the safety standards and is commonly accepted by the designers.

Thin glass is very strong and very thin, which raises problems when testing it. Its flexibility is the main obstacle: none of the current standard tests can deal with such large deformations. Not only do the geometric nonlinearities have a critical role in the distribution and calculation of stresses, but also the deformations are so considerable that they hinder the mechanical tests that run up to failure of the specimen. Considering the relevant methods to test the strength of glass, they all present significant limitations or difficulties when applied to thin glass: the coaxial double-ring tests develop considerable asymmetries and thus a non-uniform stress distribution; the four-point bending test is hampered as most of the chemically tempered specimens slip between the supports without breaking.

Currently, testing the thin glass material is mostly focused on its use in mobile devices, where the value of the ultimate strength does not have such an important role as in structural engineering. For those applications, several tests are performed (and widely publicized to a broad audience by the manufacturers, due to its visually impressive results), usually comparing the performance of thin glass with that of a sample of another type of glass: (i) impact tests, such as the ball drop or the ball launch test; (ii) tests to determine the hardness of the surface by means of micro-indentation, as Vickers or Knoop, or even by scratching it with common objects, like metallic keys; (iii) flexibility tests, forcing the buckling of the sample to assess the minimum curvature radius; (iv) three or four-point bending and ring-on-ring tests to determine the ultimate strength of the material.

It is important to note that none of the above-mentioned tests to determine the strength of glass is an accepted standard for structural design purposes and that they only stress very small areas, which are affected by significant size effects and thus not suitable for engineering applications.

To solve this problem, some studies suggest a few alternative methods, including the following: an analytically modified version of the standard four-point bending test; a buckling test, and a multiple-point bending. For the first two options, experiments were carried out using fully tempered thin glass (Spitzhüttl *et al.*, 2014; Maniatis *et al.*, 2014), but not chemically tempered glass. This dissertation describes these tests in more detail and why they are not fit to become a standard test.

After standardization, a sufficient number of tests has to be carried out to determine the value of the ultimate strength to be used in design calculations. Presently, there is a significant lack of data on the ultimate strength of thin glass, namely chemically tempered. Most of the values available are stated by the manufacturers and refer to the compressive stresses that the tempering is capable of introducing in the glass surface. Obviously, the absence of a standard to test this glass is a problem, but it is not the only reason for the scarce testing done so far: indeed, (i) it was only very recently that the dimensions of thin glass available became large enough for architecture/engineering applications, and hence adequate to be tested with that specific purpose; (ii) thin glass is expensive, particularly with those dimensions, making destructive tests very costly.

In this context, the experimental and numerical study presented in this dissertation had two main goals: (i) to design or adapt setups to efficiently test thin glass and propose a new standard test to be used in

structural design and, then, (ii) to characterize the thin glass material by using those diverse tests, focusing on the ultimate strength and on the particular behavioural aspect each test reveals more clearly. The two goals are very up-to-date and are quite appropriate to the present context of the use of thin glass, as there are no standard test setups or experimental data concerning chemically tempered thin glass; yet, such information is required to trigger its structural use.

1.3. Methodology and structure of the document

In order to achieve the above mentioned goals, a set of non-destructive tests (tin side detector test and Scattered Light Polariscope test) and a set of destructive tests (in-plane four-point bending test and buckling test) were experimentally conducted on commercially available thin glass samples. Based on the results obtained, namely in the destructive tests, an alternative test was proposed, with several potential advantages, in terms of area exposed to maximum stresses and possibility of standardization.

In chapter 2, the state of the art is presented, focusing on the current context of thin glass and on methods to test its strength. First, the background and present context of thin glass is given by explaining the composition of glass towards thin glass, the production and tempering processes, the properties of commercially available thin glass and its current and potential applications over a broad range of industries, and particularly for structural design. Then, regarding the topic of determining glass strength, the European standard EN ISO 1288, entitled “Glass in building - Determination of the bending strength of glass”, is reviewed and the methods to test the strength of regular glass are analysed. Finally, their possible use to test thin glass is discussed and alternatives reported in the literature are presented as well.

In chapter 3, the general goals of the research program developed in this dissertation are defined, as well as the experimental set of tests defined to achieve them. This set comprises both non-destructive and destructive tests, and the specific goals for each test are explained. The materials used in the research program are characterized, based on the specifications provided by manufacturers and also on the cross-section measurements.

In chapter 4, two non-destructive tests on chemically tempered thin glass are experimentally assessed. The goals of those tests are (i) to determine a value for the strength of thin glass; (ii) to study the strength distribution along the whole glass surface; (iii) to investigate the stress profile through the glass thickness, and (iv) to understand the influence of certain producing processes on the glass strength.

In chapter 5, two destructive tests on chemically tempered thin glass are experimentally and numerically investigated. In this case the goals are (i) to determine a value for the strength of thin glass; (ii) to study the lateral stability of thin glass panes; (iii) to test the edge strength, and (iv) to investigate the buckling behaviour of glass panels subjected to in-plane compressive loads and the corresponding stress distribution. Based on the results of these tests, a tension test is proposed and numerically investigated.

In chapter 6, the conclusions of the dissertation are summarily discussed and recommendations are given for future developments concerning the concepts approached in this work.

2. State of the art

2.1. Introductory remarks

Thin glass, or ultra-light glass, usually refers to glasses with thickness below 2 mm (Albus & Robanus, 2015), particularly in the range of 0,55 to 2,00 mm (Neugebauer, 2015). This thickness is the minimum for standard float glass production, which is the main reason for this categorization; yet, other thicknesses are proposed, such as 4 mm (Bos F. P., 2009) and 3 mm (Spitzhüttl *et al.*, 2014). In terms of composition, thin glass can be made of either soda-lime glass, borosilicate glass or aluminosilicate glass. Usually, these glasses are produced using either the micro-float, the down-draw or the overflow-fusion processes and then are tempered through thermal or chemical processes to enhance the mechanical properties. The combination of high strength and thinness results in a flexible material with a wide range of applications. Recently, there has been a growth of aluminosilicate chemically tempered glass as it presents the most interesting properties such as Gorilla Glass by Corning, Dragontrail and Leoflex by AGC and Xensation by SCHOTT.

Regarding strength, although brittle, glass is far from being a weak material. In fact, the theoretical tensile strength of glass, based on molecular forces, is extremely high and may reach 32 GPa (Haldimann *et al.*, 2008). However, many experimental studies show that the strength of glass is much lower, around 45 MPa (Bos, 2009). The extreme difference is caused by randomly distributed microscopic flaws in the glass surface, which became known as Griffith flaws that act as stress concentrators (Griffith, 1921). Therefore, to increase the strength of glass, it is required to enhance the surface quality or to treat it either thermally or chemically.

The purpose of the state of the art review presented in this chapter is to provide a better understanding of what is thin glass and how to test it. To do so, initially one presents the evolution of the chemical composition of glass, from the common soda-lime glass until the aluminosilicate glass, as well as the advantages of the latter to produce thin glass (2.2). Then, the production techniques are introduced, from the widespread float process to the more recent ones, more specific to thin glass, such as the micro-float, the overflow-fusion and the down-draw processes (2.3). The temper of glass is also approached, with focus on both thermal and chemical temper (2.4). An up-to-date summary of the properties of commercially available thin glasses manufactured by the major producers is provided (2.5). Next, some of the most prominent current and proposed applications of thin glass in several industries and in civil engineering are overviewed (2.6). To conclude, the test methods available to determine the strength of glass are studied; an overview of the European standards and of investigations on their suitability to thin glass is presented, together with some alternative testing protocols (2.8).

2.2. Evolution of glass chemical composition up to thin glass

2.2.1. Soda-lime glass

Glass has been used for many millennia. In pre-historic times, dark volcanic glass (obsidian), which occurs naturally from the rapid cooling of silica-based volcanic lava, was appreciated for its aptitude to produce sharp edges for blades or arrowheads. Glass manufacture is believed to have been discovered

by no later than 3000 BC, either as a by-product of metallurgy or from an evolutionary sequence in the development of ceramic materials, such as faience (Rasmussen, 2012). Although the technology was very rudimentary, it was continuously enhanced through improving chemical composition and production techniques, pushing forward the possible applications. In the following paragraphs, an outline of the evolution of the glass composition is presented to explain the contribution of each element.

Silica was soon identified as the main component to make glass. The sources of silica were typically beach sand or quartz pebbles, as quartz is the most common form of natural silica. While the fusion of such silica sources alone can result in a glass state, the temperature needed to melt silica is 1710°C, far too high to be reached with the techniques available in the early times (Phillips, 1941). Fused silica glass, also known as fused quartz or vitreous silica glass, is still used for high temperature applications.

By 2000 BC, it was discovered that the melting point of silica could be significantly lowered using a flux. The origin of the flux originates from metallurgy: a component is added to the smelting furnace to render the slag liquid at the smelting temperature (Lambert, 2005). The application of flux to the fusion of silica reinforces the theory of a strong connection between metallurgy and the origin of glassmaking (Raymond, 1986). The most common flux employed by ancient glassmakers was soda (sodium carbonate, Na_2CO_3) and its application could reduce the melting point of the silica to below 1000°C (Phillips, 1941).

However, the high solubility of the sodium present in this glass tended to make the resulting glass susceptible to deterioration when in contact with water, thus presenting a low chemical stability. To address this issue, a third element was required to act as a stabilizer for the glass product. It consisted in less soluble ions, like calcium or magnesium, which came from sources such as lime (calcium hydroxide, $\text{Ca}(\text{OH})_2$) or other mineral additives. The importance of lime, however, was not initially recognized and it was only by the seventeenth century that it started being intentionally added as a major constituent. Earlier, all calcium content in the ancient glasses was a result of impurities in either the silica or soda sources (Turner, 1956; Rasmussen, 2012).

However, ancient glass contained also a wide variety of unplanned impurities in the sand or flux, which affected the properties of the resulting glass in many ways, e.g., the colour of the glass. Iron, for example, is very common in the sand and is a very strong colouring agent (light blue-green). The careful selection of sand with low iron content and the addition of decolourizing agents, such as manganese dioxide or antimony, were essential to finally achieve colourless glass. However, despite colourless, most ancient glass contained air bubbles or undissolved material and thus was not as transparent as modern glass (Brill, 1963; Lambert, 2005)

As shown, the chemical composition of glass is quite complex and diverse, displaying a wide range of chemical and physical properties that are directly correlated to its possible applications. Moreover, the character of glass depends not only on the raw materials used, but also on the process and degree of heating, as well as on the method and rate of cooling hot glass, known as annealing (Rogers & Beard, 1948).

Regardless of the ratio of each component, the product of these three main constituents has thus been called soda-lime glass, with soda acting as the flux and lime as the stabilizer. The addition of combinations of soda and lime/calcium salts to the silica can result in an even greater reduction in the mixture's melting

point, with temperatures as low as 725°C: the triple eutectic¹ mixture results in a finished glass with composition of 73,5% silica (SiO₂), 21,3% soda (Na₂O) and 5,2% lime (CaO) (Lambert, 2005).

To sum up, the development of glass led to soda-lime glass, which is currently the most common type of glass for building applications, such as windows, and accounts for the vast majority of manufactured glass. The current composition contains magnesia (magnesium oxide, MgO) and alumina (aluminium oxide, Al₂O₃) to achieve a better chemical durability. It generally presents a composition of around 69-74% silica, 10-16% soda, 5-14% lime, 0-6% magnesia, 0-3% alumina and 0-5% others (De Jong *et al.*, 2011; EN 572-1, 2012). The standard EN 572-1 “Glass in building - Basic soda lime silicate glass products”, more specifically “Part 1: Definitions and general physical and mechanical properties”, provides insights into the chemical composition, the main physical and mechanical characteristics of this type of glass and defines the general quality control criteria applicable (EN 572-1, 2012).

Other types of glass were also developed for more specific purposes: sodium borosilicate glass, generally known as Pyrex; lead-oxide glass, generally known as crystal glass; oxide glass; and aluminosilicate glass, which is further studied in the following section.

2.2.2. Aluminosilicate glass

The aluminosilicate glasses are characterized by a much higher content in alumina (10% to 25%) and are divided in two types according to the other components of their composition.

The first type of glass of this type, alkaline earth aluminosilicate glass, has alkaline earth metals in its composition and is relevant for halogen lamps or other applications involving high temperatures.

The second type, alkali aluminosilicate glass, has a much broader application. It has a much higher content of alumina than soda-lime glass, typically 10% to 25% of the total, and over 10% lime (SCHOTT, 2014). Besides silica and the former two components, alkali aluminosilicate glass commonly includes magnesia, barium oxide (BaO) and boric oxide (B₂O₃) (De Jong *et al.*, 2011). Characteristic features of this glass are the high transformation temperatures and improved mechanical properties, such as hardness and scratch behaviour. One of the most relevant factors is the high content of alumina and lime that fosters a more effective ion-exchange (described ahead in 2.4.2) in order to improve the surface compressive strength, as stated by SCHOTT (2014) and Corning (2016).

2.3. Production techniques

The glass production techniques also underwent a remarkable evolution in terms of diversity and proficiency. From open pits to the iron blowpipe and pontil to the development of improved processes and furnaces, starting with those fired by wood and coal to contemporary all-oxygen-fired furnaces, the quality, sizes and possibilities of glass increased exponentially. The current section describes two current processes, the float (and micro-float), the overflow-fusion process and the down-draw process, as these are the main methods to produce either flat glass or thin glass.

¹ Triple eutectic is the mixture of greatest fusibility: a mixture whose melting point is lower than that of any other mixture of the same ingredients

2.3.1. Float and micro-float processes

Currently, the most common manufacturing process is the float process. It has made other flat glass manufacturing processes obsolete (e.g., the Libbey-Owens, Fourcault, and Pittsburgh processes), offering several advantages: from a better surface quality and a larger size of the panes to a much higher production rate and low requirements in terms of operational teams, this process revolutionized the glass industry (Haldimann *et al.*, 2008; De Jong *et al.*, 2011).

There are many stages in the float process, which are illustrated in Figure 1 and comprehensively described in Haldimann *et al.* (2008) and De Jong *et al.* (2011). To start with, the raw materials are mixed and melted at around 1550°C in large cross-fired furnaces or, more recently, in all-oxygen-fired furnaces. Molten glass is then conditioned and homogenised in the molten glass tank, cooling to 1100°C. Subsequently, molten glass flows into a bath of molten tin. The glass surface flows and smooths itself while on the tin bath, taking advantage of the excellent surface quality of molten tin and thus requiring no further polishing. Tin is used as flotation medium because of its density (5,9 g/cm³ compared with 2,2 to 2,5 g/cm³ for glass), surface tension (about 0,55 N/m), low melting point (232°C) and relatively low vapour pressure². The thickness of the float glass ranges from 2 mm to 25 mm and is controlled by the pull rate of the rollers. The glass gradually cools down and at about 60°C, by the time it leaves the bath, it is rigid enough to be handled without damage. The final cooling process to around 40°C occurs in the annealing *lehr* at a controlled and slow gradient to prevent thermal shocks or residual stresses. After annealing, the float glass is inspected by automated machines to ensure that imperfections are removed during cutting. Finally, glass panes are cut into a standard size of 6,00 m by 3,20 m and stored until they are further processed. The process described above is continuous.

For glasses thinner than 2 mm, the micro-float process was developed. It is adapted to aluminosilicate glass and it can produce glass with thicknesses down to 0,7 mm, although at a fraction of the output of the normal float process (Schneider, 2015). Figure 1 still applies, but temperatures are lower.

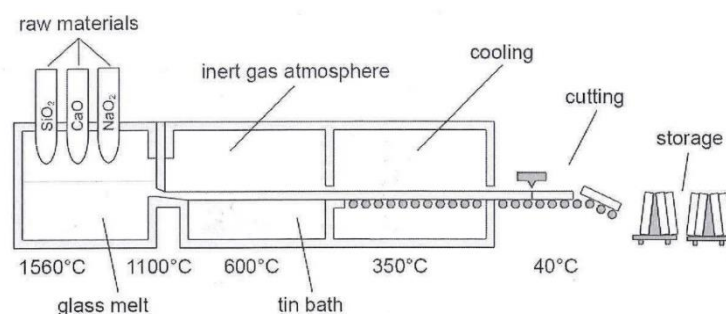


Figure 1 – Principle of the standard float process (source: Schneider, 2015)

It is important to mention that this method leaves some imperfections on the glass. Besides the rollers touching the surface of the glass, on the tin side there is some diffusion of tin atoms into the first 20 µm to 30 µm of the glass surface (Colombin *et al.*, 1977). This may have an influence on the behaviour of the surface when it is glued or laminated and the mechanical strength of the tin side has been found to

² The equilibrium vapour pressure is an indication of a liquid's evaporation rate, *i.e.*, the tendency of particles to escape from the liquid (or solid). Higher values correspond to more particles escaping.

be marginally lower than that of the air side. Still, this difference is not attributed to the diffused tin atoms but to the contact of the tin side with the transport rollers in the cooling area that introduces some surface flaws (Haldimann *et al.*, 2008). In addition, tin was found to hinder the chemical tempering process (Jiang *et al.*, 2012; Mognato *et al.*, 2016).

2.3.2. Overflow-fusion process

The overflow-fusion process and the down-draw process (see section ahead) are similar in principle, but differ slightly between the glass producers that developed them and are now proprietary processes. For both, the molten glass is pulled down, either by gravity or rollers. These two processes are the most common to produce ultra-thin glass down to thicknesses of 25 μm (SCHOTT, 2014)

The overflow-fusion process, or overflow-down-draw process, was designed by Corning around 1960, and it was recently reintroduced to produce special glass, such as thin and ultra-thin glass, providing an excellent untouched surface quality (Corning, 2016).

In fact, this recent manufacturing process has the key advantage of keeping the pristine surfaces untouched by molten tin. It is used for flat glass and allows to produce thicknesses in the order of the microns. This process is described in Figure 2, composed of relevant frames of a video of the process (Corning, 2016). The process starts after blending the raw materials at over 1000°C, the molten glass is poured into a trough, also known as “isopipe” (1). When the isopipe overfills, molten glass flows over from both sides (2) and converges at the bottom (3), where it is drawn down to form a continuous thin sheet of flat glass (4). After cooling, the glass is cut (5) and stored (6) automatically, untouched by human hands or anything else that could introduce flaws into the surface.

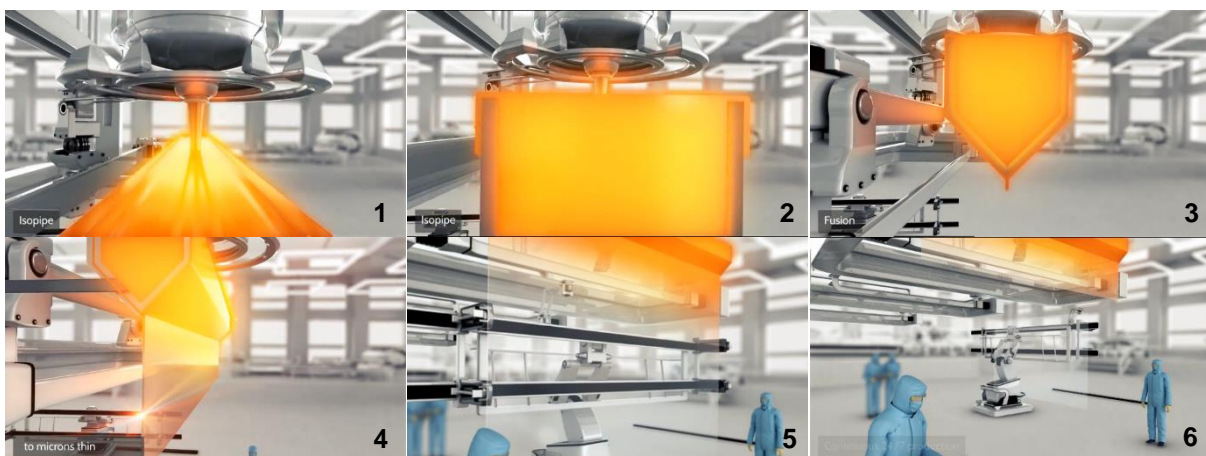


Figure 2 – Corning's overflow-fusion process (source: Corning, 2016 a)

2.3.3. Down-draw process

Other down-draw methods were developed by other producers. SCHOTT, for example, uses this process for very thin glasses with some modifications compared to the overflow-fusion process: the trough where the molten glass is poured has a slit at the bottom vertex and the molten glass is drawn down from there; in addition, the use of rollers and of an annealing *lehr* is required (Figure 3). The glass, if thin enough, is stored in rolls (Figure 4).

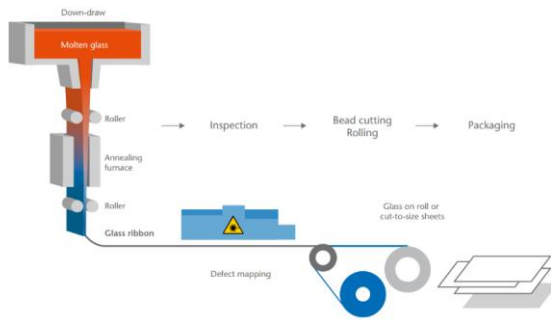


Figure 3 – SCHOTT's down-draw fusion process (source: SCHOTT, 2014)

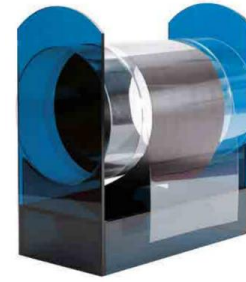


Figure 4 – Ultra-thin glass on a roll (source: SCHOTT, 2014)

2.4. Glass temper

Temper of glass is a controlled thermal or chemical treatment to increase its strength. The concept is to create a favourable residual stress field, introducing compressive stresses on the surfaces and tensile stresses in the core of the glass. The reason why this procedure succeeds is that the flaws on the glass surface can only grow if it subjected to effective tensile stress, while the glass core does not contain flaws and therefore offers good resistance to tensile stress. So, as long as the tensile surface stress due to applied actions is smaller than the residual compressive stress, there is no such effective tensile stress and consequently no crack growth (Haldimann *et al.*, 2008).

2.4.1. Thermal temper

The thermal tempering process consists in heating the float glass to approximately 620°C to 675°C, approximately 100°C above the glass transition temperature (T_g), and then cooling it rapidly with jets of cold air. When the temperature on the glass surface falls below T_g , the glass solidifies and relaxation stops immediately, which happens first at the surface of the glass. As its thermal shrinkage is resisted by the already solid surface, the cooling causes residual tension in the interior and compression at the surfaces with a depth of about 20% of the glass thickness. The maximum temper stress is achieved if the surface solidifies at the point of maximum temperature difference (Haldimann, 2006). Although ever more complex, thermal tempering can be applied to thin glasses down to 2 mm (Solinov, 2015).

In the literature, thermally tempered glass is categorized in two types: heat-strengthened glass (HS) and fully tempered glass (FT), according to the treatment they receive and consequently of the mechanical properties they display afterwards. The characteristics of these glass types is specified in the standards EN 1863-1, "Glass in building – Heat strengthened soda lime silicate glass", and EN 12150-1, "Glass in building – Thermally toughened soda lime silicate safety glass" (EN 1863-1, 2011; EN 12150-1, 2015).

Fully tempered and heat-strengthened glass undergo the same process, but heat-strengthened glass undergoes a lower cooling rate and, consequently, has a lower residual stress. The cooling rate has strong impact on the fracture pattern, and heat-strengthened glass breaks into much bigger fragments than fully tempered glass (Figure 5). Due to this large fracture pattern, heat-strengthened glass is commonly used in laminated glass elements to provide a balance in terms of pre- and post-breakage load-bearing capacity (Haldimann, 2006).

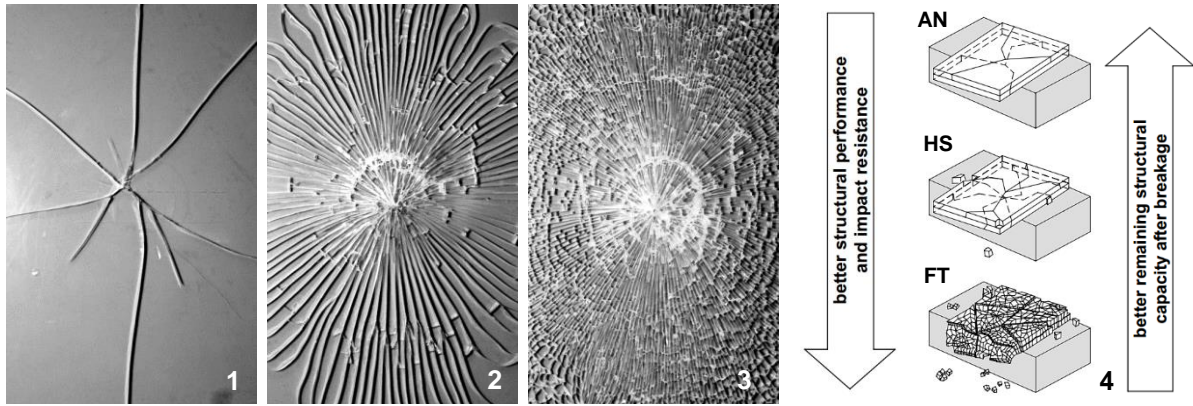


Figure 5 – Comparison of the fracture pattern: annealed glass (1), heat strengthened glass (2), fully tempered glass (3) and structural implications (4) (source: Haldimann, 2006)

2.4.2. Chemical temper

Briefly, the chemical tempering of glass is an ion-exchange process, replacing smaller ions at the surface of glass by larger ones and thus introducing a residual compressive stress. The process consists in submerging the glass in a K⁺ solution (potassium) at approximately 400°C, below the transformation of the glass, that causes the exchange of sodium ions in the glass surface by larger potassium ions (Solinov, 2015; Haldimann et al., 2008). The residual compressive stresses can go up to 800 MPa or even 1 000 MPa depending on the literature and producers, which provides a strength increase by a factor of 10 (Hundevad, 2014). These compressive stresses are introduced in a very thin layer at the surface, that can go from 40 to 100 µm (Schneider, 2015) – this measure is called depth of layer (DOL). Besides the much higher strength, cutting and drilling remains possible after chemical tempering.

Table 1 compares the strength and depth of layer of the different types of glass and Figure 6 illustrates the stress profiles developed through the thickness.

Table 1 – Comparison of the strength and depth of layer of the different types of glass (adapted: Haldimann et al., 2008; Schneider, 2015)

Type of glass	Residual compression (MPa)	Depth of layer
Annealed float glass	None	None
Heat-strengthened glass	40 to 80	20% of glass thickness
Fully tempered glass	80 to 170	20% of glass thickness
Chemically tempered glass	up to 800	25 to 50 µm

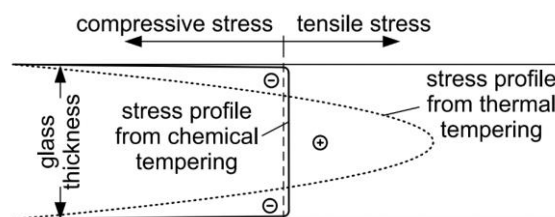


Figure 6 – Comparison of the stress profiles obtained by thermal and chemical tempering. (source: Haldimann, 2006)

There is a European standard about the chemical temper of soda-lime glass, EN 12337-1, “Glass in building – Chemically strengthened soda lime silicate glass”, which indicates a characteristic bending tensile strength of 150 MPa. However, currently, chemical temper is not common in buildings due to its

cost and limited dimensions, factors that will potentially fade away as the technology and processes evolve and become widespread and less expensive. Still, the chemical temper method had a very significant growth with the thin glass production, where it is most often applied (SCHOTT, 2014), being frequent to use aluminosilicate glass for tempering thin glass as the alumina content allows for a better and faster diffusion of the alkali-ions (Schneider, 2015). This advantage steered major thin glass producers to apply the chemical temper on aluminosilicate glass (e.g. SCHOTT, Corning, AGC, etc.).

2.5. Commercially available thin glass

The development of chemically tempered thin glass is directly connected to mobile devices. Nowadays, major companies like Corning, AGC or SCHOTT invest many resources in research for several fields, from the core glass for the devices to larger sizes for architecture or ultra-thin glasses for specialized applications. Table 2 summarizes the most relevant mechanical, thermal and optical properties of the commercially available thin glasses, all of them aluminosilicate chemically tempered thin glasses.

Table 2 – Summary of properties of commercially available thin glass
(source: product sheets, AGC 2012; SCHOTT 2014, Corning 2016 b)

Type	Property	Units	Soda Lime	Leoflex™	Dragon-trail™	Xensation	Gorilla4	Gorilla5	Gorilla Large format
Producer	-	-	-	AGC	AGC	SCHOTT	Corning	Corning	Corning
Mechanical	Density	g/cm ³	2,50	2,48	2,48	2,477	2,42	2,43	2,39
	Young's Modulus	GPa	73	74	74	74	65,8	76,7	68,0
	Shear Modulus	GPa	30	30	30	30	26,0	31,7	27,9
	Poisson's Ration	-	0,21	0,23	0,23	0,215	0,22	0,21	0,22
	Vickers Hardness before Chemical T.	kgf/mm ²	533	595	595	534	489	601	551
	Vickers Hardness after Chemical T.	kgf/mm ²	580	673	673	639	596	638	654
	Compressive Stress	MPa	-	800	n.a.	> 900	> 850	> 850	> 650
Depth of Layer	µm	-	> 35	n.a.	> 50	> 50	> 75	> 40	
Thermal	Softening Point ³	°C	733	831	831	880	912	884	896
	Annealing Point ⁴	°C	554	606	606	635	646	623	627
	Strain Point ⁵	°C	511	556	556	n.a.	596	571	573
Optical	Refraction Index	-	1,52	1,51	1,51	*1,506 1,514	*1,49 1,51	*1,50 1,51	*1,50 1,51
	Photoelastic Const.	nm/cm.MPa	25,6	28,3	28,3	29,2	30,3	30,1	n.a.
Application	-	-	civil eng.	civil eng.	devices	devices	devices	devices	civil eng.

*RI in the core of the glass, opposed to RI at the surface (below)

Source: all information retrieved from the specification sheets of the respective products; soda-lime glass values provided in the Leoflex brochure.

³ Softening point - viscosity drops to 10^{7.6} Poise; an unsupported glass will begin to sag.

⁴ Annealing point - viscosity drops to 10¹³ Poise; stresses relax in a matter of minutes.

⁵ Strain point - viscosity drops to 10^{14.5} Poise; stresses relax in a matter of several hours. ("Poise" is a measure of absolute viscosity; 1 Poise = 1 dyne-second/cm²).

2.6. Applications

The main driver of the development of thin glass up to now was its use in mobile devices, as mentioned before. The recent progress in thin glasses led to a considerable enhancement in their properties, namely higher strength, larger dimensions available, wider range of thicknesses and better impact and scratch resistance. This section approaches current or proposed applications of thin glass, first describing its main advantages, then its general applications and finally focusing on structural uses in buildings.

Thin glass presents a set of advantages such as (i) high tensile strength, many times higher than that of fully tempered glass and comparable to steel, (ii) lightness, as it has a fraction of the thickness of the other glasses, (iii) flexibility, allowing curved and dynamic/adaptive solutions, (iv) an impact and scratch resistant surface, and (v) a high quality completely transparent surface.

In addition to ever larger and resistant screens for electronic devices, such as smartphones and laptops, where Corning's Gorilla Glass alone has been designed into 4 500 000 000 devices, it is safe to predict that thin glass will have a wider range of functions in the future (Corning, 2015). There are many proposed applications and, to most, the value of strength is not the most relevant factor: as a cover to photovoltaic modules or solar heat collectors; as part of insulating glazing units, either triple glazing or quadruple glazing (MEM4WIN - ongoing project funded by EU involving thin glass (Jandl, 2015)); in platform doors of trains or subways; in interior architecture, etc. (Albus & Robanus, 2015; AGC). In addition, replacing one of the layers in a laminated panel with thin glass might bring substantial advantages as well: in the automotive industry, for example, it was announced recently that Gorilla Glass will be applied in the next Ford GT; these windows can weigh 20-60% less than conventional windows being far more resistant (Corning, 2015; Ford, 2015).

In terms of structural applications, three categories are presented: (i) used as a flat panel; (ii) used as a cold-bent curved panel, either on one axis or on two, by taking advantage of its flexibility; and (iii) adaptive or dynamic designs, in which the possibility to change its shape is leveraged. To design these applications, the value of the thin glass strength is essential and lamination is likely required.

Concerning the design of flat panels, thin glass is a valuable alternative when the weight of the structure is critical; examples are tensile façades or overhead glazing with significant spans. Instead of increasing the thickness of the laminated panels to resist the ever-growing loads imposed by the self-weight, applying a much lighter solution in thin glass can be the best option. However, the potentially large deformations must be duly considered (Hundevad, 2014).

Curved designs or membrane like structures are applications where thin glass adds even more value as bending regular glass is a complex and expensive task (Timm & Chase, 2014; Albus & Robanus, 2015). Thin glass allows cold bending, so it can be produced as a flat sheet and applied as curved, meaning there is no increase of costs to design curved elements (Figure 7). Furthermore, applying a curvature to a flat panel increases its (structural) stiffness and the forces inside the glass change from bending forces to in-plane forces. It is advised to apply a double curvature to prevent buckling, such as conical shapes (see example in Figure 8) (Hundevad, 2014). The high tensile strength together with

bent shapes provide high potential for use in membrane structures, such as roofs or stadium covers that can be conceived with a much higher freedom.



Figure 7 – Cold-bent thin glass elements, render (source: AGC 2012)

Finally, the properties of thin glass unlock a new application for glass: adaptive designs. Adaptive architecture is a multi-disciplinary field where buildings are designed to adapt to their environments or their inhabitants in order to improve their performance. This approach can be applied to a diversity of structural components, namely in (i) moveable elements, such as stadium roofs, canopies, interior partition walls, shop front façades, or (ii) adaptive façades.

As an example of the first set, a moveable canopy was developed by the company SFL Technologies GmbH. It was composed by two layers of 0,7 mm thick Gorilla Glass, each with 750 mm by 1250 mm, and laminated with a 0,38 mm PVB interlayer. The bonding material used was a 3M VHB tape to fix the glass to the frame; the tape was easy to fix to a curved surface and exhibited flexible elastic properties that allow the dissipation of concentrated loads. Besides allowing the flexible behaviour, it is estimated that the energy footprint of the production, tempering and shipping this thin glass elements was only 20% of a 6 mm two-layer laminated float glass, per unit of area (Hundevad, 2014).

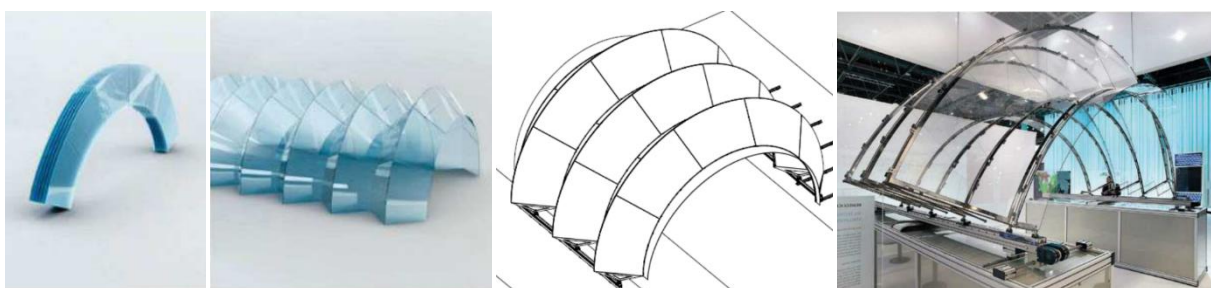


Figure 8 – Operable canopy composed of conical elements made with Gorilla Glass (source: Neugebauer, 2015)

For façades, usually the goal is to improve the ventilation and also to display dynamic aesthetics, although many other characteristics can be controlled. Silveira (2016) developed a comprehensive study on how to use thin glass in adaptive design in façades (Figure 9) and proposed a prototype with thin glass that was built as proof of concept and whose renders on a building are presented in Figure 10.

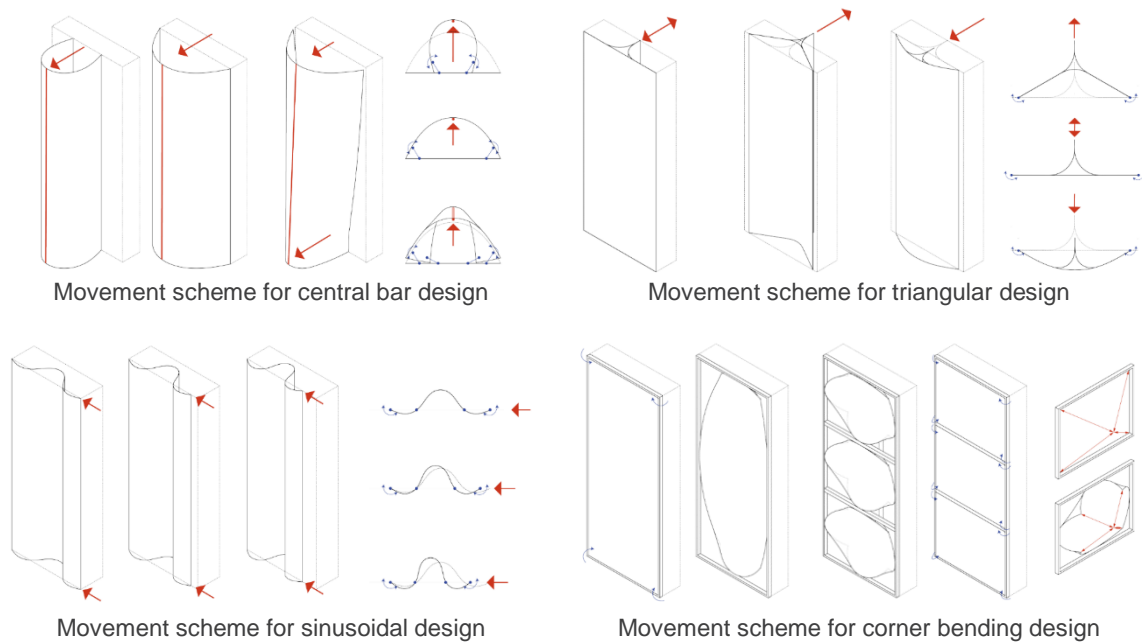


Figure 9 – Illustration of several modes to bend a thin glass element to use in an adaptive façade (source: Silveira, 2016)



Figure 10 – Render from design element developed for adaptive façades (source: Silveira, 2016)

To conclude, thin glass has high potential and in the upcoming years the development in the production techniques and a deeper knowledge about its behaviour will lead to larger sizes available and a reduced manufacturing cost, essential factors to promote a more generalized use.

2.7. Testing the strength of glass

2.7.1. European norm: EN ISO 1288

The European Standard EN ISO 1288, with the general title “Glass in building - Determination of the bending strength of glass”, refers the procedures for testing glass. This standard consists of five parts:

- Part 1: Fundamentals of testing glass;
- Part 2: Coaxial double ring test on flat specimens with large test surface areas;
- Part 3: Test with specimen supported at two points (four point bending);
- Part 4: Testing of channel shaped glass;
- Part 5: Coaxial double ring test on flat specimens with small test surface areas.

The EN ISO 1288-1 is structured around the factors that must be taken into account when testing glass, the justification for the different test methods and the limitations of those methods. This section approaches the concepts of testing glass and briefly describes the strength test standards it refers.

2.7.1.1. Factors to consider when testing the strength of glass

EN ISO 1288-1 specifies six factors that influence the strength of glass and that must be taken into account when testing, which are succinctly described in the following paragraphs.

The first factor is the **surface condition**. The standard states that, due to the brittleness of glass, any contact with a hard object can lead to surface damage in the form of ultra-fine, partly submicroscopic cracks and chips. The notch action caused by that surface damage has a major influence in reducing the mechanical strength, while the chemical composition, for example, does not play such an important role. Wiederhorn (1971) reinforces this premise, stating that the strength is deeply related to the perfection of the specimen's surface.

The second factor is the **rate and duration of loading**. It is important to introduce a few concepts about the propagation of cracks to understand when this factor is relevant. Crack propagation in glass occurs for a wide range of values of tensile stress: there is a lower limit to the stress intensity factor⁶ below which cracks do not propagate (Wiederhorn, 1971); then, at higher levels of stress intensity factor, there is some subcritical crack propagation that is influenced by humidity, temperature and chemical agents; finally, above a critical stress intensity factor the crack propagation is very rapid and leads to almost instantaneous failure. In the subcritical crack propagation state, the rate of load increase and the duration of static loading influences the bending strength. For prestressed glass, however, this time dependence is not relevant until the stress induced in the surface exceeds the residual compressive stress (Gy, 2013).

The third factor is the **area of the surface stressed in tension**. Statistically, the larger the test area, the greater is the probability of containing a large surface defect; consequently, for a larger area, a lower bending strength is expected. The influence of this parameter increases if there is a lower incidence of defects in the surface, such as in a new glass panel. EN 1288-1 compares the results of testing the same plate with EN 1288-2 (large test surface areas, maximum stressed area = 240 000 mm²) and EN 1288-5 (small areas, R45⁷ area = 254 mm², R30 area = 113 mm²) and the strength ratio between the smaller and larger ranges from 140% to 270% for R45 loading device or from 145% to 300% for R30 loading device.

The fourth factor is the **ambient medium**. Vandebroek (2014), among others, carried out a large experimental campaign to study the influence of humidity on the edge strength of glass. Vandebroek focused his tests on beams and confirmed that humidity has a significant influence on the strength of glass when the edge is stressed during a long period of time, in what is known as stress corrosion. Gy (2013) states that for glasses with residual compressive residual stresses, stress-assisted corrosion by ambient water cannot take place while the tensile stress does not exceed the residual compression. To conclude, the standard prescribes relative humidity levels in the range of 40% to 70%.

⁶ Stress intensity factor – term employed in fracture mechanics to predict the stress state near the tip of a crack caused by a remote load or residual stresses (Anderson, 2005)

⁷ R45 and R30 are loading devices, whose supporting ring has 45 mm and 30 mm, respectively – setup explained in 2.7.1 ii)

The fifth factor is **age**, *i.e.*, the time elapsed since the last mechanical surface treatment (by abrasion, etching, edge working, etc.). Glass is highly unlikely to be stressed directly after it has been treated, so the standard prescribes that it shall be conditioned for at least 24 h before testing.

The last factor, the sixth, is **temperature**. Although its effect is not very significant within the normal range of temperatures experienced by glass in buildings, the standard states that tests should be performed in a restricted range of temperatures.

The standard has constant specifications for the conditions to perform the tests: temperature of $23 \pm 5^\circ\text{C}$, relative humidity between 40% and 70% and stress rate of $2 \pm 0,4 \text{ N.mm}^2/\text{s}$.

To conclude, it is important to mention that the mechanical strength corresponds to a specified breakage probability and load duration. The characteristic values for thermally tempered glass relate to short time loading, 5% breakage probability and a confidence interval of 95%, according to the standards for thermally tempered glass EN 12150 and EN 1863. In the Italian CNR-DT-210, the strength of glass is associated to the statistical Weibull distribution (Feldmann & Kasper, 2014).

2.7.1.2. Strength tests prescribed in EN 1288

The standard EN 1288 describes four tests (Part 2 to 5) to determine the strength of glass, which are briefly described in the following paragraphs.

The part 2 describes the “coaxial double ring test on flat specimens with large test surface areas” (test setup in Figure 11), whose most singular feature is the elimination of edge effects as the maximum stress is limited to only a circular shaped area of the surface. Moreover, it has the advantage of loading the specimen in a uniform and directionally independent manner, meaning that the direction of possible surface defects is irrelevant.

The test is suited for relatively small deformations: the central surface area is subjected to uniform tensile stressing with equal components, radial and tangential (Figure 12). If the deflections increase, exceeding approximately half the thickness of the sheet, the loaded ring no longer displays an homogeneous stress (Figure 13). For those large deformations, the tangential and radial stresses behave differently and a simple calculation of the stresses is no longer possible: calculations according to linear bending theory would lead to too high stress results. In terms of dimensions, the radius of the supporting ring is $r_2 = 400 \text{ mm}$ and that of the loading ring is $r_1 = 300 \text{ mm}$, totalizing an effective surface area of $240\,000 \text{ mm}^2$. The minimum thickness of the specimen is 3 mm .

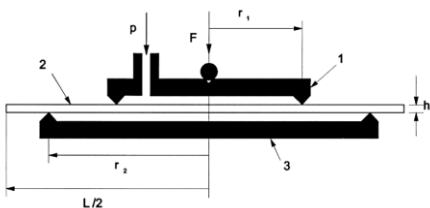


Figure 11 - Coaxial double ring test setup (source: EN 1288-2)

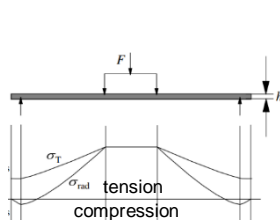


Figure 12 - Radial and tangential stresses when loaded – small deformations (source: EN 1288-2)

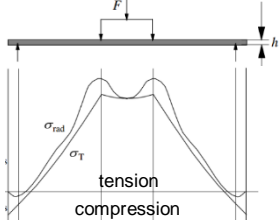


Figure 13 - Radial and tangential stresses when loaded – large deformations (source: EN 1288-2)

The part 3 describes the “test with specimen supported at two points (four point bending)”, whose setup is presented in Figure 14. The rationale for deciding between this test and the former one (EN 1288-2) is the relevance of the strength of the edge of the glass. In fact, the whole section at mid-span is subjected to stresses, including the edges. Moreover, Poisson’s effect generates an increase in the tensile bending stress developed at the lateral edges of the beam (Blank, et al., 1994). The plates are 1100 x 360 mm².

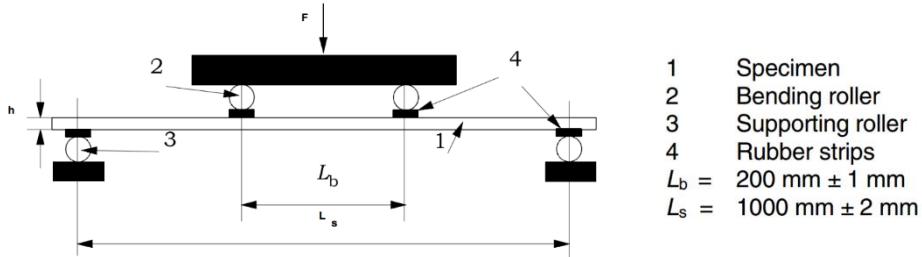


Figure 14 – Four-point bending test setup (source: EN 1288-3)

The part 4 describes the “testing of channel shaped glass”, which also employs a four-point bending setup (Figure 15). It is not particularly relevant for this dissertation, as it does not focus on flat plates but on channel plates, such as an U section (Figure 16).

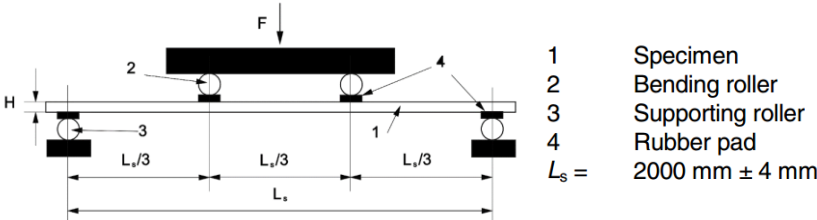


Figure 15 – Channel shaped glass testing with four-point bending setup (source: EN 1288-4)

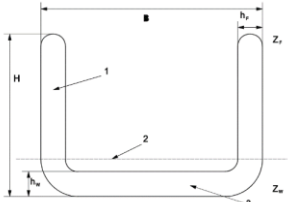


Figure 16 – Cross section of specimen (source: EN 1288-4)

The part 5 describes the “coaxial double ring test for small test surface areas”. The principle and setup are very similar to the test of part 2, with much smaller radii (Table 4). The maximum and minimum thicknesses are constrained to the bending strength of the glass and to the loading device chosen. Furthermore, the ratio between the deflection in the centre over the thickness of the specimen should not exceed 1,00.

Table 3 - Dimensions of loading ring and supporting ring (source: EN 1288-5)

Loading device	Radius of loading ring, r1 (mm)	Radius of supporting ring, r2 (mm)	Radius r3 or L/2 of specimen (mm)
R45	9	45	50
R30	6	30	33

2.7.2. Studies on testing the strength of thin glass

A few recent studies focused on the testing of thin glass, namely those of Siebert (2013), Spitzhüttl et al. (2014), Maniatis et al. (2014) and Neugebauer (2016). This section starts with a brief discussion on the limitations of the tests prescribed in EN 1288 when applied to thin glass. Then, it reviews these studies, namely the coaxial double ring tests, the pressure pad test, the four-point and multiple-point bending tests, and finally the buckling test.

Concerning the coaxial double ring tests, it is obvious that when applying the test meant for large surfaces (EN 1288-2), the deflections of thin glass specimens would be too high and quickly reach a nonlinear behaviour that would compromise the intended stress development. In fact, the standard itself is limited to thicknesses above 3 mm. Even though the test designed for small surfaces (EN 1288-5) is applicable to thinner glasses, the minimum thicknesses are 2,0 mm for R45 and 1,0 mm for R30, limited to a maximum stress of 100 MPa and a maximum deformation equal to the thickness of the specimen.

Furthermore, when testing thin glass with double ring tests, effects like geometrical nonlinearities, size effects or imperfections have to be taken into account (Neugebauer, 2016). Due to the thinness of the glass sheets, the effect of the geometrical nonlinearity is the dominant factor (Wilcox, *et al.*, 2013). Moreover, Siebert (2013) reinforces the fact that the results of this test are also compromised by the difference of the size of the glass samples compared to those usually produced for application in engineering.

Neugebauer (2016) did some tests with the loading device R105 (Figure 17), whose load ring has 35 mm of radius and whose supporting ring has 105 mm. The tests show clearly a large overall deformation and significant asymmetric deformations of the edges, as shown in the experimental test illustrated in Figure 17 and in the finite element model simulation of Figure 18. These can be caused by a not exactly centered loading ring or imperfections either of the setup or in the glass specimens. Also sample size effects were confirmed to be relevant, and an analytical manner to deal with them was presented in this study.

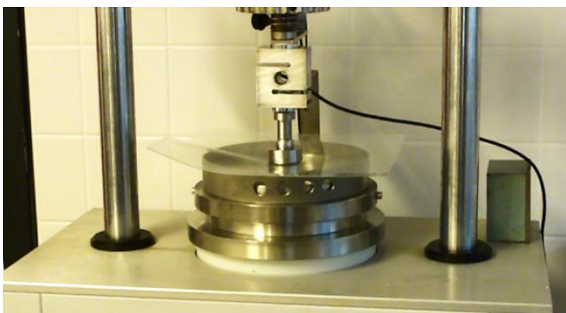


Figure 17 - Coaxial double ring test R105
(source: Neugebauer, 2016)

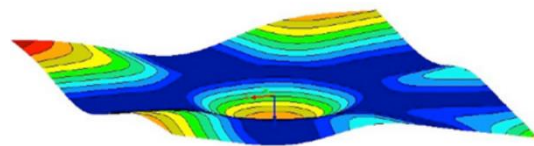


Figure 18 - FE simulation of the test with R 105 revealing the nonlinear effects (source: Neugebauer, 2016)

Neugebauer (2016) also proposes a related test where there is no influence of the edge: the “pressure pad on ring test”. The principle is similar to the double ring test but, instead of the loading ring, a pressure pad with a smaller but similar radius of the supporting ring applies the load; no dimensions are suggested in the article. The benefit is that the test is more stable and the effects of buckling are minimized. However, the stress inside the pressure pad is not uniform, requiring the use of an equation to estimate the effective area.

Regarding the four-point bending test, it is also clear that it is not a procedure intended for the very high deformations potentially involved when testing thin glass. At a first level, the Bernoulli theory cannot be applied anymore and even the EN 1288-3 deformation limits (given in percentage of the thickness) are easily exceeded, as demonstrated in Figure 19. Furthermore, due to the large deflections, horizontal forces are generated at the supports and these must be taken into account (Maniatis *et al.*, 2014;

Spitzhüttl *et al.*, 2014). Large deflections also produce the risk that the specimen will slide off the supports due to the bowstring effect: distance of rollers is constant but the extremities of the panes move inwards (Neugebauer, 2016).

Maniatis *et al.* (2014) proposed a modified analytical approach to this test to include the geometrical nonlinearities and experimented with fully tempered thin glass samples. The setup and procedure is the same, but the equations to determine the stresses include the influence of the horizontal loads developed at the supporting rollers and the mid-span deflection (Figure 20). Although this method offers advantages, such as a widespread equipment and a simple execution, it will fail to determine the strength if the sample simply slides through the supports. Therefore, for the ever increasing strength and thinner glasses, even the modified version is not applicable to test stronger thin glasses.

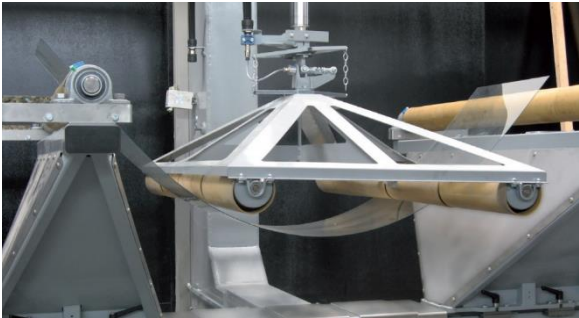


Figure 19 - Experimental test of four-point bending in 2,00 mm thin glass with strength of 120 MPa (source: Holzinger, 2011)

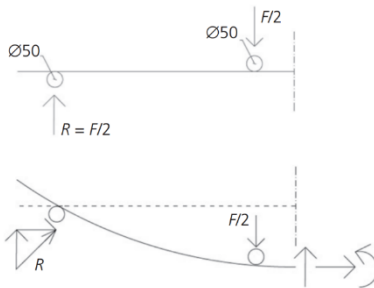


Figure 20 – Horizontal force at supporting rollers due to large deflections (source: Maniatis *et al.*, 2014)

Siebert (2013) and Neugebauer (2016) went a step further and discussed a modified test setup. The “multiple-point bending” consists, in these two examples, of four pairs of loading rollers (Figure 21), creating seven spans under tension combining the top and bottom surfaces (Figure 22); other configurations are possible, adjusting the number of spans and their length. One of the main drivers for this setup is the possibility to use the standard 1100 x 360 mm² plates and introducing maximum stresses on a considerable length but distributed over several smaller loading spans. Nonetheless, the setup was never validated experimentally and presents many difficulties, such as its sensitivity to imperfections in the geometry.

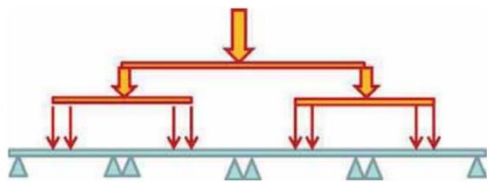


Figure 21 – Scheme for the multiple-point bending setup (source: Siebert, 2013)

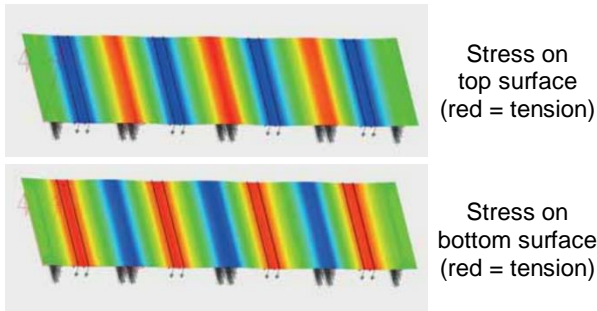


Figure 22 – Illustrative stresses developed on top and bottom surfaces (source: Siebert, 2013)

Finally, another test presented in all these four articles is the flexural “buckling test” or “bending by in-plane force”. The glass panel is supported vertically by two rollers that rotate around the minor axis of

inertia and is loaded by an in-plane force on the top; the force causes the buckling and an increasing out-of-plane deflection. To determine the maximum stress, the most important effect is due to the geometrical nonlinear deformation: a second order moment is created by the lateral deflection at mid-span, which is multiplied by the applied vertical force. The axial stress corresponding to this applied force divided by the cross-sectional area plays a minor role, as the Euler critical load is very low.

Using the buckling setup shown in Figure 23, Spitzhüttl *et al.* (2014) and Maniatis *et al.* (2014) carried out experimental investigations on fully tempered thin glass plates with dimensions of 1100x360 mm², together with numerical studies to assess the influence of the Young's modulus, the thickness and the Poisson's ratio. As depicted in Figure 24, the maximum vertical displacement experimentally attained was 75 mm, corresponding to a strength of around 125 MPa; the two samples tested presented somewhat different behaviours concerning the vertical displacement vs. axial stress: besides the significant differences in stress values, one of the samples presented an instabilization different to what was numerically predicted (Producer 2, in Figure 24). The studies did not provide the final value for the strength tested or the compressive surface stress of the glass samples employed. The numerical analysis was useful to understand the expected stress distribution on the test specimen, regarding both the stresses on the edges (higher than in the centre) and the effective area subjected to the maximum stress (Figure 25).



Figure 23 – Buckling test setup (source: Spitzhüttl *et al.*, 2014)

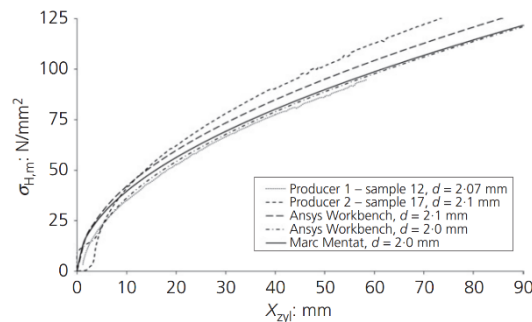


Figure 24 – Comparison of numerical and experimental results (source: Maniatis *et al.*, 2014)

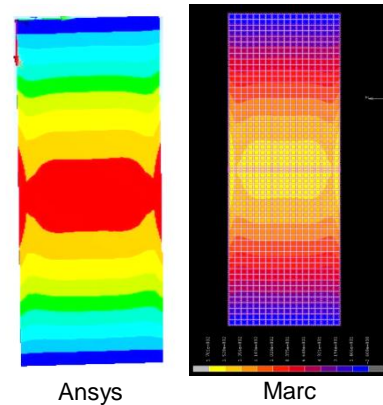


Figure 25 – Plot of the distribution of the main stresses with two FE softwares (source: Spitzhüttl *et al.*, 2014)

To sum up, there is an obvious lack of experimental tests in thin glass, both to investigate the testing methods in order to agree on a standard and, in a second phase, to reach a strength value to be employed in structural design. While the referred studies carried out the buckling test on fully tempered thin glass samples, the absence of literature is particularly evident in chemically tempered thin glass that is an even more demanding challenge due to the very high strength and flexibility expected.

2.7.3. Other tests for thin glass

Testing of thin glass focus mostly on its use in mobile devices. Therefore, the main concern has to do with determining its impact and scratch resistance and not its mechanical strength. Those tests are beyond the scope of this dissertation and therefore they are only briefly mentioned here. They include impact tests, such as the ball drop or the ball launch test; tests to determine the hardness of the surface with

microindentation as Vickers or Knoop, or even scratching it with common objects like keys; flexibility tests, forcing the buckling of the sample to assess the minimum curvature radius; and finally, abrasion tests.

On another note, some test method used for regular tempered glass are being adapted to study thin glass strength and its properties. Examples of these tests, with the particularity of being non-destructive, are the tin-side detector test or, more promising, tests based on the photoelasticity of glass; several adaptations of this principle are approached in more detail in section 4.3.

2.8. Concluding remarks

Thin glass experienced a remarkable development in the recent years and is now regarded as a material with very high potential for applications in civil engineering, among many other industries. In fact, if chemically tempered, it combines a strength similar to that of steel, a very low self-weight, the possibility to be cold-bent and transparency, among other features that make it a very interesting solution for flat, curved or even adaptive structural designs. However, a value for its design strength is still missing.

When studying the strength of thin glass, it is clear that the extraordinary mechanical properties it presents prevent the practical application of the standard methods used to test the strength of regular glass: the deformations are simply too large. None of the currently available methods is prepared for the geometrical nonlinearities that develop when testing such a thin and strong pane of glass. So far, tests specific for thin glass are focused on applications such as mobile devices, where the value of the strength is not so relevant and both stresses and sample size are quite different than for buildings.

In summary, a new standard for testing the strength of thin glass is required in order to trigger the use of thin glass as a structural element. Hence, new methods of testing must be designed and tested thoroughly to come up with a valid solution that offers coherent and insightful results through a standardisable methodology. While a few studies suggest some methods and even experiments on fully tempered samples, there is an evident lack of information regarding this topic. Furthermore, experiments about the strength of the (more challenging) chemically tempered thin glass were not yet reported in the literature.

3. Research program

3.1. Objective of the research program

The main goal of the research program consists of studying the mechanical behaviour and the strength of thin glass and to propose a set of experimental tests that can be used as a standard for the mechanical characterization of this material. Therefore, a research program comprising a set of non-destructive and destructive tests was carried out, focused on the ultimate strength of thin glass. Moreover, this diverse set of tests allowed to gain insights on the different properties and mechanical behaviour of this material, contributing to a deeper understanding on how to test it and on which applications it might prove useful.

3.2. Overview of research program

In order to reach the proposed goal, the tests to be performed should not have a very complex setup or methodology as that would complicate not only the correct replication of the tests but also their standardization. Therefore, the following set of non-destructive and destructive tests was planned: the tin side detector test and the Scattered Light Polariscope (SCALP) test (non-destructive); the in-plane four-point bending test and the buckling test (destructive tests). Table 4 summarizes the objectives of each test, which are briefly described in the next paragraphs and detailed in chapters 4 (non-destructive) and 5 (destructive).

Table 4 - Summary of tests and objectives of the research program

Test	Summary of objectives
Tin side detector test	a) verify if the tin side is still detectable after the ion exchange
SCALP test	a) study the residual stress at the surface b) study the residual stress distribution as a function of the depth c) analyse differences of residual stress on air side and tin side of the plate
In-plane four-point bending test	a) ultimate strength of the material, focusing on the edge b) lateral buckling behaviour
Buckling test	a) ultimate strength of the material b) buckling behaviour and flexibility

Both the SCALP test and the tin side detector tests provide some insights on the glass properties through the use of light. As non-destructive tests that are based on the optical properties of glass, they are performed before any of the other tests and with the glass plates as clean as possible. The goal of the tin side detector test is to verify if the tin is still detectable after the ion-exchange. With the SCALP test, one aims at studying the impact of the tin on the surface stress; in addition, this test has a broader objective: to verify the stress and its distribution on the whole surface of the glass, as well as how it varies along the glass thickness.

The remaining tests are performed until the failure of the material with the goal of determining the ultimate strength of glass; thus, they are referred as destructive tests. In addition to this main goal, the different setups provide a clearer understanding on certain behavioural aspects and properties of glass. The in-plane four-point bending test focus on the lateral stability and edge strength, which can be critical

points for certain applications where glass is loaded on its plane, like a beam. The flexural buckling test allows studying the buckling behaviour of glass panels subjected to in-plane compressive loads, providing valuable insights (e.g., for curved-glass applications). These tests complement each other, providing information about the strength and mechanical behaviour for diverse realistic applications.

3.3. Materials

This section presents the materials and samples used in the experimental program. It starts with an overview of the materials and their specification, which are grouped in three categories as displayed in Table 5. It is complemented with the use given to each material and the reasoning supporting it. Finally, the properties and geometric measurements made in some samples are presented.

Table 5 - Summary of used samples: specifications and dimensions

Material	Specification	Dimensions (mm)	Thickness (mm)
Thin glass	AGC Leoflex™	710x80	2,00
Thin glass	SCHOTT® Xensation®	Small (~70x40)	0,55; 0,70; 1,10; 2,00; 3,00
Aluminium	Not available	710x80	2,00

The AGC Leoflex™ thin glass, which is produced with AGC's micro-float process and designed for architectural applications, was the basis of the experimental testing due to its specimens' dimensions. These samples were employed in all tests. The other two materials – aluminium and the SCHOTT® Xensation® thin glass – were used as auxiliary or complementary material to the experimental analysis. Figure 26 is a side-by-side picture of a Leoflex™ and an aluminium sample. The properties of Leoflex™ were described in Table 2 (c.f. section 2.5) and in Appendix A.1. However, for all the analyses carried out in this research, either numerical or analytical, the properties used are hereby specified for ease and clarify the reading: Young's modulus, $E = 74$ GPa; shear modulus, $G = 30$ GPa, thus Poisson's ratio $\nu = 0,233$; refraction index, $RI = 1,508$ (better fit with experimental test, datasheet states $RI = 1,51$, see 4.3.5); photoelastic constant, $C = 28,3$ nm/cm.MPa (AGC, 2012).

The SCHOTT® Xensation® samples, produced with SCHOTT's micro-float process, were used in the tin side detector and SCALP tests to provide a comparison with different composition and thickness; also, the dimensions of the samples made of this material were not interesting for mechanical tests. Figure 27 shows two of the five samples. The Xensation technical specifications are available in the Appendix A.2.

The aluminium samples were used for preliminary tests, making use of a material with a similar Young's modulus to study the test setup and prevent setup flaws that would compromise the results and a sample of (more expensive) thin glass. However, its specific class was not provided by the supplier and there was no information about its Young's modulus and yield tension; therefore, the following average value for the Young's modulus and the following range for the yield tension (ASM International, 1997) were considered: Young's modulus, $E = 71$ GPa; yield tension, $\sigma_y(\text{plate}) = 125$ MPa to 615 MPa.

Regarding the geometry of the Leoflex plates, an important feature should be mentioned: only one corner has a particular cut at 45°, while the others are perpendicular (Figure 28). This is quite useful for systematic measurements and tests, being that mark the reference. To further study the Leoflex™ glass and aluminium plates that were subsequently subjected to mechanical tests, a digital calliper with precision of 0,005 mm was used. Figure 29 shows the measurement of one height. The scheme of the measurements is described in Figure 30, which emphasizes the marked corner as the reference.

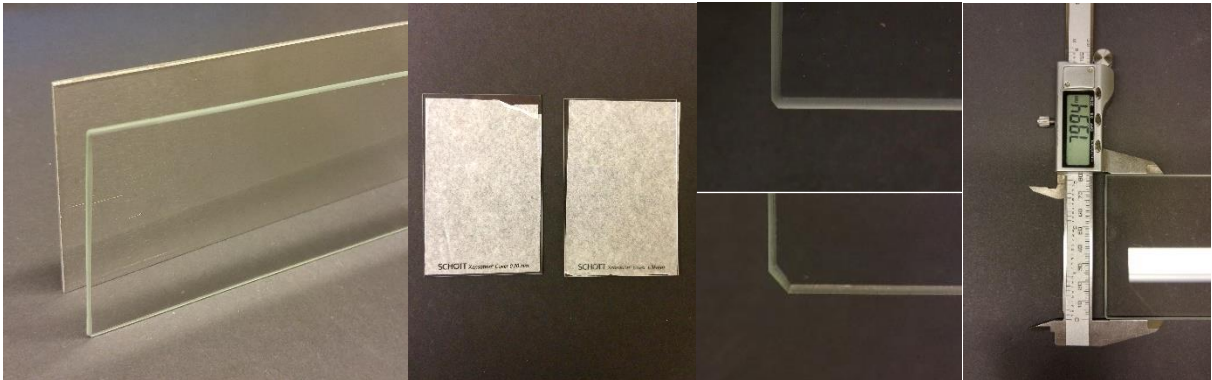


Figure 26 – Samples of aluminium (back) and Leoflex™ glass (front) Figure 27 – Xensation® samples, 0.70 and 0.55 mm thick Figure 28 – Marked corner on Leoflex™ samples Figure 29 – Digital calliper measuring Leoflex™ height



Figure 30 - Scheme of the measurements: thickness and height

The results of these measurements are presented in Table 6, indicating the average and the standard deviation. It shows that the dimensions of both aluminium and Leoflex samples are very precise, being the glass very slightly smaller than it was supposed and with a lower standard deviation than aluminium.

Table 6 – Measurements of aluminium and glass samples: height and thickness according to position (in mm)

Material	Parameter	height1	height2	height3	thickness1	thickness2	thickness3	thickness4
Aluminium 4 samples	Average	80,01	80,01	80,00	2,01	2,00	2,00	2,00
	St. Dev.	0,03	0,02	0,05	0,01	0,01	0,00	0,00
Glass 10 samples	Average	79,96	79,96	79,97	1,99	1,99	1,99	1,99
	St. Dev.	0,01	0,01	0,01	0,01	0,01	0,01	0,01

Based on the measurements reported above, the following section properties were considered, namely in the analytical calculations: height, $h = 80,00$ mm; thickness, $t = 2,00$ mm; around the major axis the inertia is $I = 85333,33$ mm⁴ and the section modulus is $W = 2133,33$ mm³; around the minor axis the inertia is $I = 53,33$ mm⁴ and the section modulus is $W = 53,33$ mm³.

There were 40 samples of Leoflex glass available with the aforementioned dimensions.

One very simple analysis concerning these thicknesses is the curvature radius (R) as a function of the ultimate strength (σ_{max}), elasticity modulus and specimen thickness (t), as given by equation (1):

$$\rho = \frac{1}{R} = \frac{M}{EI} = \frac{\sigma \cdot w}{EI} \xrightarrow{l=w \cdot 2/t} R_{min} = \frac{E \cdot t}{2 \cdot \sigma_{max}} \tag{1}$$

Figure 31 illustrates the relationship presented in equation (1) with the available glass thicknesses, highlighting the interval of compressive stresses that the producers state: for Leoflex, the compressive stress is over 800 MPa (AGC, 2012). For thin glass, the combination of such slim sections with strong resistances results in extremely low curvature radius. In fact, for the tested 2,00mm thick Leoflex samples, the ultimate curvature radius is between 120mm to 80mm, meaning a four-point out-of-plane bending test would have a maximum span of around 150 mm to 200 mm; for a thickness of 0,55 mm, that span would be about 50 mm. This simple analysis is enough to prove the standard four-point bending test described in EN 1288-3 (1000 mm of span, *c.f.* section 2.7.1) is not applicable to these values of strength in thin glass.

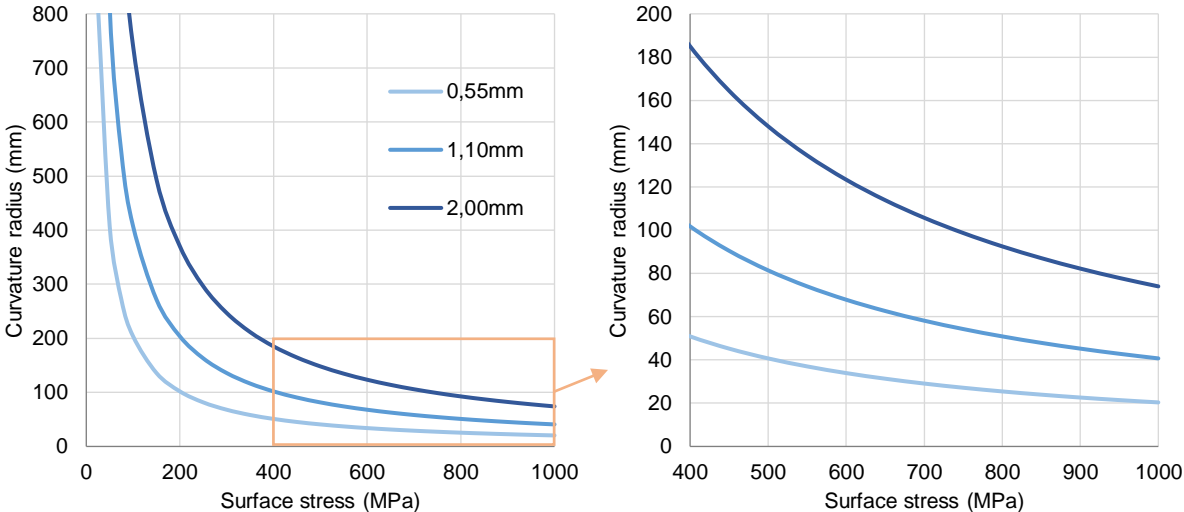


Figure 31 – Curvature radius as a function of the surface stress and specimen thickness, detail with critical area (E = 74GPa)

3.4. Concluding Remarks

In this chapter, the objectives of the research were discussed and an experimental program comprising both non-destructive and destructive tests was defined. The specific goals for each of the tests included in those two categories were also presented. Finally, the materials used in the research program were studied, presenting the relevant properties and the geometry measurements made on them, as well as a simple analysis to illustrate that such combination of strength and thickness cannot be tested with the regular methods.

4. Non-destructive testing

4.1. Introductory remarks

The non-destructive tests are a broad set of techniques used to assess the properties of a material or element without causing damage (Cartz, 1995). These techniques are a much more cost-efficient way of testing as they have the advantage of keeping the specimen unaltered after the exam, which is particularly important in the case of thin glass, because specimens with adequate dimensions are still very expensive.

In the case of the experiments performed, the tin side detector test and the SCALP test consist in emitting UV light and a laser beam, respectively. Although both tests are useful for studying the strength of thin glass, the data they retrieve is different: while the tin side detector test focus on detecting tin on one of the surfaces, the SCALP test can provide a stress profile through the thickness of the tested specimen.

4.2. Tin side detector test

4.2.1. Objectives

In the float or micro-float production processes (see 2.3.1), the side of the glass in contact with the molten tin is usually known as the “tin side”. After being removed, traces of tin or tin oxide deposited during the cooling stage can be found on this surface of glass. The other side is identified as “air side”.

The goal of this test is to verify if the tin side is still detectable after the ion exchange. As there is evidence that the tin might hinder the exchange of ions in the chemical temper (Jiang, et al., 2012), this is particularly important for studying the glass strength, despite this test not providing an ultimate value for this parameter. If indeed the tin was detectable, after labelling each side, that influence would then be studied with the SCALP test.

The principle of the test is simple and is exclusively applicable to glasses produced with the float or micro-float processes. The tin side detector emits a short-wave UV radiation that causes a visible fluorescence in the tin. The glass substrate does not transmit the UV light; therefore, if the detector is placed on the air side, the tin coating on the opposite side will not receive the energy.

4.2.2. Methodology

The test was carried out with a tin side detector, an equipment produced by C.R. Laurence Co., Inc., model TS1301 (Figure 32).

For security reasons, the use of UV blocking glasses is very important because although the light seems dim, the visible part is only a small fraction of the radiation emitted. Those security glasses are provided with the equipment and consist of lenses of simple glass that block the emitted light.

The following material was used in the test: a sample of 2,00 mm thick thin glass (AGC Leoflex); small samples of various thicknesses (0,55; 0,70; 1,10; 2,00 and 3,00 mm; SCHOTT Xensation); and a sample

of 10 mm thick float glass. All the glass samples were produced with float or micro-float processes. The test was performed in an underground room with all lights off.

Two methods were used. In the first method, known as *through glass testing* or *bottom side method*, the detector is placed on the side of the glass and one observes if either the shape of the UV lamp (air side) or a blur (tin side) is visible from the opposite side of the glass (Figure 33). The alternative method is the *“top side method”*, which consists in placing the detector on the top edge of the glass, tilting the glass and irradiating its side surface (Figure 34). If there is a glow on the surface, it is the tin side.



Figure 32 – Tin side detector, front and back side

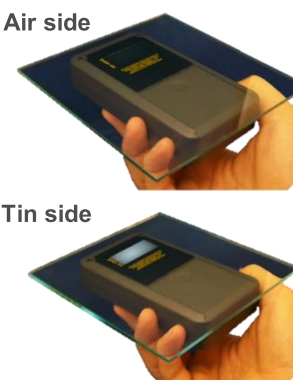


Figure 33 – “Through glass” or “bottom side” testing (source: C.R.Laurence Co., Inc.)

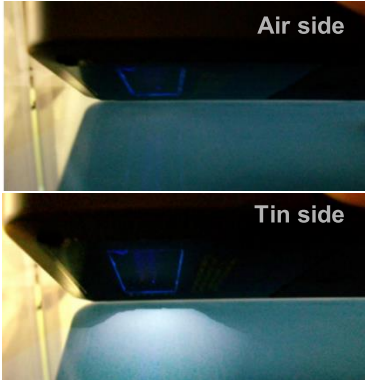


Figure 34 – “Top side” method (source: C.R.Laurence Co., Inc.)

4.2.3. Results

The first method used was the *“through glass testing”* one. On the thick float glass it was clearly distinguishable one side that glowed more and made the lamp light blurry (tin side) and other where the lamp was clearly visible, with little to no distortion (air side). However, in all the thin glass samples, it was impossible to detect any significant difference. The glass seemed slightly translucent with the same intensity for each of its sides and, due to its slimness, it was not possible to verify if one of the sides was glowing more than the other.

The *“top side method”* is more focused on the surfaces and the influence of the glass thickness is decreased. As expected, it provided good results for the thick float glass. However, this method also failed to provide convincing or clear results for the thin glass samples, as both sides were sort of translucent.

4.3. SCALP test

4.3.1. Objectives

The main goal of the SCALP test is to obtain the value of the stress at the surface of a glass plate and to study the stress distribution both along the area of the plate and as a function of the depth. This test is also used to study the influence of the air and tin sides on the surface stress, if previously identified.

The main advantage of the SCALP test is that it presents a stress distribution through the glass profile for architectural and automotive glass panels. It performs the readings automatically without wasting material on each reading, except for a drop of immersion liquid; it is also quite portable and simple to

use. These characteristics make it a very interesting option for a more generalized use in determining the strength of glass. In fact, Aben *et al.* (2010) refer a simplified relationship (equation (2)) between the bending strength of glass (σ_{bs}) and its surface stress (σ_{sf}), the strength of annealed glass (σ_a) and an empirical coefficient ($k \cong 1$):

$$\sigma_{bs} = \sigma_a - k \cdot \sigma_{sf} \quad (2)$$

An extensive preparation was required to study the impact of each of the parameters included in the equipment software and of the testing conditions on the results obtained. Of all the readings performed, three tests were selected and are presented next as they fulfil different and complimentary goals. These tests are the following: (i) the full-length test; (ii) the area test and (iii) the test with different thicknesses. The goals of these tests are summarized in Figure 35 and their specific methodology and results obtained are described in section 4.3.6.

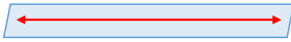
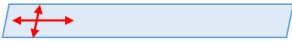

Name of analysis	Full-length test	Area test	Test with different thicknesses
Goal	Understand the distribution of the residual stress along the total length of the plate	Investigate the surface stress near the ends and corners of the plate and the symmetry of the stress distribution	Study changes in the stress profile of different thicknesses and of samples produced by different manufacturers
Readings			

Figure 35 – The three SCALP tests carried out – summary of goals and focus of the readings done

4.3.2. Test principle

The test principle is based on the concepts of stress birefringence and photoelasticity of glass. Birefringence is a phenomenon in which a ray of light passing through a given material experiences two refractive indices. Photoelasticity is a property of the materials that exhibit birefringence when subjected to stresses. The magnitude of the refractive indices at each point in the material is directly related to the state of stresses at that point, as evidenced in the Stress-Optic Law by Maxwell (McGraw-Hill, 2003).

Accordingly, if n_1 , n_2 and n_3 are the principal refractive indices for waves vibrating parallel to the principal stresses (σ_1 , σ_2 and σ_3 , respectively) and C is the photoelastic constant, equation (3) expresses the Stress-Optic law. If polarized light passes through the glass by normal incidence (axis 3), the wave is split into planes 1-3 and 2-3. Then, the relative retardation, R_t , is given by the Wertheim law presented in equation (4), where t is the thickness of the panel. These equations are the basis for the photoelastic analysis, expressing the relationship between refractive indices and stresses (Aben & Guillemet, 1993; McGraw-Hill, 2003).

$$n_1 - n_2 = C \cdot (\sigma_1 - \sigma_2); \quad n_1 - n_3 = C \cdot (\sigma_1 - \sigma_3); \quad n_2 - n_3 = C \cdot (\sigma_2 - \sigma_3) \quad (3)$$

$$R_t = C \cdot t \cdot (\sigma_1 - \sigma_2) = t \cdot (n_1 - n_2) \quad (4)$$

There are several photoelastic methods for determining the stress. Aben and Guillemet (1993) and later Aben *et al.* (2008) highlight five of those methods, either in use or in development:

- *The frozen stress method*, which involves heating the plastic model and loading it; after cooling and removing the loads, the stresses are “frozen” and stress analysis consists of examining the photoelastic fields of its slices. Although not applicable to glass, it is useful to models of plastic.
- *The integrated photoelasticity*, generally used for axisymmetric glass specimens – the polarized light passes through the whole sample in an immersion bath and the polarization change is recorded (example of such a device: Automatic Polariscope, or AP-07, by *GlasStress*).
- *The photoelastic tomography*, used in case of non-axisymmetric glass articles, consists of passing a light beam through the specimen at once and characterizing each point with a single parameter; the stress field is composed by the measurement of a single stress component at a time.
- *The mirage method*, used to determine the surface stress of automotive or architectural glass panels, exploits the gradient of the refractive index in the tin side: an incident polarized beam resurges at the surface with changes in the polarization according to the surface stress (example of such a device: Grazing Angle Surface Polarimeter, or GASP, by *Strainoptics*).
- *The scattered light method* has the same usage as the mirage method but provides an in-depth stress reading; an incident laser is scattered as it passes the glass panel and, as the scattered light intensity depends on the birefringence caused by the stresses, the stress profile can be determined.

4.3.3. Scattered light method

The method chosen for the analysis was the scattered light method. The device used was the *Scattered Light Polariscope 05 (SCALP-05)* equipment manufactured by *GlasStress*. The SCALP-05 emits a 5 mW polarized laser beam with a wavelength of 635 nm (*GlasStress Ltd*, 2013). Figure 36 illustrates the test principle. The beam passes through the polariscope prism and enters the glass panel at a specific angle. As it passes through the panel, the laser is scattered in planes perpendicular to the beam. The polarization of the scattered laser changes due to the stress birefringence. Variation of the polarization also means variation of the intensity. Those changes are recorded by a charge coupled device (CCD) camera that has a high quality sensor in terms of accuracy and light sensitivity. The laser beam is optically modulated and light intensities recorded by the camera from each pixel should vary sinusoidally. The variation of the intensity of the scattered light along the laser beam is registered, the retardation through the panel thickness processed and fitted into a retardation curve (retardation fit) and, finally, that curve is inverted and the stress profile is calculated. (*Aben et al.*, 2008; *Aben et al.*, 2010; *GlasStress Ltd*, 2013).

As chemically tempered glass has a high surface stress on a very thin layer, the angle of entrance of the laser is lowered so that the laser stays for a longer length in this layer. In fact, the standard option for the angle of entrance of the SCALP-05, measured from the perpendicular of the surface of the glass, is 70° but, when applied to chemically tempered glass, it should be calibrated to an entrance angle of 80°.

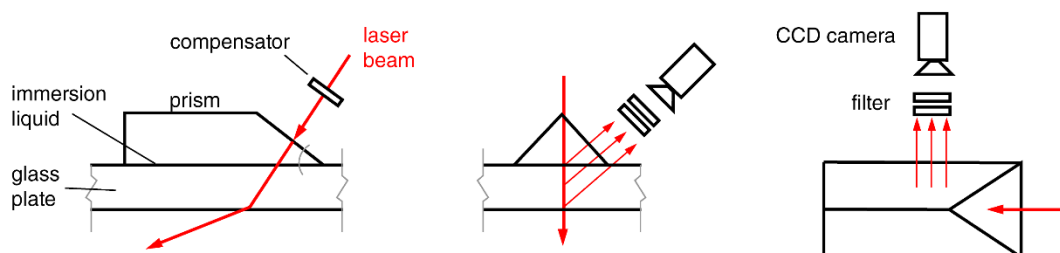


Figure 36 – Side, profile and top view of the SCALP working principle (adapted from *Aben et al.*, 2008)

There are several current and potential applications for this method. In terms of strength, a good correlation was found between surface compressive stresses and mechanical strength (Schiavonato *et al.*, 2005) using the mirage method. Therefore, the SCALP has been tested as a replacement of the standard tests of four-point bending (EN ISO 1288-3, see 2.7.1) and fragmentation test (EN 12150-1) (Aben *et al.*, 2010). Although this study does not consider chemically tempered glass, it proposes to reconsider those destructive and expensive tests in favour of residual stress measurements. To further investigate tempered glass, SCALP is also being used to understand the inhomogeneity of residual stresses, both locally and globally (Anton *et al.*, 2012). As an example of future applications, the development of laser sheet scattered light method is quite promising (Castellini *et al.*, 2012). This non-contact technique provides a full stress profile of a section of a flat glass plate, presenting much more data and being more suited for industrial uses, such as support of furnace control.

Regarding chemically tempered glass, Hödemann *et al.* (2016) presented the benefits of applying a curved ray inversion (CRI) instead of the standard straight ray inversion (SRI). The inversion process turns the optical retardation registered into the stress profile. The core assumption of SRI is that the laser ray goes in a straight line from entrance to exit spot and provides accurate results for entrance angles of around 45°. However, there is a local curvature of the ray due to the gradient of refractive indices. The study uses a modified SCALP on a 15 mm thick glass that is chemically tempered for this purpose with a depth of layer⁸ (DOL) of 365 µm and whose optical parameters were thoroughly studied. Presented as the gradient scattered light method, it yielded significantly improved results over the standard version.

4.3.4. Methodology

As mentioned above, the polariscope used in the experiments was SCALP-05 (Figure 37) which is complemented with the software *GlasStress SCALP* version 5.8.0.11, released in 2015. As this model operates with a laser of low output power, it is suggested to keep the ambient light level below approximately 50 lux (cloudy day) while making the measurements. The equipment has a measurable thickness between 1 and 6 mm and an error of less than 5%, although its accuracy is not certified yet. The measurements are spaced around 2,1 µm. The methodology presented below was followed in the tests and is suggested in the manual of SCALP (GlasStress Ltd, 2013); some adaptations were made to study the influence of some parameters (detailed ahead in section 4.3.5).

To start, the periscope must be connected to the computer with the SCALP software turned on. A live video of the laser in the glass appears on the screen. The following step is the cleaning of both the surface of the glass and the periscope's prism, which is of the utmost importance for the quality of the readings. Either alcohol or the immersion liquid with paper or cloth were used to cleanse the fingerprints, dirt or liquids from the surfaces in a circular motion from inside out (the classical optics cleaning method). Still, most of the tests were carried out on glass samples removed for the first time from the packaging box, completely clean, so only the periscope needed cleaning.

The safety mechanism prevents the laser from exiting the prism by making a total internal reflection. So that it can exit the prism, an immersion liquid is required to refract the laser. Therefore, the Cargille

⁸ As mentioned in chapter 2, DOL refers to the depth of the layer of residual compressive layer in the glass surface

immersion oil (provided with the equipment), whose refraction index is $n = 1,52$ at 635 nm, was applied on the glass where the measurements were to be made. It is also advisable to apply the immersion liquid to the opposite surface of glass in order to reduce the diffused light and laser speckle; although the influence of this procedure was tested, it is not always easy to carry out this suggestion as usually the bottom surface of the glass is supported on another surface.

After placing the periscope's prism onto the immersion liquid (Figure 38), the video image stabilizes and must be checked. At this stage, some parameters can be adjusted to assure a better result; this is explained in the next section. After this calibration, by simply clicking the "Measure" button a measurement of a specified number of seconds (3 by default) starts, after which the Retardation and corresponding calculated Stress distribution graphs are displayed. A convenient feature is the "Repeat" button, which takes several consecutive measurements with the same conditions.

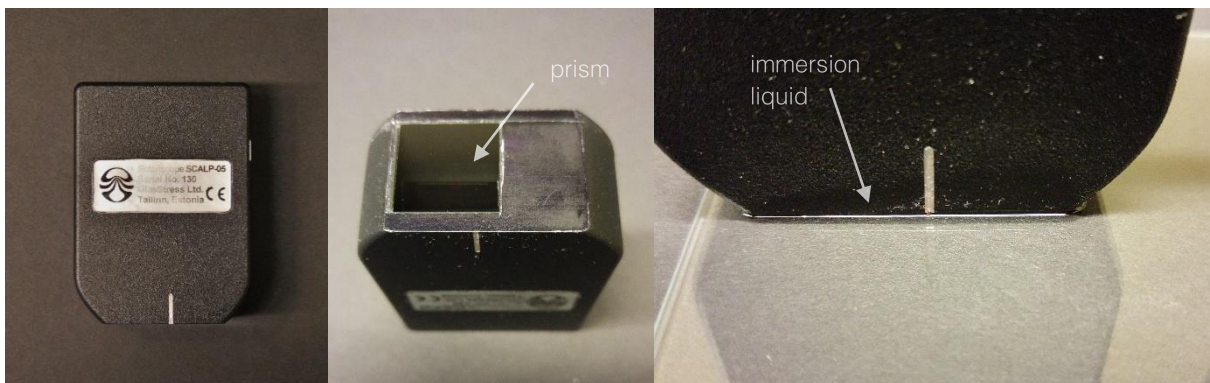


Figure 37 – SCALP-05, front and bottom view

Figure 38 – Example of a reading, focusing on the immersion oil

4.3.5. Preliminary tests

An extensive set of preliminary tests was carried out to 1) understand the influence of the software parameters and 2) assess the influence of the testing conditions. The results are presented in the Appendix B, and explain many details of operating the SCALP.

4.3.6. SCALP test results

4.3.6.1. Full-length test

The main goal of the full-length test was to study the variation of the surface stress along the length of the plate. It consisted of consecutive readings spaced of 10 mm along the whole length of the plate. The polariscope was positioned in the centre of the plate's width and moved to the following position by slowly sliding it. A ruled paper was used as a background. The readings start on the 2nd centimetre and finish on the 70th as a consequence of the length of the polariscope prism.

Results are presented in Figure 39, where DOL was linearly interpolated between the points of transition of compressive to tensile stress (readings were spaced 2,11 μm in depth, on average). At the 24th centimetre, the polariscope was removed and cleaned. There was a noticeable difference in the video regarding the entrance point, which is depicted in Figure 40. Although there is not a significant impact in the surface stress from readings 24 to 25, the variation of the average before (red) and after (blue)

cleaning is noteworthy. This could also be explained by the influence of the reflection on the edge as the laser was always facing the same edge.

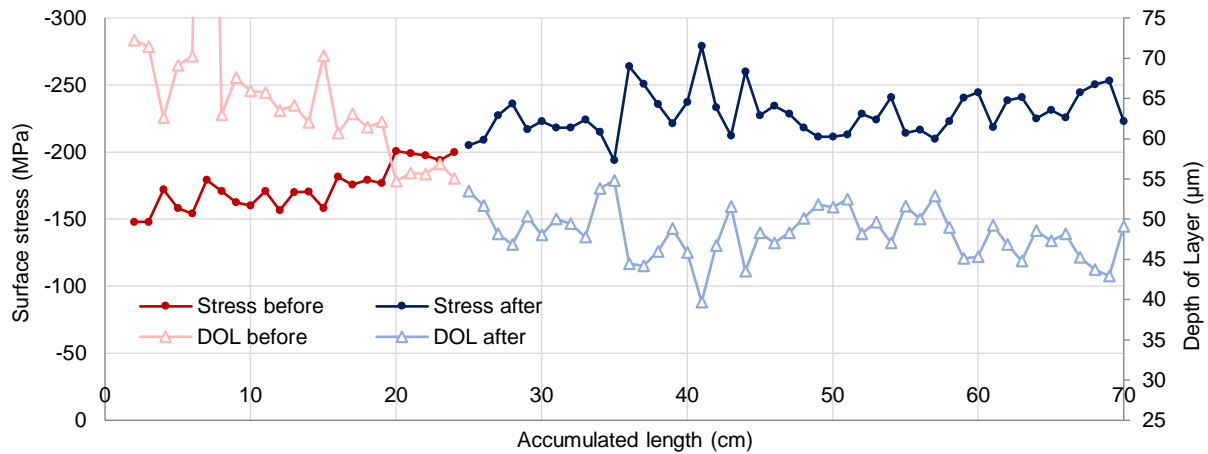


Figure 39 – Surface stress and depth of layer along the whole length of the plate

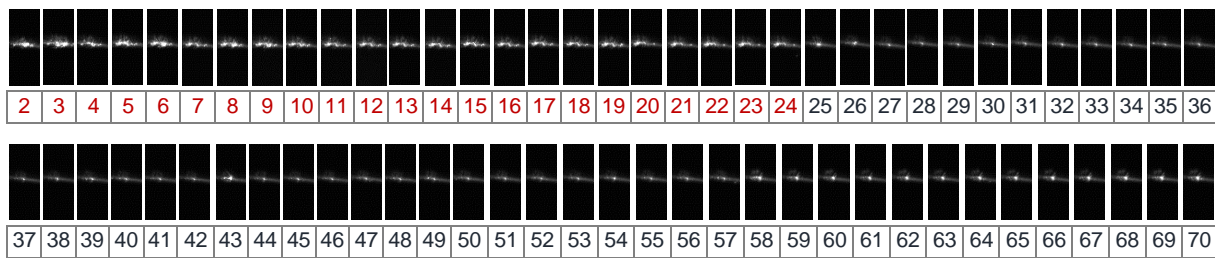


Figure 40 – Detail of the video focused on the entrance spot of all readings

The most immediate conclusions that can be drawn are the following: there is a strong negative correlation between surface stress and depth of layer, which is suggested in the product datasheet (AGC; see A.1); the magnitude of the obtained surface stresses is far below the value of 600 MPa to 800 MPa, expected for the type of glass being tested.

The cleaning did not have a direct immediate impact in the readings and globally the results are coherent, which is a sign in favour of the quality of the test. On the other hand, the abrupt changes in stress when all settings remain constant do not testify in favour of the test performance. Indeed, the distance to the edge appears to play a role and perhaps there is inhomogeneity of the residual stresses, as it has been investigated in tempered glasses with the SCALP (Anton *et al.*, 2012). However, from readings 35 to 36, for example, stress varies from 194M Pa to 264 MPa, which is a very significant sudden variation. Repetition of the test on the same glass sample would be insightful, but one should take into consideration that the conditions of cleaning would change.

4.3.6.2. Area test

The aim of the area test was to study the surface stress distribution on the area, particularly near the edges and corners. Six positions were chosen to make the measurements, with the SCALP pointing for two or three directions in each reading point, as illustrated in Figure 41 with the respective results.

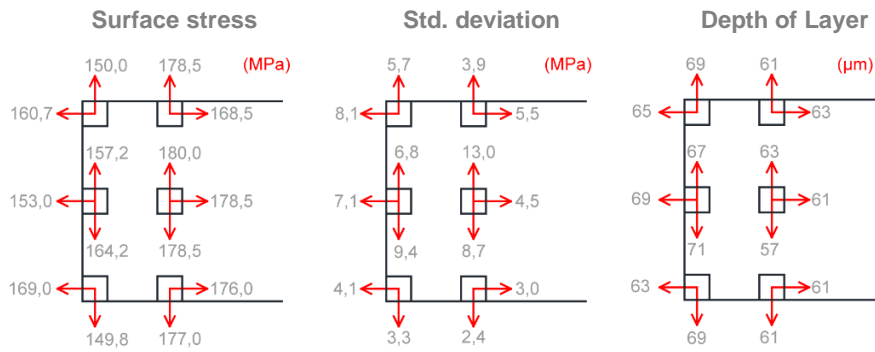


Figure 41 – Scheme of the stress results (MPa) with respective standard deviations and DOL (μm) for the area test

The fit error was around 2,0 for all measurements, which indicates good accuracy. A quite significant symmetry was observable in the stress measurements: as the direction of the SCALP and the distance to the edge remain constant, the surface stress for the symmetrical points is consequently similar. However, as for the former test, the magnitude of the surface stresses is far below than what was expected.

4.3.6.3. Test with different thicknesses

As mentioned, the test with different thicknesses had several goals: to understand the influence of the glass thickness in the stress profile; and to study the performance of SCALP on samples of different thicknesses and produced by different manufacturers. For this test, five different samples from SCHOTT were used with thicknesses of 0,55, 0,70, 1,10, 2,00 and 3,00 mm. Figure 42 and Table 7 summarize the results, displaying the surface stress distribution for the various specimen thicknesses. Since only one position was tested for each thickness, more information was added to the analysis on the depth.

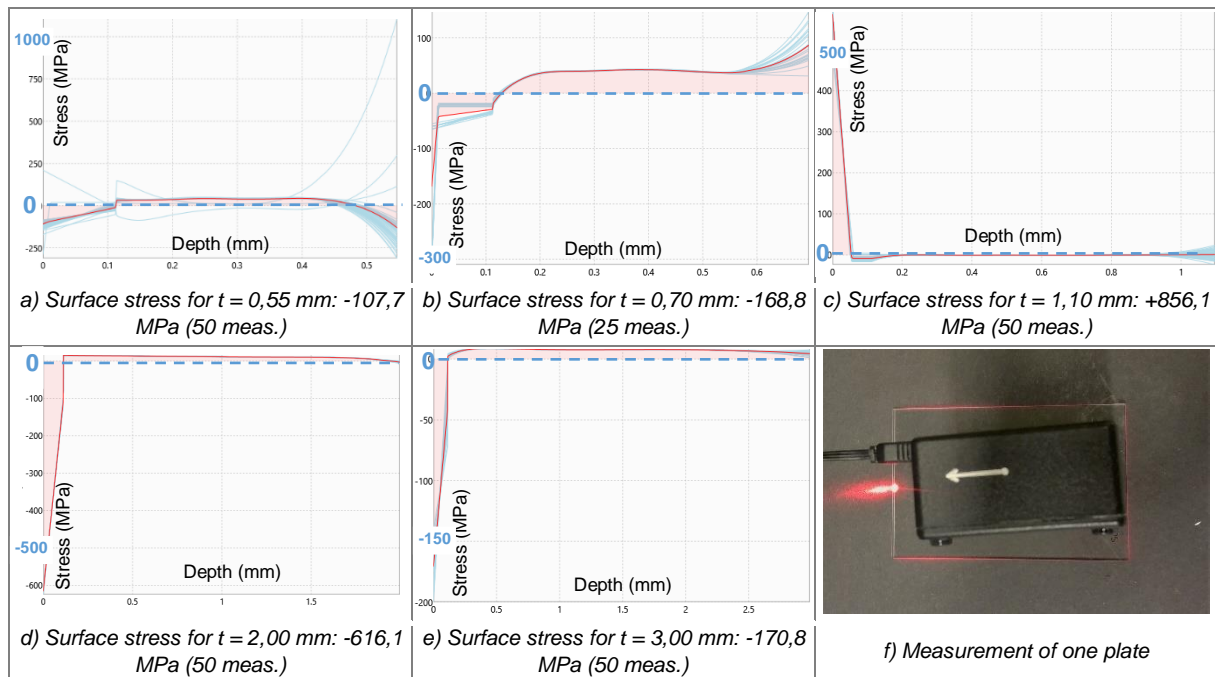


Figure 42 - SCALP tests on SCHOTT samples: a) to e) stress distribution (y-axis) vs. depth (x-axis) for different thicknesses and f) picture of measurement

Table 7 – Results of SCALP readings for Xensation samples with 5 different thicknesses

Sample thickness (mm)	Number of measurements	Surface Stress (MPa)	St. Deviation (MPa)	Meas. Depth (mm)	Depth of layer (μm)	Fit error (MPa)
0,55	50	-107,7	54,6	0,55	113,8	4,9
0,70	25	-168,8	121,7	0,70	126,7	3,5
1,10	50	+586,1	23,9	1,10	52,3	3,6
2,00	50	-616,1	3,8	2,00	111,1	3,1
3,00	50	-170,8	12,1	3,00	111,7	4,9

One did not expect the specimens' thickness to have significant influence on the results provided by the SCALP tests, since the compressive layer should have similar depth for the different specimens tested. However, results presented in Figure 42 and in Table 7 indicate that such impact is visible, for example, on the standard deviation values that are quite significant for thinner glasses (0,55 and 0,70 mm), perhaps caused by larger interferences of reflections at the exit of the laser beam as the opposite surface is nearer. It is also worth highlighting the measurement made on the 1,10 mm thick specimen, in which the surface stress was positive (*i.e.*, tensile) and the sign was switched at less than half of the depth of the other samples – no reasonable explanation or justification was found for such unexpected results. Although with very different values, the readings were more stable for thicker glasses. Tests were repeated weeks after, but results obtained were different than the initial ones, highlighting the overall unreliability of the test when used with thin glass.

4.4. Concluding remarks

In this chapter, two non-destructive tests were introduced and assessed: the tin side detector test and the SCALP test.

For the tin side detector test, the motivation and a brief test principle were presented. Then, two methods were employed on different samples: Leoflex (chemically tempered thin glass, 2 mm thick), Xensation (chemically tempered thin glass, thicknesses of 0,55; 0,70; 1,10; 2,00 and 3,00 mm), and float glass (10 mm thick). The results obtained were not conclusive, indicating that this test may not be appropriate for chemically tempered thin glass, at least when using the procedure followed herein.

For the SCALP test, the motivation and test principle were explained more comprehensively. An overview of the methodology and of the preliminary tests carried out to understand the influence of the parameters was presented. Subsequently, three tests were designed and experimented: (i) the full-length test, centred on understanding the distribution of the residual stress along the length of the plate; (ii) the area test, focused on the surface stress near the ends and corners of the plate and the symmetry of the stress distribution; and (iii) the test with different thicknesses, to study changes in the stress profile of different thicknesses and of samples produced by different manufacturers. The results obtained also raised several doubts, as the stress values provided by the SCALP tests (200 MPa) were much lower than those reported by the producer for the maximum stress (from 600 MPa to 800 MPa, see Appendix A) and also from those obtained from the mechanical tests reported in the next chapter.

5. Destructive testing

5.1. Introductory remarks

In destructive testing, experiments are carried out up to failure, in order to investigate the specimens' performance or the material behaviour when subjected to mechanical loads. These tests generally yield more information and are easier to interpret than non-destructive tests, as they can replicate more closely the effects of actual loading conditions. In general, these tests are more expensive than non-destructive tests, but can be economically interesting if the items are mass produced and hence the costs of mechanically testing a small number of specimens is negligible. When testing thin glass, while the price per sample is still very high, the experience and investment in production techniques will certainly lower the costs, and the decision between testing methods depends on the trade-off between cost and reliability of the tests.

For the destructive mechanical tests with increasing loadings, the stress rate is a measure that can be replicated adequately in different setups or geometries of the samples, in opposition to displacement or applied force rates that are not directly related to the material strength. In fact, the standard EN ISO 1288 establishes $2 \pm 0,4$ MPa/s as the rate for strength testing. Experimental studies on glass use a stress rate and the literature categorizes the results accordingly. Vandebroek (2014) used three main test rates: 50 MPa/s, 2 MPa/s (EN ISO 1288) or 0,08 MPa/s (EN 1991-1-4, wind loading).

In the present experimental campaign, a stress rate of 2 MPa/s close to the failure was adopted in the destructive tests carried out. The rate of 2 MPa/s was deemed as the most adequate to the goals of the research, mainly for the sake of coherency with the standard EN 1288, but also as such rate corresponds to a quasi-static testing speed: compared to 50 MPa/s, it provides a longer interval and more data to study the behaviour per test and it avoids dynamic effects; on the other hand, the 0,08 MPa/s rate is used basically for wind loading tests and would make each test last more than two hours and a half.

The experimental program presented in this chapter comprised in-plane four-point bending tests and buckling tests in glass specimens subjected to in-plane compressive loads. The experimental study is complemented with numerical analyses. The main goal of these numerical analyses was to obtain a better understanding of the results obtained in the experiments.

5.2. Assessment of in-plane four-point bending behaviour

5.2.1. Objectives and methodology

The main goal of this test is to investigate the ultimate strength of thin glass samples, knowing that the most tensioned part of the section is the bottom edge. Given the slenderness of the thin glass samples, and being subjected to in-plane loads applied at the top edge, lateral torsional buckling is likely to occur. Therefore, these tests may also provide insights on this phenomenon. Yet, to determine the ultimate strength of glass, it is of interest to prevent such phenomenon; therefore, this test is also useful to determine what is required to prevent lateral-torsional buckling of glass members under in-plane loads.

The advantages of this test method are the following: the four-point bending setup has been thoroughly studied for many applications; it focuses strictly on the edge over a significant length and is the best setup to study the strength of such component; furthermore, if well designed, the behaviour of the sample is linear, not requiring much instrumentation to obtain the results. The difficulties lie on the effective lateral constraint and on the concentration of stresses on the points of contact between glass and metallic parts of the setup.

In terms of methodology, several iterations of the experimental setup were required and, consequently, several numerical analyses were carried out to study the implications of each modification of the setup. Therefore, both experimental and numerical tests are presented, in sections 5.2.2 and 5.2.3, respectively.

5.2.2. Experimental tests

5.2.2.1. Geometry of the setup and instrumentation

The test setup followed a common symmetrical four-point bending configuration, with 600 mm between supports and 200 mm between load points, thus 200 mm between loads and supports. These measures are depicted in Figure 43 and were common throughout all tests; the setup modifications required were just concerned with the lateral constraints (see 5.2.2.2). Several reasons motivated the choice of these measures:

- To be comparable to EN 1288-3, which is also based on a 200 mm loading span;
- To simplify repetition and execution: the length is divided in thirds, the loaded length is 2,5 times the height of the section and all measures are round;
- To introduce maximum stress in a considerable portion of the plate's length.

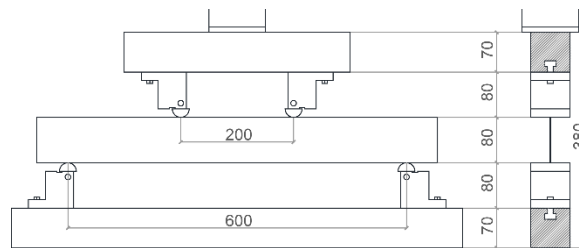


Figure 43 – Setup of the in-plane four-point bending test used in all iterations, front and side view, no lateral constraint depicted

The tests were performed in a Universal testing machine *Zwick100*, with a maximum test force in either tension and compression of 100 kN (the expected maximum load was over 10 kN). This machine records the vertical displacement and the force applied; previous studies at TU Delft indicate that it has an accuracy of $\pm 2 \mu\text{m}$ in displacement and around 5 N in force. The connection of the compression machine to the loading head only allows for rotation in the axis perpendicular to the plate so that the same load is applied on each contact point. No other instrumentation was used in the tests.

To achieve a stress rate of 2,0 MPa/s on the bottom edge, assuming the behaviour is linear close to the failure of glass, a cross-head displacement rate of 0,0234 mm/s was applied. With that assumption, a displacement of 1 mm corresponds to an increase of 85,25 MPa (data obtained with the numerical analysis presented ahead in section 5.2.3).

5.2.2.2. Setup development and preliminary tests

The development of the whole setup was a quite long and iterative process because it was designed and built from the available materials and most of its components had to be cut, welded and attached

to the main beam. What made it particularly time-consuming were the several difficulties to achieve an effective lateral constraint. To test each solution, instead of a glass sample, an aluminium plate (with similar elasticity modulus of glass) of the same dimensions was used (for cost reasons).

The details and results of each stage as well as the reasoning behind the modifications are described in the following paragraphs. While this subsection provides a more qualitative overview, the next one (5.2.2.3) provides the results of the preliminary tests on aluminium and the tests on glass.

The study of this setup comprised three stages and 8 preliminary tests. A final setup is proposed as well. Figure 44 shows, for each of the three stages of the setup, a) a scheme highlighting the modification introduced at a given stage, b) a picture of the physical setup, and c) the preliminary results obtained with aluminium plates, in terms of failure mode or deformed shape of the test specimen. In addition, the testing conditions per test are summarized in Table 8 and are explained afterwards.

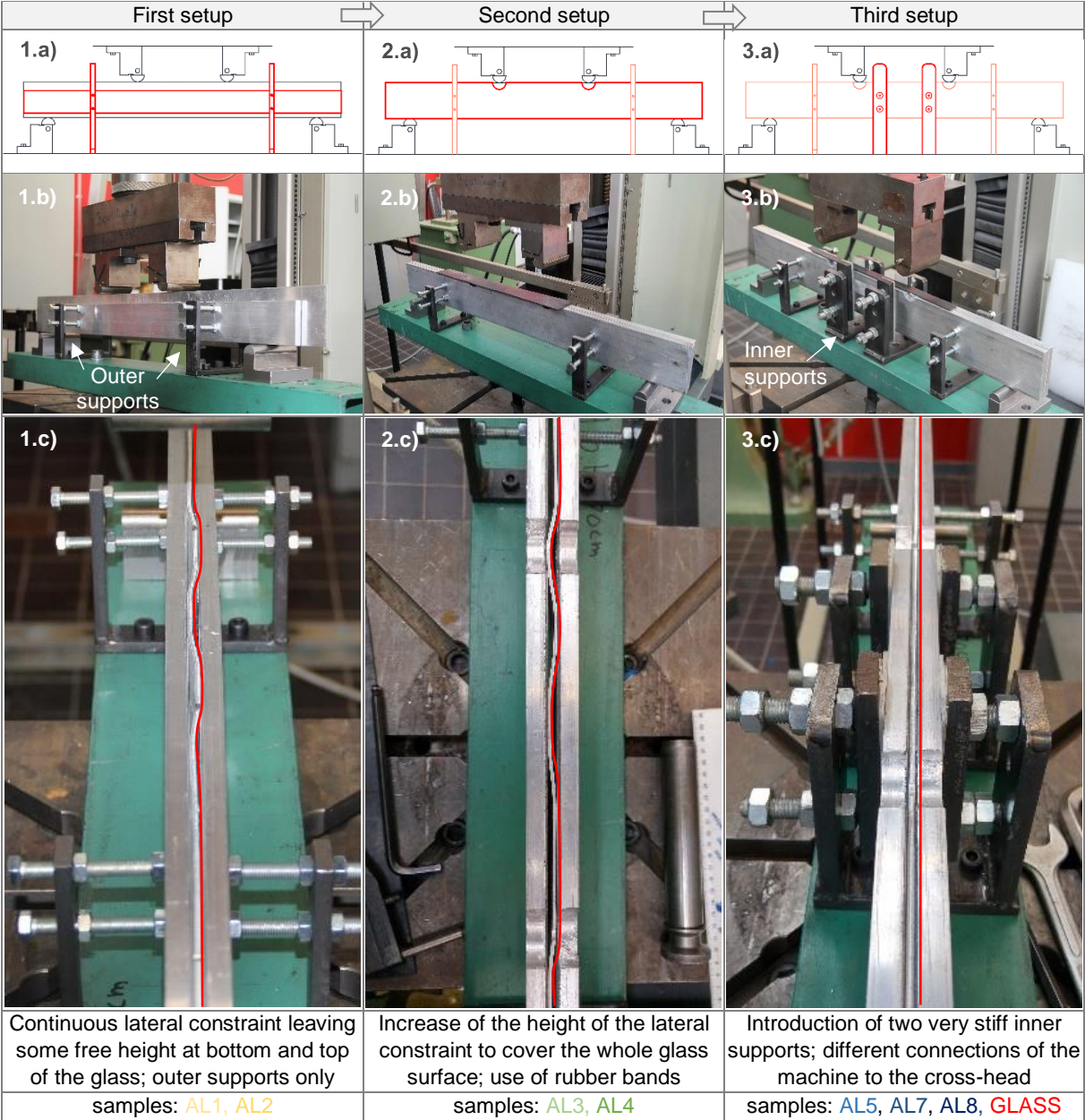


Figure 44 – Successive modifications introduced on the setup and results of preliminary tests

Table 8 – Summary of the conditions for each of the preliminary tests and for the final test (yet to be performed).

Setup Sample tested		First		Second		Third			Final	
		AL1	AL2	AL3	AL4	AL5	AL7	AL8	GLASS	FINAL
Lateral constraint	Partial constraint	x	x							
	Full constraint			x	x	x	x	x	x	x
Supports for lateral constraint	Outer supports	x	x	x	x	x	x	x	x	x
	Inner supports					x	x	x	x	x
Connection	Spherical	x	x	x	x	x	x			
	Fixed							x	x	
	Cylindrical									x
Rubber band				x	x	x	x	x	x	x

Concerning the first setup, only the outer lateral supports were applied and the aluminium plates were 15 mm thick and 50 mm high, leaving 20 mm on the top and 10 mm on the bottom of the glass plate unconstrained. Teflon stripes were glued to the inside of the lateral constraints to reduce the drag caused by the compression of those constraints against the glass and allow the sliding once loaded.

A spherical connection between the test machine and the loading head was used, allowing rotations in all axes. When tested (AL1), the aluminium plate buckled and the lateral supports were pushed apart, creating some gaps between the buckled plate, as shown in Figure 44 1.c). The second attempt with this setup (AL2), leaving 10 mm on the top and 20 mm on the bottom of the glass unconstrained, required considerably more force to buckle.

For the second setup, in order to increase the resistance of the lateral constraint, the area of the lateral plates was enlarged to cover all of the test samples, except for two holes where the loads were applied (thus penetrating the plates). The holes are 13 mm deep (in the centre) where the loads are applied – this value was defined based on numerical analysis (see 5.2.3). It was requested that the new plates were made of steel or thicker aluminium, but these materials were not available. One had concluded that the buckling was triggered on the upper part of the section and then the lateral constraint could not resist the lateral force and also underwent considerable deformations. So, by covering all the plate, the buckling would be prevented from the beginning.

However, in the preliminary tests with the new setup (AL3 and AL4), the sample buckled as shown in Figure 44 2.c), at a higher load than in the former tests. The same aluminium sample was tested (AL3) and reused in the next test, upside down with a slight curvature upwards (AL4).

In these tests, a rubber band with around 2,0 mm of thickness was used to address the concentration of stresses on the sample caused by loads and supports, which had originated significant dents on former tests. It has the advantage of being easily replaced because it sustains a very high stress in each test and is locally damaged after. These rubber bands were used in all the tests carried out afterwards.

Finally, in the third setup, the stiffness of the constraint was addressed. Two much stiffer supports were added near the centre of the lateral constraint (visible in Figure 45). Furthermore, the contact between supports and tested plate was granted by large screws and wide steel plates, while the outer supports only counted on regular screws at a considerable distance from the plates. The lateral constraint plates were the same as those for the second setup.

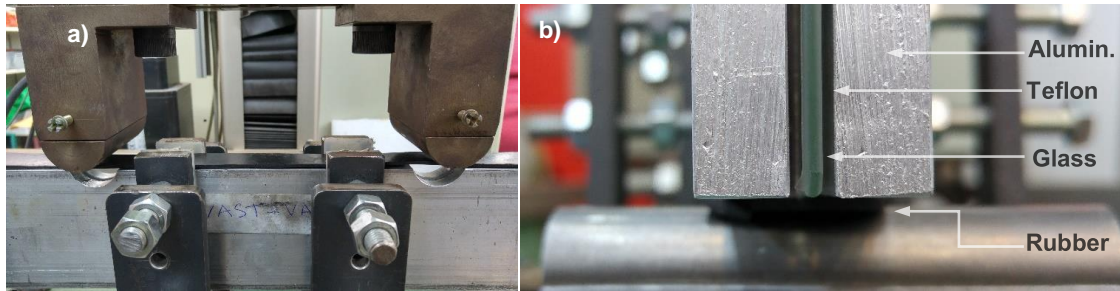


Figure 45 – In-plane four-point bending setup, front and side view, with focus on a) loading and b) lateral profile

For this third setup, three preliminary tests were done. In the first one (AL5), the specimen was very tightly positioned within the lateral constraint system - it was too hard to even move the sample by hand. The specimen did not buckle, but the force displacement graph revealed some unexpected sudden load drops. The second one (AL7) still revealed some buckling because the constraint was not tight enough, but this was less evident and occurred at an even higher load. The graphs are not easy to interpret because the force reached is much higher than previously obtained and the corresponding tension in the section is very high. After these tests, it was observed that the loading head was slightly tilted as it was not perfectly centred in the sample; therefore, such load eccentricity certainly contributed to the lateral buckling of the specimen. The last aluminium sample (AL8) was introduced and tightened in a way it could be moved by hand when some reasonable force was applied; regarding the connection of the *Zwick* machine to the cross-head, it was changed to a fixed connection temporarily, as there was no cylindrical connection available (such a connection was designed and built after the final test). A glass sample was also tested with the same conditions as the former aluminium sample.

5.2.2.3. Experimental results

The instructions about the final setup modification were given and executed. Thus, shortly after these preliminary tests, the proposed setup was already complete for further testing (see 5.2.4). However, it was decided to suspend these tests, because (i) the number of glass plates available was limited and (ii) it was decided to prioritize the buckling test as its setup is more straightforward. Indeed, the last preliminary four-point bending test was performed on the same day of the first preliminary buckling test, which provided far less complications and a better basis to proceed (see 5.3).

Therefore, only preliminary results are available, whose maximum values in terms of cross-head displacement, load and bending stress are presented in Table 9. Figure 46 presents the preliminary results in terms of a force vs. cross-head displacement graph, where the influence of each modification in the behaviour is shown, including the results obtained with the glass sample. It is important to note that the test includes many modifications that must be considered (Table 8); the behaviour is expected to be similar within iterations and, altogether, it should converge to a non-buckling failure of the sample. The successive iterations are displayed with different colours: yellow for the first attempt, green for the second one and blue for the last, with red corresponding to the glass sample.

The detailed behaviour corresponding to the very first millimetres of deformation is also interesting and is presented in a force vs. cross-head displacement graph (Figure C-3 of Appendix C). It shows that as the iterations further constrain the sample, the sooner the loading is effective in creating a sustained

displacement. Also, the loading of glass has a much higher oscillation in terms of applied force than in the aluminium samples (amplitude of 10 N versus 1 to 2 N).

Table 9 – Maximum values of cross-head displacement, force and corresponding bending stress in all samples

	AL1	AL2	AL3	AL4	AL5	AL7	AL8	GLASS
Displac. (mm)	*3,70	6,59	2,56	6,11	11,86	9,56	6,86	6,83
Force (N)	913,32	1561,28	2488,02	4075,48	8966,73	6626,02	5096,00	4525,34
Stress (MPa)	42,81	73,19	116,63	191,04	420,32	310,59	238,87	212,13

*note: maximum displacement does not correspond to maximum force

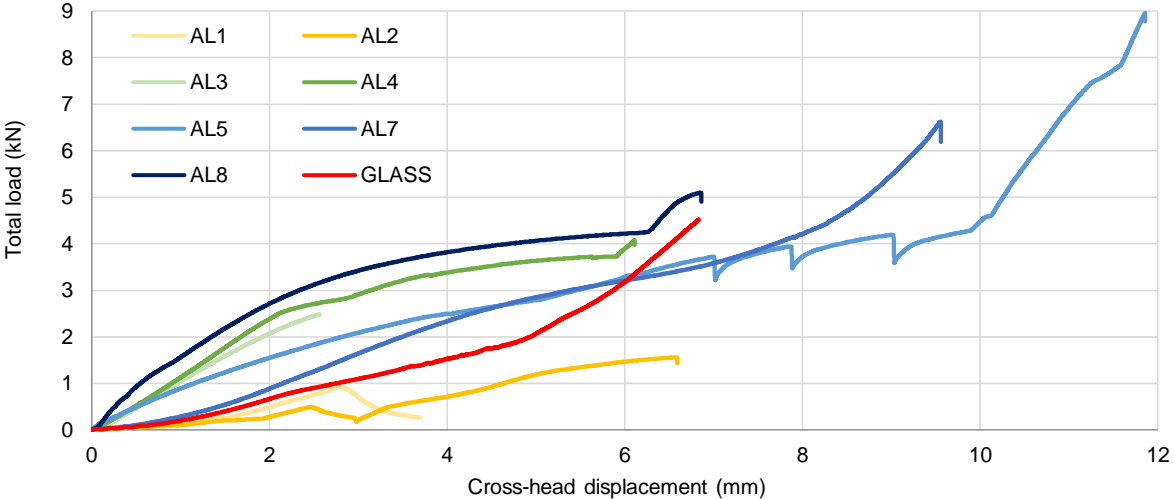


Figure 46 – Force-displacement graph for all preliminary tests

Regarding the test with the glass sample, which is more indicative of how the final test would work, the results were not as linear as expected. One thing to consider in the behaviour is the fixed head, which might not have been fully horizontal. The main factor of the early low stiffness seems to have been the rubber bands, which are around 2,0 mm thick and whose Young’s modulus is far less than that of glass; at around 5 mm of cross-head displacement the stiffness increases gradually. However, aluminium samples 3 to 8 also had the rubber band and do not present such behaviour. The geometry of the edge is a plausible explanation for this difference: the edges of the glass section are round and may work as a wedge to penetrate the rubber more easily, opposed to the orthogonal bottom surface of the aluminium section that may only compress it. Figure 47 shows the cracking pattern after the breakage of the glass sample, saved by the foil that had been glued to its surface. In fact, some marks are visible where the supports contacted the glass, but those marks are due to the foil; as the glass penetrated the rubber on the supports, the foil was peeled by the rubber.

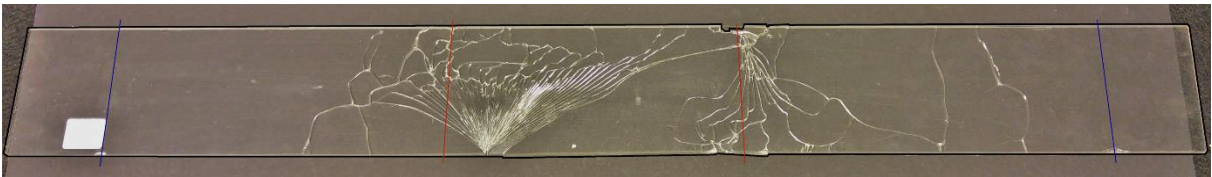


Figure 47 – Glass plate after breakage, with marks on the supports (blue) and loads (red)

Figure 48 (left) shows the flaw on the edge of the tested glass sample that might have compromised the strength of the glass plate. The foil was very useful to keep the shatters and allow the subsequent study of the cracking pattern, as only very small shatters were missing.



Figure 48 – Detail of a flaw on the edge of the sample (left tested and corresponding cracking pattern (right))

5.2.3. Numerical analysis

5.2.3.1. Objectives and overview of the numerical analysis

The numerical analyses were carried out to complement and support the experimental tests, iteratively. Therefore, several tests were required to study the behaviour of samples strictly under bending, i.e., without lateral torsional buckling, but also to investigate that buckling behaviour. Figure 49 summarizes the analyses, stating their goals, the nodal degrees of freedom (dof), the lateral constraints and lateral forces applied.

Name of analysis	Analysis 0 (Leoflex glass; aluminium, variable σ_y)	Analysis 1 (Leoflex glass)	Analysis 2 (Aluminium $\sigma_y = 150\text{MPa}$) Analysis 3 (Leoflex glass)	Appendix C-3 (Aluminium $\sigma_y = 150\text{MPa}$) Analysis 4 (Leoflex glass)
Goal	Understand the theoretically perfect behaviour of the test, with no lateral displacement. Second, estimate the σ_y of the aluminium used	Validate the new model, its geometry and elements used (with many more d.o.f.) by comparing with Analysis 0	Study the lateral instability phenomenon and the influence of the lateral supports - represents 1 st and 2 nd setups	Study the lateral instability phenomenon and the influence of the lateral supports - represents 3 rd setup
dof	Two: $\{u_x, u_y\}$	Five: $\{u_x, u_y, u_z, \phi_x, \phi_y\}$	Five: $\{u_x, u_y, u_z, \phi_x, \phi_y\}$	Five: $\{u_x, u_y, u_z, \phi_x, \phi_y\}$
Lateral constr.	Perfectly constrained laterally (theoretically)	Only outer supports, no rotations at lateral supports	Only outer supports, no rotations at lateral supports	Both outer and inner supports, no rotations at the supports
Lateral force	No lateral / horizontal force applied	No lateral / horizontal force applied	Horizontal forces applied proportionally to the vertical displacement at load points	Horizontal forces applied proportionally to the vertical displacement at load points

Figure 49 – Overview of the set of analyses comprised in the numerical study regarding goals and lateral boundary conditions

Each of the following subsections states the goals of the analysis and the description of the model: types of elements, mesh size, boundary conditions, material properties, type of analysis, software used. The geometry of the object is constant: a plate of 710 mm by 80 mm. The analysis of the finite elements and the mesh sensitivity study were important to define the models but are not presented. The validation is done by comparing with the experimental results and by progressively introducing more complexity in the model, confirming results with the previous analyses.

5.2.3.2. Theoretically perfect behaviour – Analysis 0

This analysis had the main goal of studying the behaviour of the test under perfect conditions, not considering the factors that could hamper the results, such as lateral torsional buckling, drag caused by the lateral constraints or the deformation of the rubber bands. It was used to support the first experimental tests, but also to estimate the yielding tension of the tested aluminium samples and even to understand the experimental tests, by testing a hypothesis regarding the different stiffness observed in the glass sample.

For this analysis, the FEM software used was “DIANA Release 9.6” and the models were pre and post-processed in “midas FX+ for DIANA version 3.3.0”. As the loading is purely applied in the plane of the glass plate and the out-of-plane displacement is not allowed, a 2D analysis is suitable. Plane stress elements were used; more precisely, Q8MEM - quadrilateral elements with four nodes, each with 2 dof $\{u_x, u_y\}$ and three layers: each of the two outer surfaces and one in the middle (Figure 50). As these finite elements must be thin, square finite elements of 10,00 mm with a thickness of 2,00 mm were chosen. Figure 51 illustrates the mesh, the boundary conditions and the applied loads.

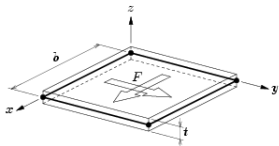


Figure 50 – Scheme of a plane stress element (source: DIANA)

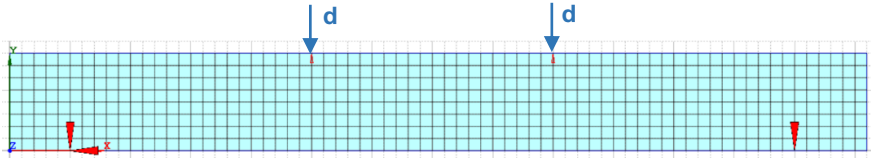


Figure 51 – 2D model with plane stress elements

The analysis was structural nonlinear, performed in displacement control, with 120 load steps of 0,10 mm, allowing both geometrical and physical nonlinearities, although one did not expect that the geometrical nonlinearities would have much influence on the results. The Newton-Raphson iterative method was used with displacement and energy convergence norm, with a maximum of 10 iterations; this iterative method is common to all numerical analyses.

Four tests were carried out. The conditions were common to all samples, only the materials changed: (i) the glass, modelled as a linear material with $E = 74 \text{ GPa}$, and (ii) the aluminium, with $E = 71 \text{ GPa}$ and for which three values of the von Mises yield tension were considered (to compare with the obtained results, $\sigma_y = 150 \text{ MPa}$ (AL150), $\sigma_y = 200 \text{ MPa}$ (AL200) and $\sigma_y = 250 \text{ MPa}$ (AL250)). Figure 52 presents the results in terms of total applied force and maximum principal stress versus the vertical displacement at the loaded sections (as registered by the test machine). Note that the rubber band is not modelled, hence the different stiffness in the first stage of the experimental test with glass.

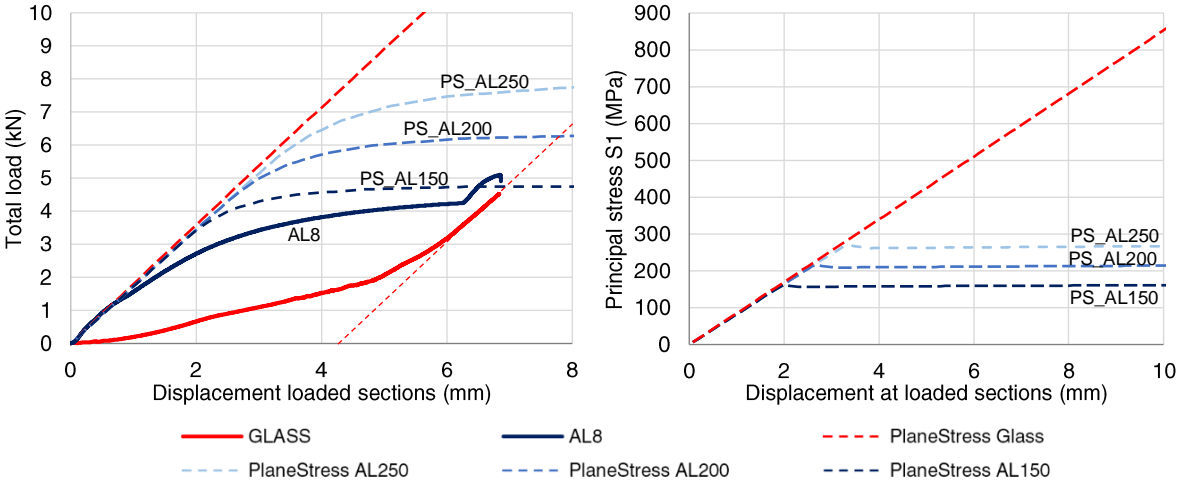


Figure 52 – Results of the numerical tests compared with the last preliminary tests (samples AL8 and GLASS)

An important value from Figure 52 is that the 800 MPa stress on glass is reached for 9 mm of displacement. Due to the compression of the bottom rubber band and the possibility to reach a higher value of stress, a margin of 4 mm was added and a value of 13 mm was defined for the holes on the

lateral constraint. The stiffness of the glass specimen is 1797,72 N/mm or 85,25 MPa/mm, meaning that a stress rate of 2 MPa/s requires a load rate of 42,39 N/s or 0,0234 mm/s.

As expected, the stress behaviour is different due to the physical nonlinearities and the magnitude of the applied displacement. Figure 53 shows the principal stresses 1 and 2 at the loaded sections for a displacement of 5,00 mm, where the aluminium is already yielding and there is considerable stress on the glass. It is noteworthy the concentration of stress along the edge in the case of the glass panel; the same is observed in the aluminium plate prior to yielding.

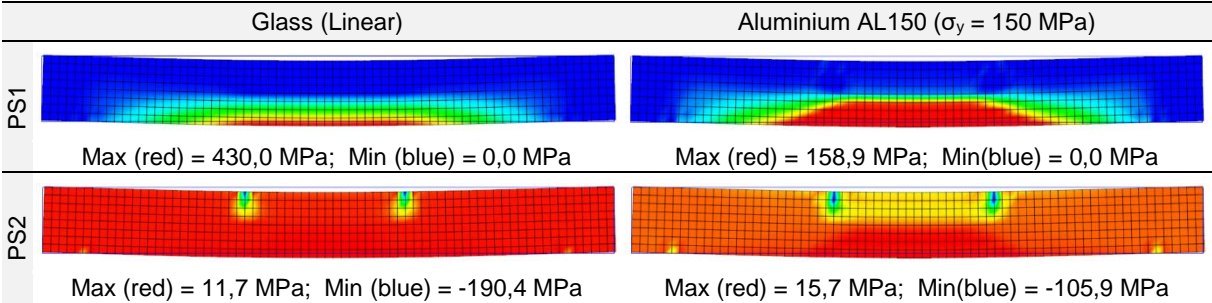


Figure 53 – Comparison of behaviour of glass and aluminium (AL150 $\sigma_y=150$ MPa) at 5,0 mm of displacement

Finally, to understand the influence of the connection of the compression machine to the cross-head being fixed or cylindrical, the same numerical model was used. The fixed connection translates into non-symmetric three-point bending loading, assuming that the cross-head is never completely horizontal and only loads one side of the glass in a first stage. The cylindrical connection causes the same load to be applied on both load points, creating a four-point bending system. Consequently, the goal of the analysis is to investigate if the fixed connection could contribute to the nonlinear two-stage behaviour observed for the glass sample. The hypothesis is that the lower overall stiffness of the first stage could be caused by the three-point bending, while the second stage presented a higher stiffness from the moment the cross-head touched the glass and a four-point bending developed. Figure 54 and Figure 55 depict the stress distribution in glass and the numerical results compared to the results obtained in the preliminary test.

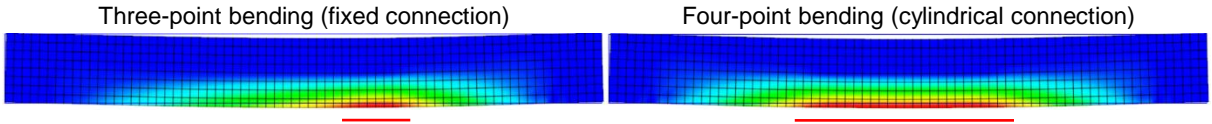


Figure 54 – Comparison of the principal stresses S1 due to one-point (fixed connection) and two-point loading (cylindrical)

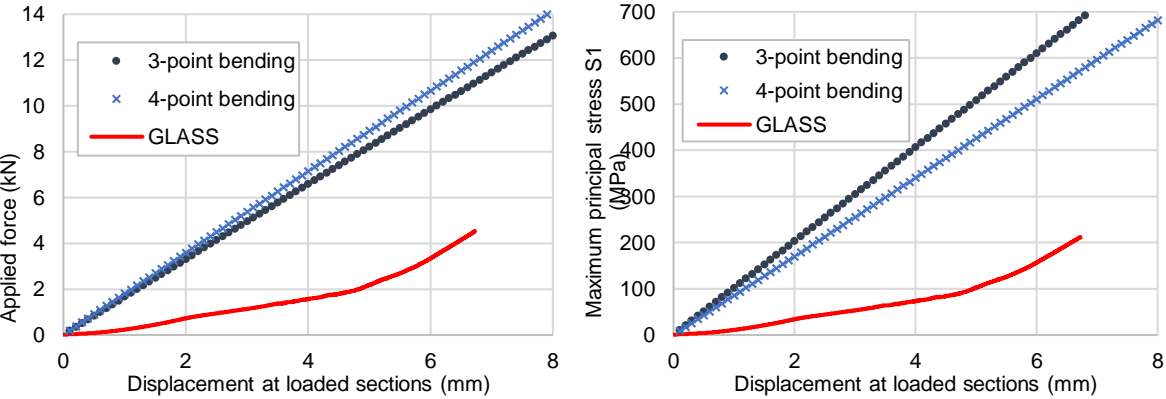


Figure 55 – Total applied force and maximum principal stress S1 vs. cross-head displacement for 3-point and 4-point bending and experimental results for glass

Considering these graphs and the superposition principle, one can conclude that the hypothesis that motivated the analysis would in fact cause the glass to present the two-stage behaviour in terms of stiffness, with the three-point bending displaying a lower stiffness. However, it is also obvious that factors like the rubber bands or the drag caused by the compression of the constraints have a more impactful role.

5.2.3.3. Methodology of the analyses of the lateral-torsional buckling phenomenon

To investigate the lateral-torsional buckling phenomenon a more complex numerical model was developed. The elements chosen for the analysis were curved shell elements (Figure 56), Q20SH (Figure 57), which are also quadrilateral with four nodes, but each has 5 dof $\{u_x, u_y, u_z, \phi_x, \phi_y\}$. To be consistent with the former analysis, the same dimensions were used: square elements with 10,00 mm with 2,00 mm of thickness. The analysis was structural nonlinear, also displacement controlled, with 120 load steps of 0,10 mm, and geometrical and physical nonlinearities were considered.

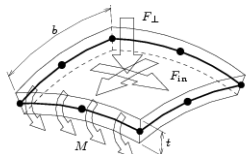


Figure 56 – Scheme of the forces and bending moments supported in a curved shell element (source: DIANA)

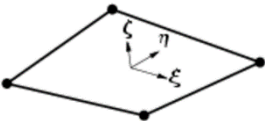


Figure 57 – Nodes and internal axes in a Q20SH element (source: DIANA)

In these analyses, not only the elements changed, but also the FE program used was different: instead of DIANA 9.6, midas FX 2016 (v1.1) was used. This software is developed in cooperation with TNO DIANA, responsible for DIANA 9.6, so no major differences are expected and all the same options were used.

The modelling of the lateral constraint is a rather challenging task: as the lateral plates were not rigidly connected to the specimen and the former can push the plates apart, the most accurate option would be a contact analysis. However, such analysis would greatly increase the complexity of the model and moreover the definition of the interface properties (normal and sliding contacts) would be cumbersome.

Two models were developed, both with the same geometry and boundary conditions of the previous analysis (i), but incorporating the supports on the out-of-plane direction to reflect the conditions of the experimental tests. As illustrated in Figure 58, model A represents the first and second stage of the setup, only with the outer supports, while model B simulates the third and final setup, already with the inner supports. These supports represent the outer and inner supports of the setup, which were fixed. Regarding those supports, it was verified experimentally that they are broad and stiff enough to prevent the specimen's rotation in their vicinity. Therefore, they were modelled as two vertical lines of nodes to block the rotation around it; the same effect could be achieved by constraining the y-rotation; an analysis with only one line of nodes is presented in Appendix C.2. No further lateral constraint was added; this very conservative approach was chosen to demonstrate that, if no buckling happens with so little constraints, then the constraints used are more than enough.

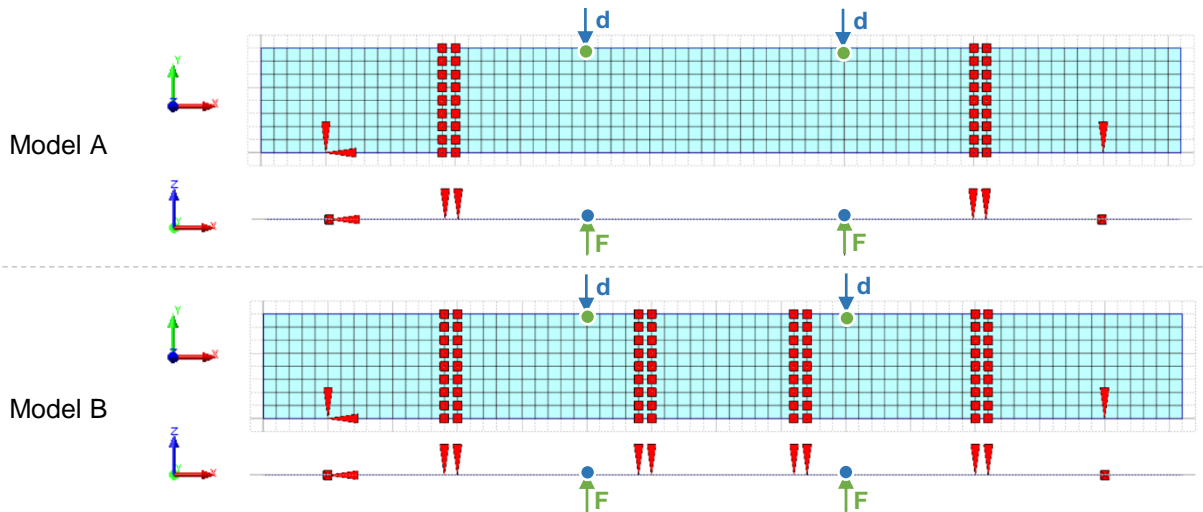


Figure 58 – Model with shell elements and with supports in the out-of-plane direction: only outer supports (A) and both (B)

As mentioned in Figure 49, four analyses were carried out, progressively changing material properties or boundary conditions. Analysis 1 is simply model A with Leoflex glass, done for validation. Analysis 2 and 3 are model A with, respectively, aluminium (yield tension of 150 MPa) and Leoflex glass. These two analyses have a stability analysis consisting in the application of a horizontal force in the out-of-plane direction in each loaded point of 1 N and 100 N (force F in Figure 58), proportional to the displacement, i.e., distributed over the 120 steps. Finally, analysis 4 is model B with Leoflex glass, with the referred stability analysis concerning the applied force.

5.2.3.4. Validation of new model – Analysis 1

The first analysis has the main goal of assessing the effects of using curved shell elements instead of plate stress elements, demonstrating that the results obtained are similar for the same loads and boundary conditions. Figure 59 and Figure 60 show that the results were as expected, without any out-of-plane deformation and with the stresses and applied force corresponding to those of the plane stress model.

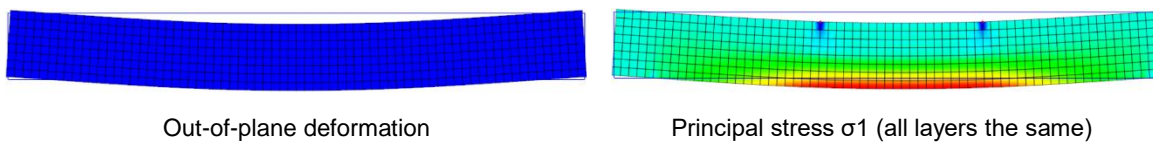


Figure 59 – Results for analysis 1: out-of-plane deformation and principal stress σ_1

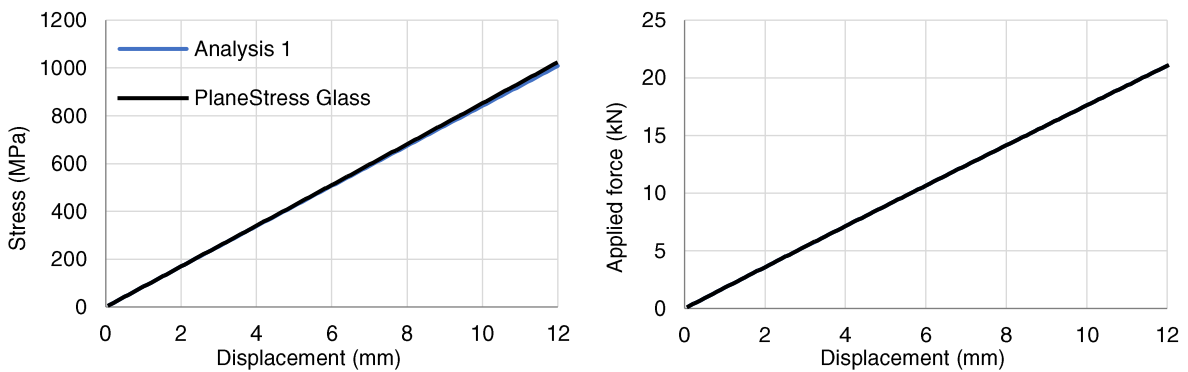


Figure 60 – Comparison of the former plane stress elements analysis with analysis 1 (shell elements)

5.2.3.5. Lateral torsional buckling – Analyses 2, 3 and 4

Analyses 2 to 4 were developed to study the lateral torsional buckling phenomenon and the influence of the lateral supports. Figure 61 compares the results from analyses 2 and 3 in terms of out-of-plane deformations and principal stresses at the outer layers of the shell elements. For these two analyses, a total force of 1 N or 100 N was applied proportionally to the vertical displacement, i.e., distributed along the 120 steps to replicate an eccentric load. At 12 mm of vertical displacement, the difference of applying 1 N and 100 N is no longer visible in the distribution of stresses and in the deformation, so the illustrations of Figure 61 are applicable for both scenarios.

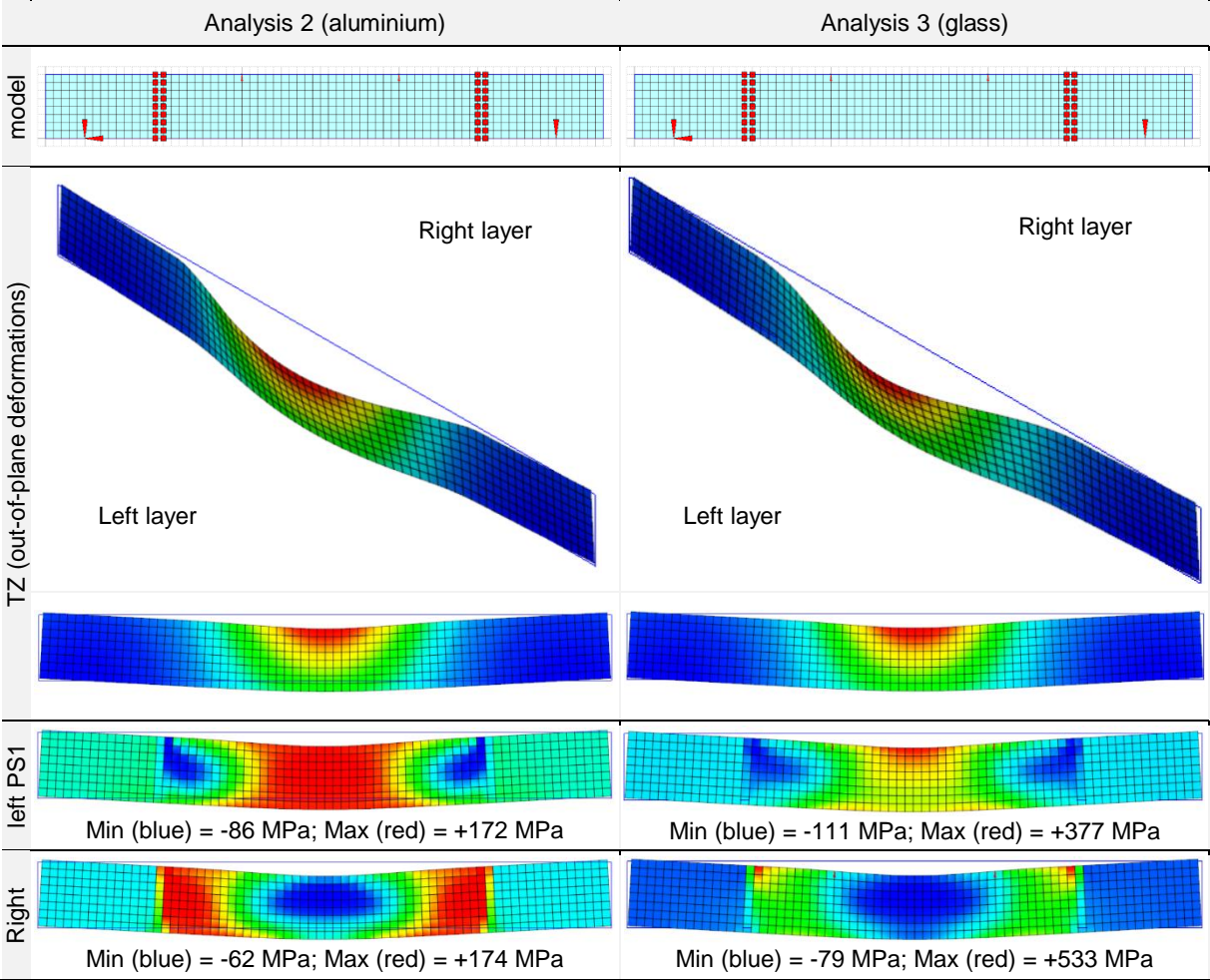


Figure 61 – Analyses 2 and 3: out-of-plane deformations and principal stresses on outer layers of the shell (cross-head displacement 12 mm)

Besides the distribution of stresses being quite different, as expected from plastic and elastic materials, other relevant conclusions can be retrieved from analyses 2 and 3. For the glass plate, after buckling, the maximum tensile stress occurs at the top edge: the maximum is near the supports (right layer) and the second highest value, although fairly lower, occurs at the centre of the buckling span (left layer). For the aluminium, most of the section yields after buckling. Considering Figure 62, it is clear that buckling is affected by the horizontal component of the force and even the upper limit of the vertical force applied, around 700 N for 1 N of lateral force, shows no significant influence of yielding (from the analysis without

torsional buckling, yielding of the aluminium with $\sigma_y = 150 \text{ MPa}$ starts at 4 kN, see Figure 52). Soon after yielding, the yield stress is reached and the behaviour of the materials differs significantly from then on.

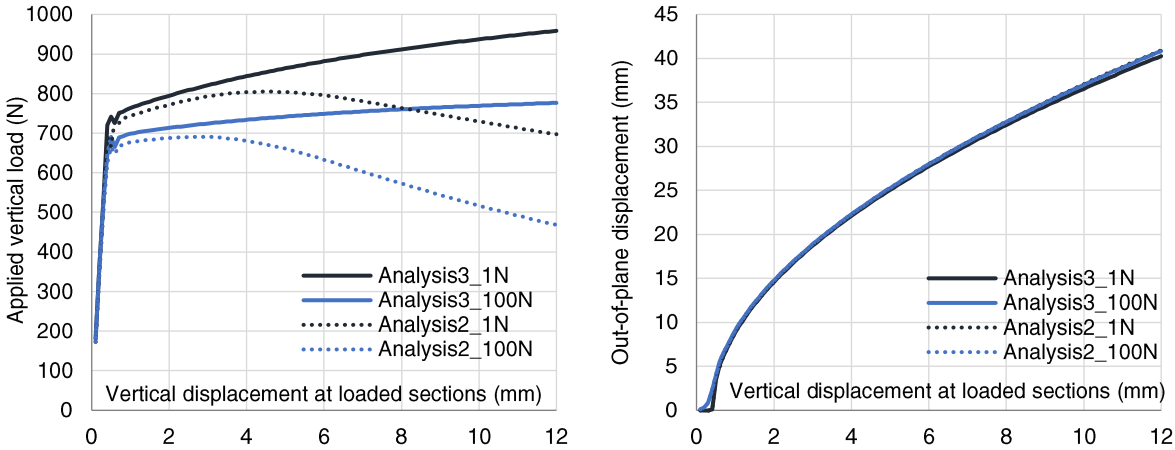


Figure 62 – Analyses 2 and 3: out-of-plane deformations and principal stresses on outer layers of the shell (TZ=12mm at loads)

Analysis 4 introduces the inner supports, therefore changing the configuration of the out-of-plane deformations. Figure 63 and Figure 64 illustrate the out of plane deformations and the principal stresses at a cross-head displacement of 12 mm. A similar stability analysis was carried out, with total out-of-plane forces of 1 N and 100 N distributed over the 120 steps of (vertical) displacement. It is clear that the impact of the horizontal force is drastically more relevant than in the previous analyses: with 1 N, the buckling occurs at more than 5 mm of vertical displacement; for 100 N, out-of-plane deformations are triggered just above 1 mm of vertical displacement. The pre-buckling behaviour obviously follows the linear growth of stresses of analysis 1 at the bottom edge, but after buckling the maximum stresses develop also near the supports (right layer), followed by the centre of the span (left layer) (Figure 64).

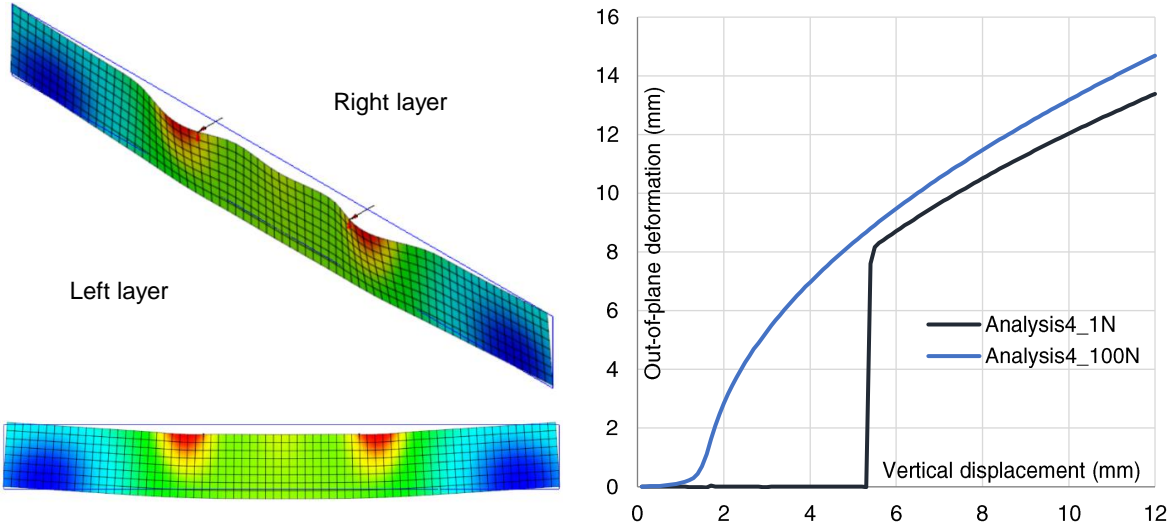


Figure 63 – Analysis 4: out-of-plane deformation at 12 mm of vertical displacement and out-of-plane deformations vs. vertical displacement at loaded section.

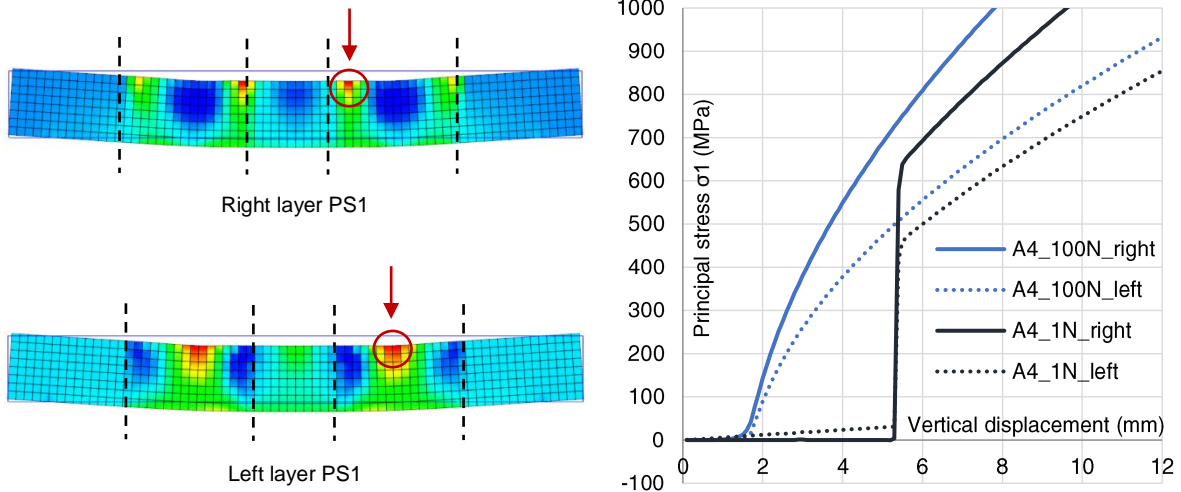


Figure 64 – Analysis 4: post-buckling principal stresses at 12 mm of vertical displacement and principal stresses in points highlighted with an arrow vs. vertical displacement at loaded section.

Finally, the overall comparison of the analyses is presented in Figure 65 and Figure 66, providing a sense of magnitude of the differences of behaviour in terms of applied force and maximum principal stresses. In Figure 66, in order to simplify the graph only the maximum value of the stress for an applied horizontal force of 100 N was considered.

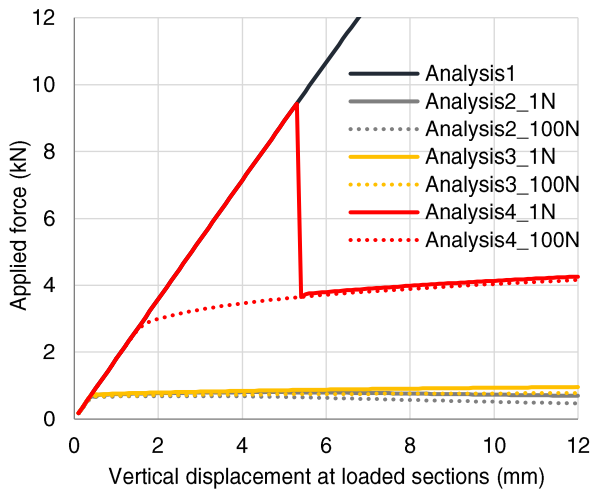


Figure 65 – Overall comparison of the applied force vs. vertical displacement at loaded sections.

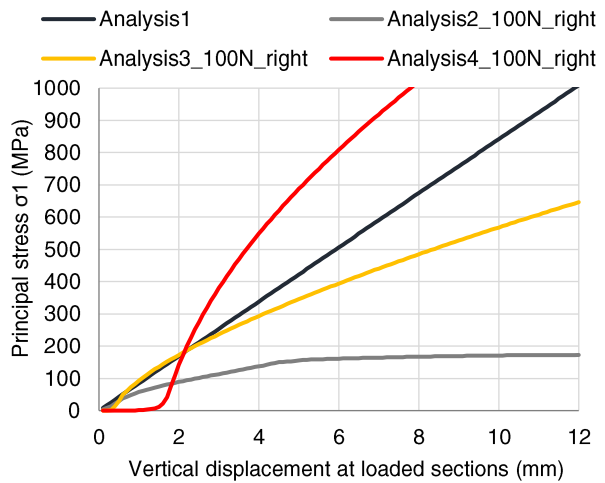


Figure 66 – Principal stress vs. vertical displacement at loaded sections.

These comparisons reveal the influence of the material's properties and of the lateral constraint, as well as the importance of buckling to the stress distribution and applied force. In fact, it is clear the significant range of stresses that buckling causes; provided that the lateral constraint fails to prevent buckling, obtaining valid ultimate strength results with this setup is extremely hard in an experimental analysis.

5.2.4. Proposed setup

It became evident that executing this test is a rather challenging task and that it is prone to many instabilities. Nonetheless, in Figure 67 it is presented a final version of the setup that was built but never tested experimentally, as the samples were spared in favour of the buckling test. While the dimensions are the same as presented previously, the lateral constraints and the axis change.

To sum up, the lateral constraint used in these tests is composed of two plates of aluminium, with 710 mm by 80 mm (same dimensions of the glass plate) and 15 mm of thickness. On the upper part of the plates there are holes with 13 mm of depth (in the centre) where the loads are applied. Between these plates and the glass, stripes of Teflon are glued. The aluminium plates are supported by four steel supports, the outer two being considerably less stiff than the inner two. A rubber band is used on the top and bottom edge of the glass and a transparent foil is glued to one of the surfaces of the glass.

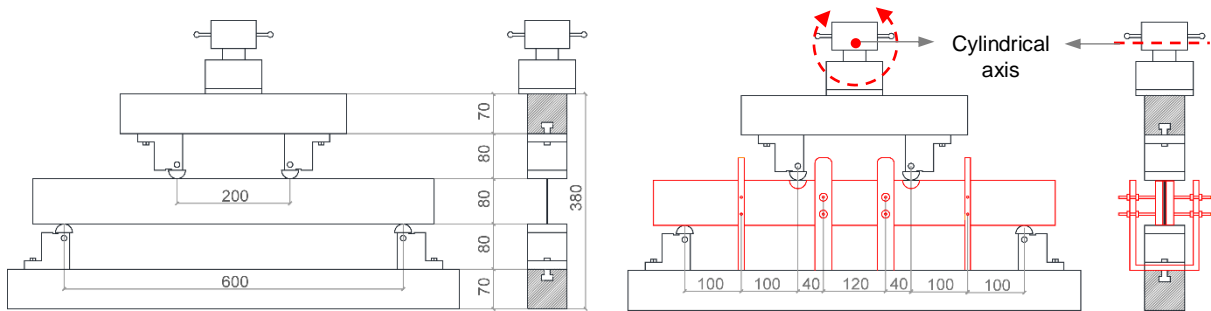


Figure 67 – Proposed setup for the in-plane four-point bending test, front and side view, with focus on the lateral constraint (red)

5.3. Assessment of buckling behaviour in compression

5.3.1. Objectives

The high potential of application of curved or flexible glass plates of large dimensions motivates the interest in studying their buckling behaviour in compression, besides the assessment of the ultimate strength of the material. The study presented in this section includes the assessment of the distribution and evolution of stresses as well as the post-buckling behaviour of thin glass plates and provides valuable insight for these applications. In fact, to achieve or at least maintain those curved conditions, a similar loading to that applied in the tests described herein must be applied and/or sustained.

One of the advantages of this buckling test is the introduction of the maximum stress over a considerable area, in a way that is very similar to realistic applications. It allows assessing the performance of thin glass plates in terms of flexibility and curvature. Regarding the setup itself, it is fairly easy to build and does not require complex testing machines, since only simple compression is applied. Another benefit of the setup is that it is not limited to samples of a specific length or width: the height of the compression machine sets the length upper limit; the width is limited by the width of the rollers.

However, the execution of this test also presents some difficulties or challenges. The centre of the span experiences significant vertical and horizontal displacement, making it complicated to measure out-of-plane deformations without perturbing the test. Due to the high slenderness of the test specimen, flexural buckling starts at very low forces; therefore, a high sensitivity load cell is required to measure the applied force. Finally, when failure is reached, the fracture develops very fast and requires specialized equipment to analyse such occurrence. A protection system is also needed to avoid the spreading of the glass fragments.

5.3.2. Test setup

The buckling test setup, illustrated in Figure 68, consists of a glass plate supported at the top and bottom edges by a cylindrical roller that constrains rotations around all axes but the weakest axis of inertia of the plate. The test itself consists of applying a vertical displacement on the top roller; when a sufficient vertical load is applied, a horizontal force is applied momentarily by hand to impose the direction of buckling towards the intended protected side. The horizontal force is then removed once the vertical compression is enough to keep the out of plane curvature. The vertical compression force, besides the pressure it causes in the whole section, is multiplied by the deformation of the plate and creates a second-order bending moment. Taking into account the reduced thickness of the glass plate and its very high deformations, the second-order moment generates significant stresses over the area around the mid-height of the plate.

The rollers used in the setup are 100,0 mm wide, with 25 mm of radius and contain a 7 mm deep slit (Figure 68). As the glass plate has 710 mm of length, the distance between the centres of the rollers is then 746 mm. The slit is 2,5 mm wide; its depth was limited by technical reasons. Hence, it is easier to insert and remove the 2,00 mm thick glass. For the tests performed, the glass was in direct contact with the metallic roller.

To achieve a stress rate of 2,0 MPa, a displacement rate of 2,085 mm/s was applied. This value was obtained based on the numerical analysis presented in section 5.3.5.

The test was performed on a Universal testing machine *Zwick010*, similar to that previously used for the in-plane four-point bending test (*Zwick100*, see chapter 5.2), but with a maximum force of 10 kN. The machine records the vertical displacement and applied force; however, it is more precise than the other model; previous studies at TU Delft indicate that it also has an accuracy of $\pm 2 \mu\text{m}$ (as the Zwick datasheet states) in displacement, and of 2 N (instead of 5 N) in force.

In addition to the test machine and the setup itself, the test required a protective box to contain the energetic shattering of the glass. In terms of instrumentation, strain gauges were used to register the strains at the centre of the plate and, in some cases, the vertical and horizontal distribution along the plate. Finally, several cameras were positioned to film the test specimens, either focusing on the overall behaviour of the plates or on the area near the rollers.

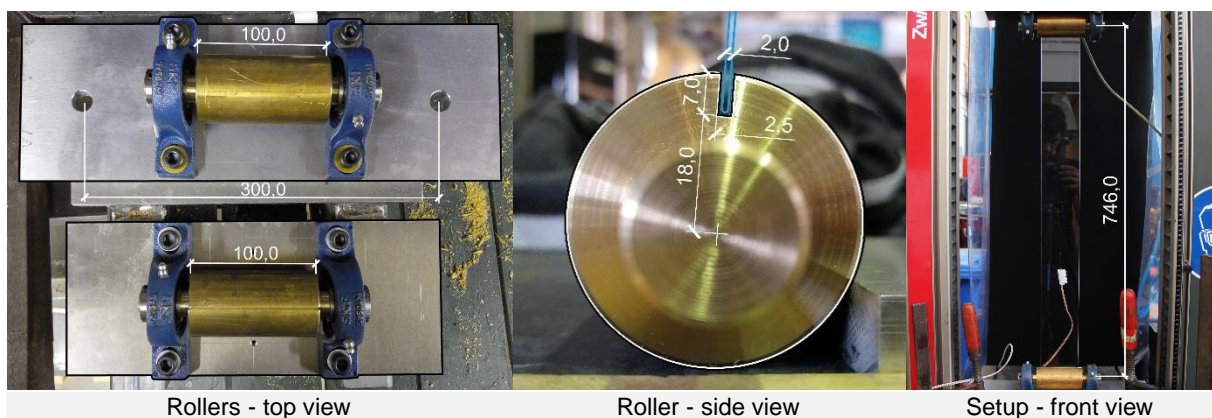


Figure 68 – Pictures of the test setup with dimensions (mm)

5.3.3. Preparation of the tests

5.3.3.1. Preliminary tests

The preliminary setup was exactly as described in 5.3.2, but the slit of the rollers was 2,00 mm wide, matching the samples thickness. No instrumentation was used other than that of the test machine.

For the first experience, an aluminium sample was tested instead of a glass one. Despite the behaviour being very different due to the plastic properties of the metal, the setup worked as expected. For a constant displacement rate set for the sample, the force increased in a first phase, up to 110 N, and then progressively started to reduce (the test was stopped at 68 N) revealing the influence of the physical nonlinear behaviour on the unstable (buckled) behaviour. At this stage, the curvature of the aluminium plate resembled a parabola, with a very pronounced curve at mid-span (Figure 69-a).

As a final attempt, the test was performed with a glass plate, without any strain gauge. In order to recover the shatters and analyse the breakage pattern, a transparent foil was glued only to the inner (compressed) side of the glass to have the least influence possible on the plate. An improvised protection made out of three acrylic panels was placed around the setup, and the plate buckled towards the wall of such protection. A slow displacement rate of 0,40 mm/s was applied. The glass collapsed when the applied force was 84,85 N and the vertical displacement was 292,66 mm. For the same vertical displacement, the glass plate displayed a more uniform curvature than aluminium, almost circular, as the comparison in Figure 69 shows.

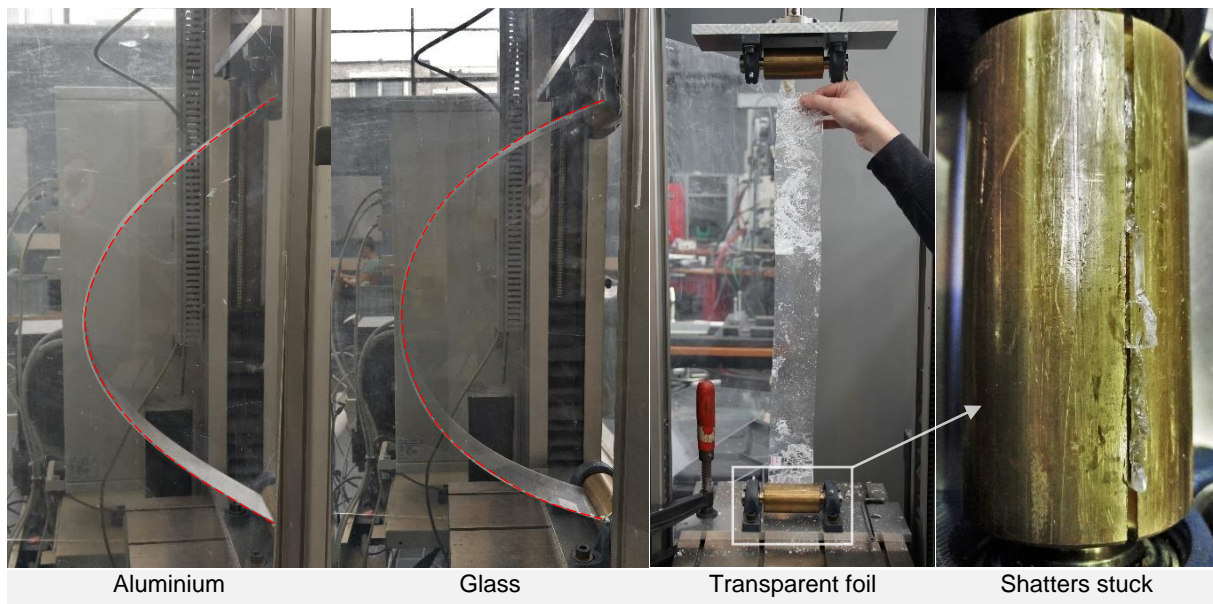


Figure 69 – Buckling shape of (a) aluminium and (b) glass specimens

Figure 70 – Shatters of glass in the foil and roller

A few conclusions could be drawn from this preliminary test: the shatters of the glass were clamped in the rollers' slit and were very hard to remove; the extremely energetic collapse of the glass plate was not contained by the simple improvised box and some small particles flew several meters; finally, less than 10% of the glass remained in the transparent foil, making it useless.

The slit was thus enlarged from 2,0 mm to 2,5 mm. Indeed, besides being impossible to remove the small broken pieces after breakage, it was not easy to insert the glass into the slit in the first place, leaving some visible marks on the aluminium sample. However, this widening had an important consequence: the glass is no longer fully clamped inside the roller, since some (limited) movement is allowed.

A new protective box to contain the collapse was also designed and built. It consisted of four wooden beams with a squared section of 45 mm per side, forming a rectangle of 600x500 mm². One of the rectangle's small side was clamped to the top of the Zwick machine, leaving the rest hanging on top of the setup. The other end supported a black cloth 500 mm wide and 1200 mm long. The remaining two sides had a transparent plastic 400 mm wide and 1200 mm long. The top was covered by transparent foil. Finally, the front consisted of an acrylic panel, easily removable to access the setup.

5.3.3.2. Instrumentation and equipment

To study the behaviour of the glass plate, the required data to be recorded was the applied displacement and corresponding vertical force, and the strains, complemented with videos to register their overall deformation and failure mode. Accordingly, the instrumentation set consisted of the compression machine *Zwick 010* itself, strain gauges and cameras.

As mentioned, the machine *Zwick 010* measures automatically the vertical displacement and the applied force. However, it does not provide the option to synchronize such measurements with external devices, such as the strain gauges. Moreover, it does not measure horizontal displacements, which are difficult to measure due to the considerable vertical displacement. For that purpose, some solutions were studied: the use of laser sensors; the use of wire LVDTs (horizontally positioned at the beginning of the tests) and the triangulation of their results; a camera recording a side-view with a ruled background. The laser sensors had the problem of following the moving point; this could be manageable by moving the laser accordingly but this procedure would certainly affect the accuracy of the measurements. The LVDT option seemed practical and interesting, with the vertical displacement measured by the Zwick helping the complex processing of the results, but would possibly interfere with the buckling behaviour by introducing a non-controlled force to the side of the plate. The camera option was also dismissed due to its evident imprecision. It is also worth mentioning that none of the above mentioned solutions could be actually tested as the corresponding devices were not available at the time of testing.

The strain gauges used are manufactured by *Tokyo Sokki Kenkyujo Co., Ltd.*, type *FLA-10-11*. The gauge length is 10 mm and the gauge resistance is $120 \pm 0,3 \Omega$.

For data acquisition, a 24-Bit Universal Analog Input *NI 9219*, manufactured by *National Instruments*, was used. This device has four analogue input channels able of two measurements per second using either one or three channels (Figure 71). The software used to record the data, *Mp3*, was developed by TU Delft.

To apply the strain gauges to the glass, a common method consists in creating a rougher surface by either mechanically scraping the surface or applying an acid. However, this method is not applicable in this case, as the chemical temper (a very thin layer) would be damaged. Instead, an adhesive based on cyanoacrylate produced by *Tokyo Sokki Kenkyujo Co., Ltd.* was applied directly on the surface. Cleaning

of the surface is essential, and the remaining methodology is briefly illustrated in Figure 72. After welding, all strain gauges were verified with a multimeter.

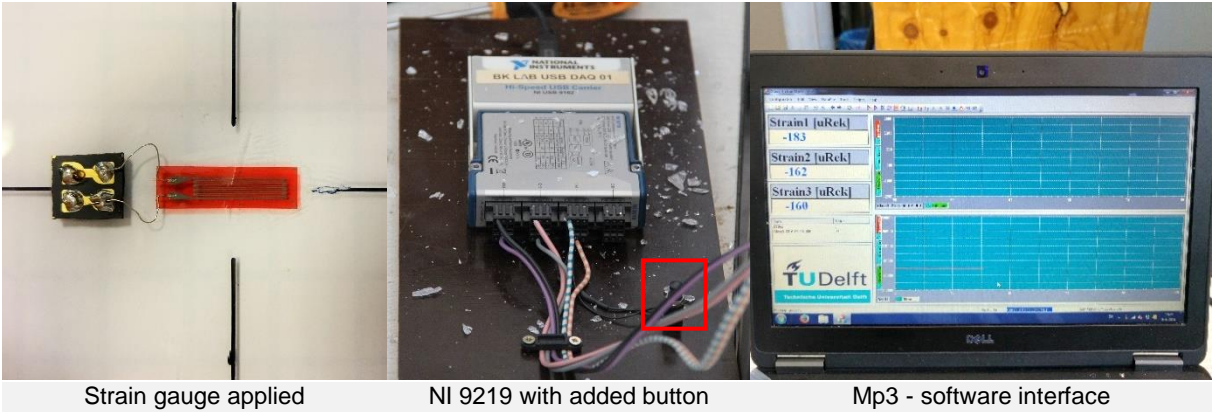


Figure 71 – Strain gauge and corresponding hardware and software

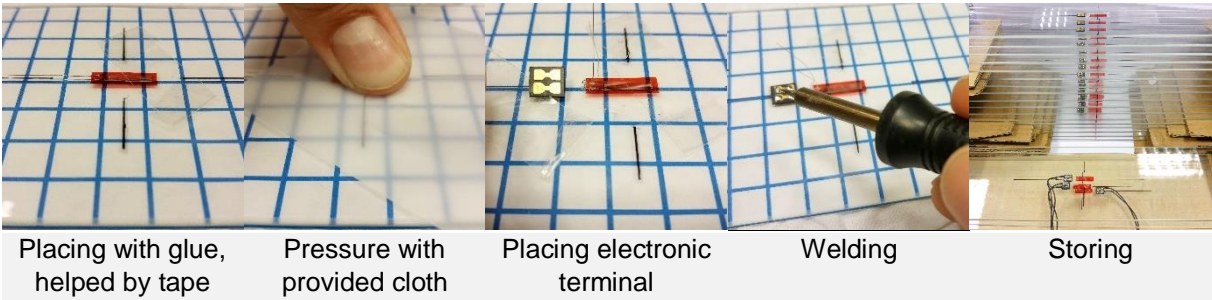


Figure 72 – Application of the strain gauges

Strain gauges were applied in 20 plates: 18 plates had a single strain gauge at the centre; then, two plates had, besides the central one, two more gauges: in one of the plates these additional gauges were distributed horizontally (at mid-height at both lateral edges, at the boundary of the flat surface), whereas in the other one they were aligned vertically (located 100 mm and 200 mm below the centre).

Of the 20 plates prepared, 11 were tested until failure (see 5.3.4); of those, 9 had one strain gauge only, identified as T.1 to T.9; the other 2 plates were the ones where vertical and horizontal strain profiles were measured. The latter two samples are identified differently: instead of just T and its order number, they also have a 3 in their nomenclature (number of strain gauges) and a V or H, standing for vertical or horizontal profile, respectively.

In order to synchronize the strain measurements with the force and displacement, a button was added in the DAQ board to emit a defined strain signal to channel 1, marking the beginning of the test (highlighted with a red square on Figure 71). Then, further matching is done using the time elapsed in both software records. Measurements with strain gauges were taken at 2 Hz, while the Zwick measurements started with intervals of 0,02 s and were quickly switched to 0,01 s. The collapse of the sample could be instantly and obviously visible in both measurements by a sudden drop of force and either an inconsistent value in the strain gauges or a drop as well. The strain values were zeroed so that a standing plate just before the loading started had a value of zero. The spike caused by the button was helpful to verify both this synchronization and the calibration.

To record the tests, several cameras were used: two Canon EOS 550D, one GoPro HERO4 Black, one UMOX SJ4000 camera and a LG G4. Two dispositions were used, being the focus of the first the overall behaviour (front and side view) and of the second the area near the two rollers.

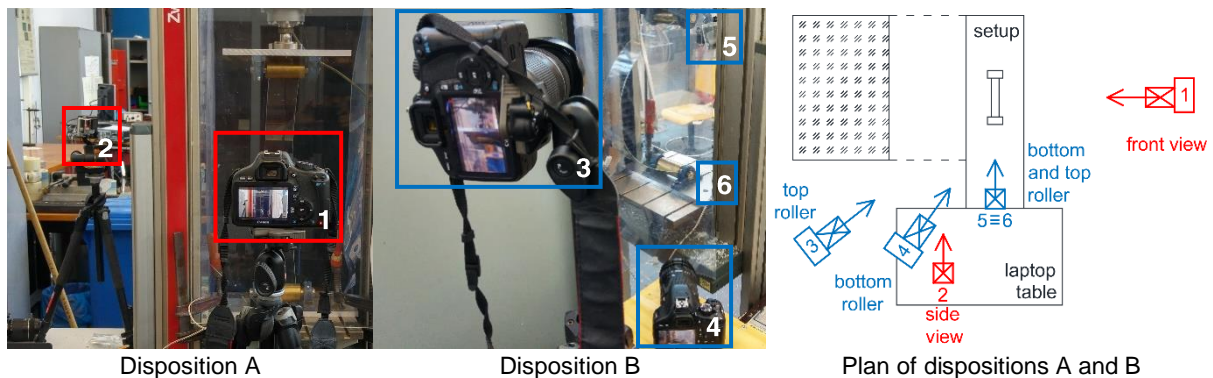


Figure 73 – Two dispositions of cameras used to record the test

Ideally, high speed cameras would record the test so that the fracture development would be visible and possible to study. Unfortunately, none was available and the maximum speed used to record the test was 60 fps. At this speed, it is very hard to visualize the start of the failure, which would be very useful to check the good behaviour of the setup, causing the plate to break at mid-span, or if concentration of stresses at the rollers triggered the collapse of the glass.

5.3.3.3. Test conditions

The tests were neither temperature nor humidity controlled and, at the testing site, temperature was 24,8°C and relative humidity was 37,7%.⁹

5.3.4. Experimental results

This section starts with a study on the behaviour of the sample in function of the vertical displacement; then, the distribution of strains/stresses in a vertical and horizontal axis is investigated; the stress rate of the overall test is also shown and an analysis of the ultimate strength at failure is analysed. Finally, selected photographs and frames of videos are shown to illustrate the test and complement the analysis.

With the results from the Zwick compression machine, a force vs. vertical displacement graph was prepared (Figure 74). The graph shows a remarkable coherency of the obtained results in terms of behaviour. The vertical force progressively increases before any significant vertical displacement, and the peaks of applied force occur in the first 0,15 mm – at this stage, the plate was under pure compression. Then, the force varies due to the start of the flexural buckling, which was manually imposed when enough compressive force was applied. This is visible at the first millimetres of the graph, stabilizing shortly after (see Appendix D.1). Since the test was conducted under displacement control, the sudden increase of displacement causes a sudden drop of force applied.

⁹ The temperature and humidity values were not registered for the four-point in-plane bending test, as it was not performed a final test but only preliminary tests, mostly on aluminum.

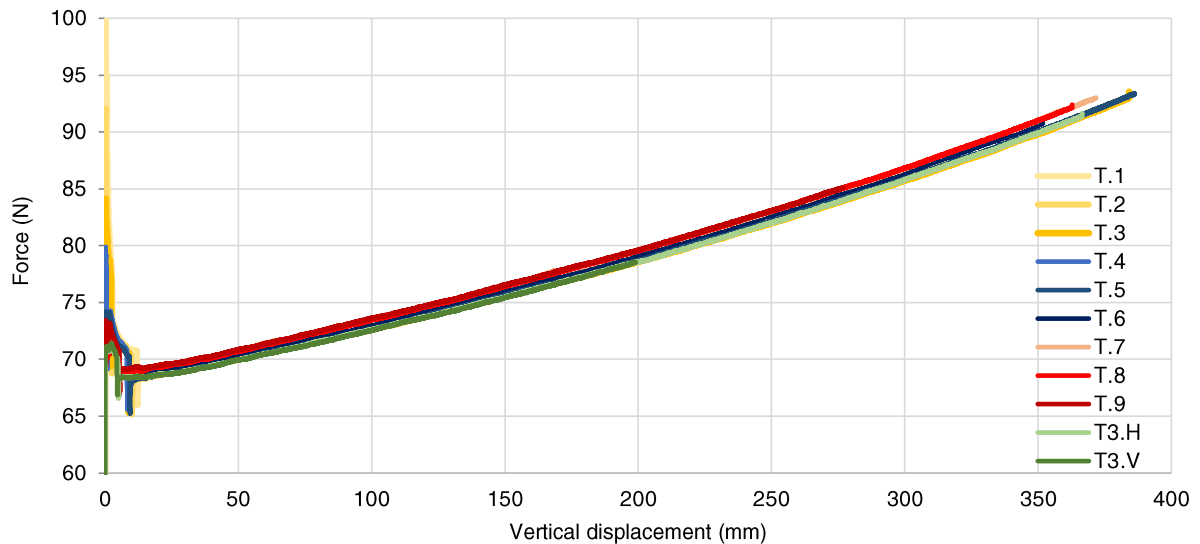


Figure 74 – Applied force in function of vertical displacement

The deformation measurements obtained with the strain gauges were converted to stress by applying the Hooke's Law. To this end, the Young's modulus considered was 74,0 GPa, as stated by the manufacturer (AGC). Figure 75 shows the stress-displacement graph obtained with the strain gauge at the centre of the plate for all the 11 samples. Once again, the results were very consistent among the different replicate tests. For the first millimetres of vertical displacement the stress increases rapidly and after around 100 s of testing, or 200 mm of vertical displacement, the stress rate stabilizes. In fact, this is explained by the relationship between the vertical displacement and the horizontal one (or out-of-plane deformation, see 5.3.5): for the first millimetres of vertical displacement there is a high increase of out-of-plane deformation. This deformation is multiplied by an almost constant force, thus being the main contributor to the bending moment increase.

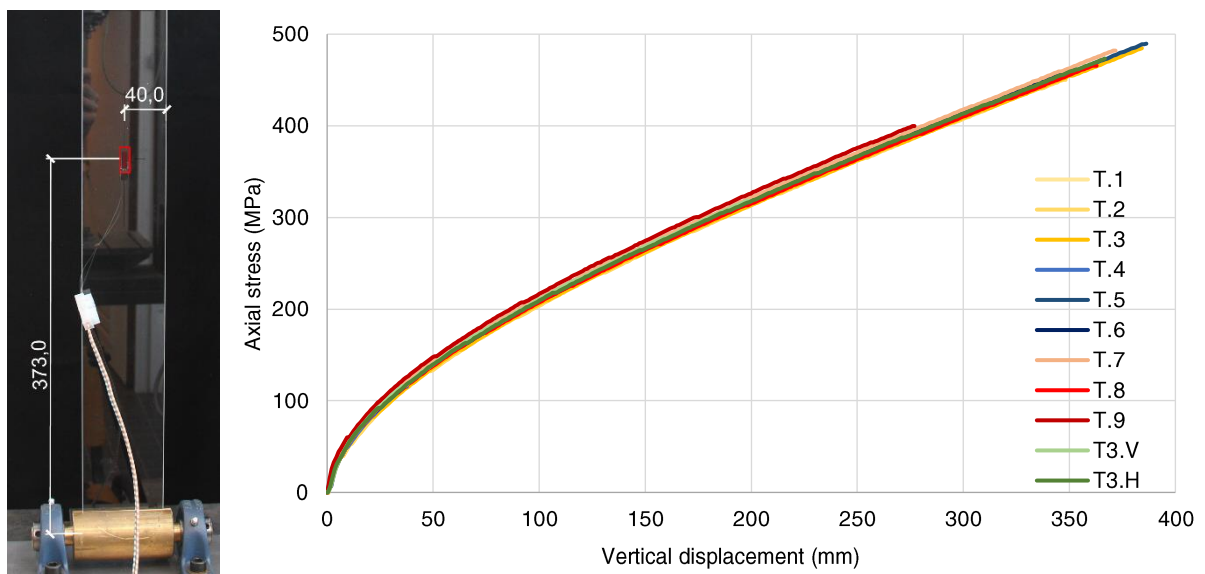


Figure 75 – Stress at centre of outer surface (strain gauge) in function of the vertical displacement

Analysing the vertical distribution of stresses (Figure 47), the highest values of stress develop at the centre of the panel, as expected, and the reduction of the stress along the profile is also verified. For

this test, the collapse was relatively premature, at 199,06 mm of vertical displacement or 318,24 MPa of axial stress, which to some extent limited the data available. One interesting result is that the axial strain rate increase varies proportionally to the distance from the supports – the highest rate occurs at the centre of the plate. To sum up, there is an accumulation of stress at mid-height as the test develops.

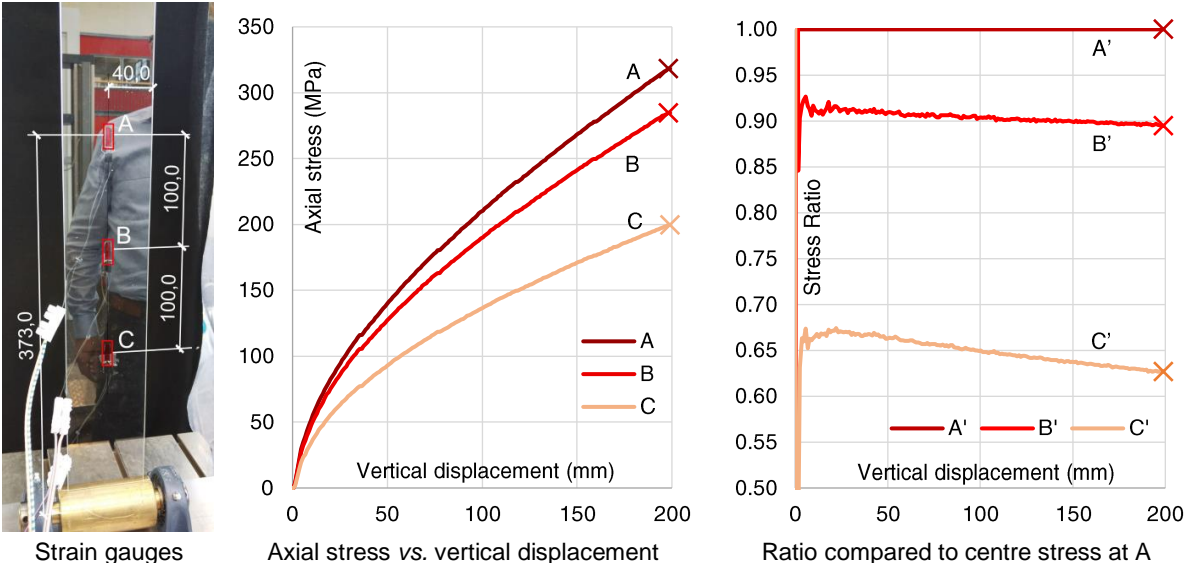


Figure 76 – Vertical distribution of axial stress along the plate's longitudinal axis as a function of the vertical displacement (T3.V)

Regarding the horizontal distribution of strains/stresses at mid-span, the most outstanding result is that near the edges the stress is considerably higher than at the centre (Figure 77). The ratio between the strains/stresses at the edge versus at the centre increases very rapidly from 1,00 to around 1,17, and then progressively reduces until the collapse of the plate occurs, when this ratio is around 1,09. It would be interesting to understand how this ratio would continue to vary if the material strength or the setup itself would not be a limit.

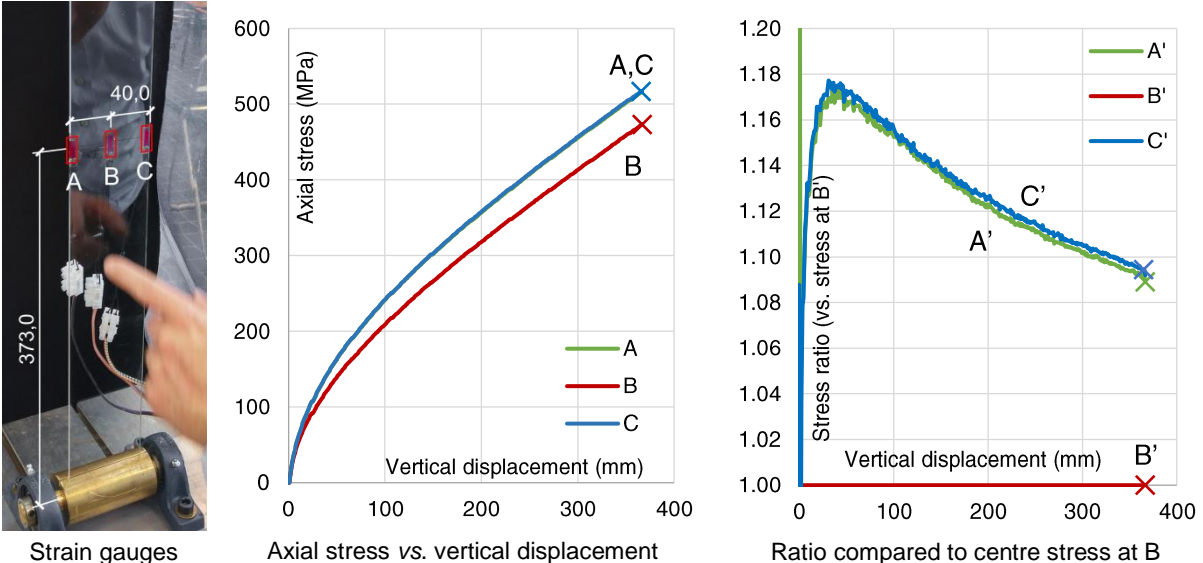


Figure 77 – Graphs of ultimate values of stress and force in function of the vertical displacement (T3.H)

It is worth mentioning that the displacement rate used (2,085 mm/s) proved to correspond to the intended stress rate of 2,0 MPa/s. In the first stage of the test, a much higher stress rate occurred, as

explained before, but from an axial stress of 200 MPa up to the failure of the samples the planned stress rate was kept roughly constant and as planned, presenting only a very slight reduction (Figure 78).

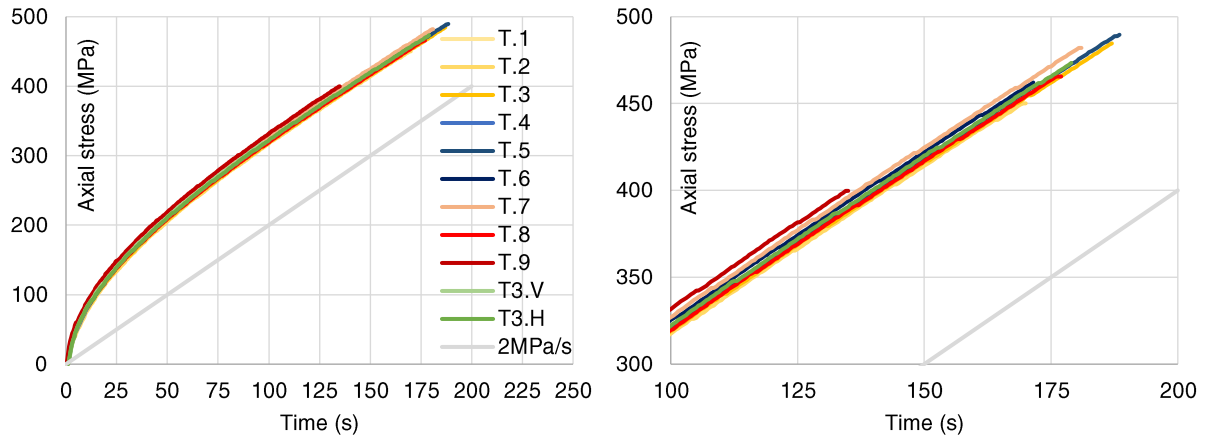


Figure 78 – Stress rate of the overall test and detail of the near-breakage area

Finally, in terms of failure behaviour, Table 10 presents the ultimate values obtained, both the averages and the standard deviations. Figure 79 presents the distribution of ultimate values of both force and stress as a function of vertical displacement. The sample T.4 was clearly an outlier and it was not considered for the statistical analysis of ultimate values; even the shatters size it originated were orders of magnitude above the remaining. The time presented was measured in units of half a second because of the synchronization: the ultimate value of force and displacement was set as the last time of the strain gauge measurements (accurate results were obtained until the end of the test).

Table 10 – Ultimate values of displacement, force, strain and stress for each test

SG	Test time (s)	Vertical displac. (mm)	Vertical force (N)	Axial strain ($\times 10^{-6}$)	Axial stress (MPa)
T.1	153,00	314,04	86,97	5686,74	420,82
T.2	170,00	348,23	89,75	6082,77	450,12
T.3	187,00	384,20	93,54	6549,31	484,65
T.4	19,00	37,59	69,81	1559,45	115,40
T.5	188,50	386,32	93,36	6616,69	489,64
T.6	171,50	351,83	90,75	6245,36	462,16
T.7	181,00	371,79	93,01	6514,13	482,05
T.8	177,00	362,86	92,40	6291,85	465,60
T.9	135,00	276,98	85,11	5402,26	399,77
T3.V	97,50	199,06	78,54	4300,53	318,24
T3.H	179,00	366,73	91,65	6397,88	473,44
Average	163,95	336,20	89,51	6008,75	444,65
Std Deviation	27,00	55,60	4,52	678,22	50,19

It should be noted, however, that the axial strength values are not representative of the ultimate tensile strength of the glass, because the hereby presented values may have been limited due to test setup restrictions. The actual glass strength values are expected to be significantly larger.

The average ultimate strength obtained in the centre strain gauge of the 10 samples considered is $\bar{x} = 444,65$ MPa, with a standard deviation $\sigma = 50,19$ MPa (coefficient of variation of 11,3%). The maximum value is 489,64 MPa and the minimum one is 318,24 MPa, with 7/10 samples presenting maximum stress above 450 MPa. Assuming a normal distribution, the characteristic value of the maximum stress is $f_k = 362$ MPa.

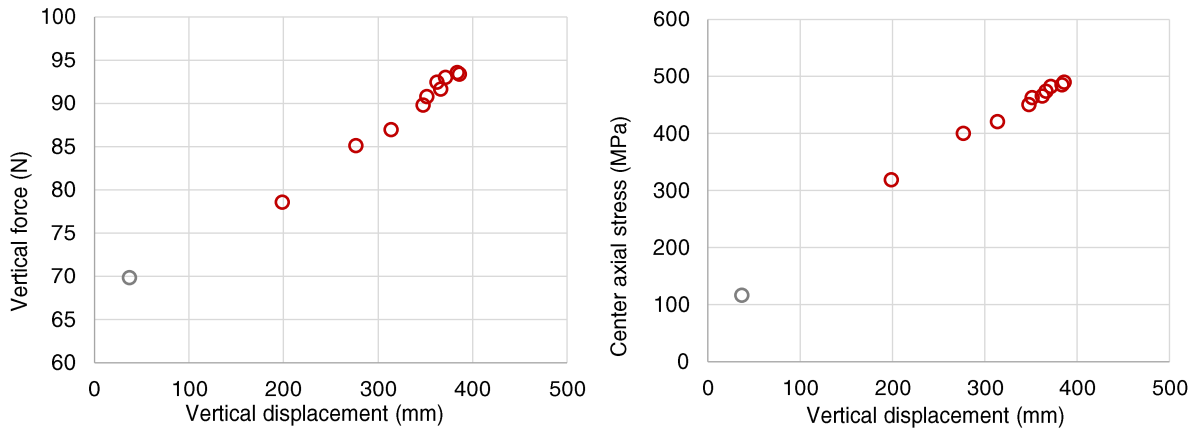


Figure 79 – Graphs of ultimate values of stress and force in function of the vertical displacement

Taking into consideration that the stress at the edges is 1,09 times higher than at the centre near the collapse (T3.H sample broke at 473 MPa), those values could be multiplied by this coefficient to determine the ultimate stress reached with this test: hence, $\bar{x}_{max} = 485\text{MPa}$ and $f_{k,max} = 394 \text{ MPa}$.

Despite only 10 tests performed, a 2-parameter Weibull distribution was also used to describe the above mentioned maximum stress values. Equation (5) presents the cumulative distribution, where σ_0 is the characteristic stress and m is the measure of the strength variability.

$$F(\sigma; \sigma_0; m) = 1 - e^{-(\sigma/\sigma_0)^m} \quad (5)$$

The parameter estimation was performed as described in Vallée *et al.* (2006) and as illustrated in Figure 80. For the experimental values obtained are $\sigma_0 = 471,69 \text{ MPa}$ and $m = 7,89$; once more, note that these are a lower bound of the actual tensile strength of the thin glass tested. These values correspond to the cumulative distribution depicted in Figure 81, in which a probability of 5% is achieved for a stress of $f_{k,5\%} = 325 \text{ MPa}$. The coefficient to the edges was not used for this distribution, but if applied it would lead to a characteristic stress of $\sigma_{0,max} = 514 \text{ MPa}$.

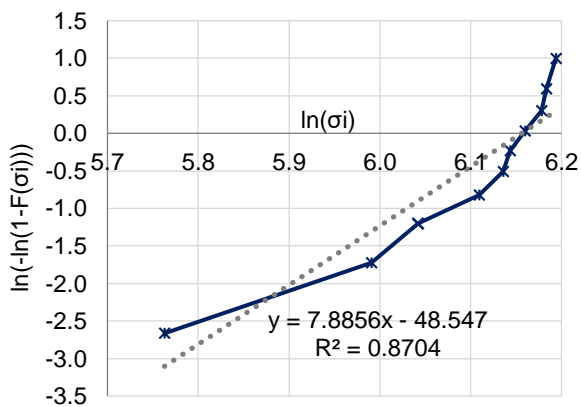


Figure 80 – Parameter estimation plot for Weibull 2P distribution

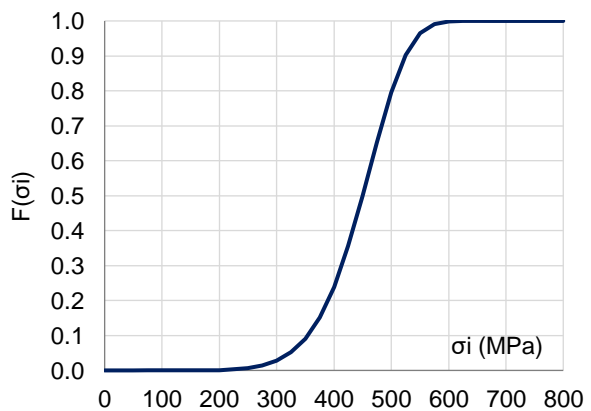


Figure 81 – Weibull 2P cumulative distribution with estimated parameters ($\sigma_0=471,69 \text{ MPa}$; $m=7,89$)

Regarding the failure modes, the cameras were also useful to understand what happened in the tests, particularly regarding the behaviour of the tested samples, evidencing their flexibility and the energy released at collapse. Some videos were selected and are presented in the Appendix D.2 to give an overall impression of the failure behaviour and the collapse.

The videos of the GoPro camera were too affected by a wide angle distortion (fisheye) for a direct analysis. In fact, those videos suggested a completely wrong behaviour with the opposite curvature to what was intended (see Appendix D.2). The frames presented in Figure 82 were processed in Adobe Photoshop to correct that effect, and the difference is particularly noticeable in the straight lines of the Zwick machine. These frames are shown as they illustrate the behaviour near the rollers, the critical points of the setup design. Although the curvature is not obvious due to the small length focused on the camera, it suggests that the plate buckled as expected even near the rollers. This is confirmed in the other videos. One detail worth mentioning is that the plate had one or two abrupt movements, explained by adjustments in the slit of the roller.

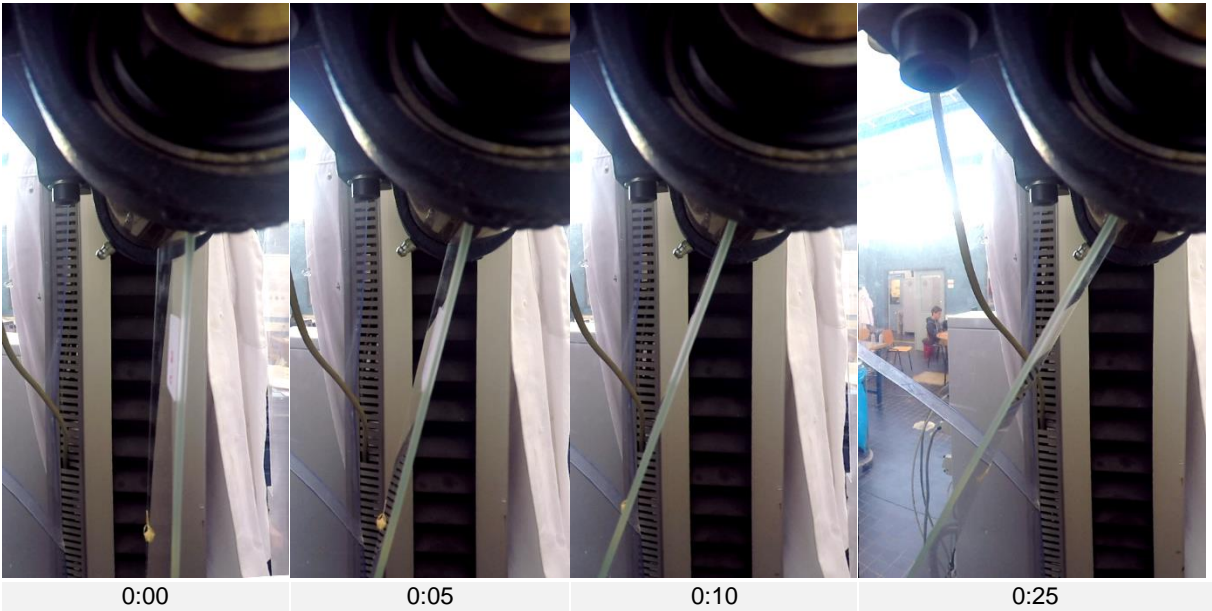


Figure 82 – Frames of GoPro video focusing on top roller - first seconds [camera 5]

Regarding the collapse, it is very difficult to understand from any of the videos where the fracture actually started. Figure 83 shows the collapse of the same sample as in Figure 82. From the Appendix D.2, Figure D-6 is where the fracture seems more noticeable, starting at both rollers and revealing an unaffected mid-span.

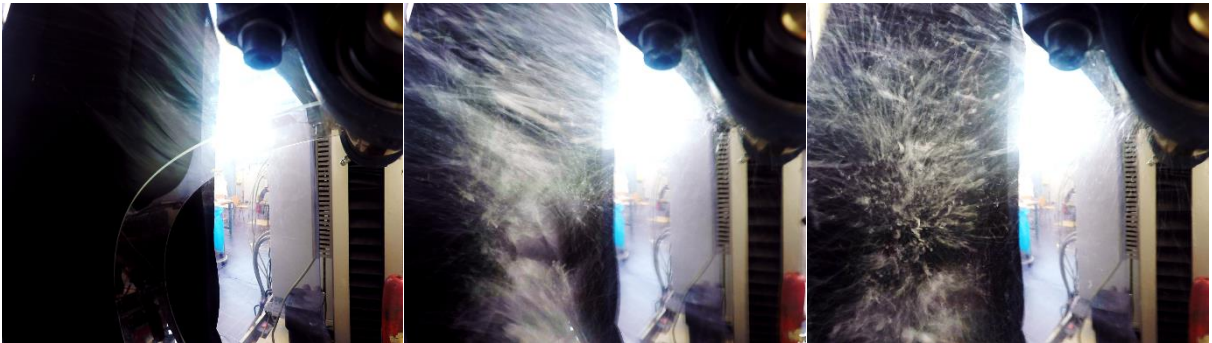


Figure 83 – Frames of GoPro video focusing on top roller - collapse [camera 5]

To conclude the analysis of the collapse, although the breakage of the glass plates was quite violent, the size of the shatters was rather small and almost powder-like, which is desirable for glasses. Figure 84 shows pictures of those shatters with objects that help to scale.



Figure 84 – Shatters after breakage of glass: detail with a 6cm diameter lens cover and with a 1cm strain gauge

5.3.5. Numerical analysis

5.3.5.1. Objectives

The main goal of the numerical analysis presented in this subsection was to simulate the experimental tests presented above and to obtain a better understanding of the behaviour of the tested plates. In fact, comparing numerical and experimental results draws insightful conclusions on the behaviours observed as it provides more data and the assumptions considered in the numerical analysis are clearer.

5.3.5.2. Modelling

The FEM software used was “DIANA Release 9.6” and the models were pre and post-processed in “midas FX+ for DIANA version 3.3.0”.

For simplicity, this analysis considers that the whole length of the glass plate between the centre of the rollers behaves in a uniform way, neglecting the transition at the slit. In fact, near the rollers the stresses are not significant, since the out of plane deformation is small, so this simplification should not have much influence. As such, a continuous element of 746x80x2 mm³ was used to model the glass plate.

For the analysis, the same finite elements used in 5.2.3 were chosen: quadrilateral curved shell elements, Q20SH regular, with four nodes, each with 5 dof $\{u_x, u_y, u_z, \phi_x, \phi_y\}$. The mesh consisted of squares of 10 mm. Figure 85 illustrates the model and presents the axes notation. Regarding the boundary conditions, the displacements are constrained as follows: x-direction - in a line of nodes in the bottom end (left edge in Figure 85); y-direction - in a single node in each end; z-direction - in the line of nodes at both ends of the plate. In terms of loads, an initial deformation was introduced by applying an out-of-plane (in the z-direction) point load at the centre of the plate, thus inducing the consequent buckling, which was then caused by an in-plane displacement (in the x-direction) applied at the top end.



Figure 85 – Geometry, mesh and boundary conditions for the buckling model

The analysis was nonlinear and the size of the load steps had some influence, particularly at the very beginning of the loading stage. Therefore, firstly, the centre force was applied in one step only, followed

by the application of the vertical displacement, in this case first in 100 steps of 0,10 mm and then in 690 steps of 1,00 mm, totalizing 700 mm of vertical displacement. The smaller load steps at the beginning are justified by the start of the instability, where each millimetre of vertical displacement has more impact on the applied force, out-of-plane displacement and stresses. The centre force applied is 1 N, causing an out-of-plane deformation at mid-span of 1,1 mm. This value was determined based on a preliminary study concerning the influence of the initial imperfection.

For the study of the initial imperfection, three different values of out-of-plane deformation were compared: 1,00 mm, 5,00 mm and 10,00 mm (Figure 86). Firstly, a linear analysis was performed by imposing a displacement and retrieving the equivalent value of the (reaction) force. Then, as applying a displacement “locks” the nodes to that position afterwards, that force was applied to cause the corresponding deformation. Finally, a vertical displacement on the top nodes of the plate was applied in 500 steps of 1,00 mm for each of the three values of horizontal force. Considering the production technique, the careful quality control and its stiffness, the initial imperfection is rather small, so the value of 1 N was chosen. This load of 1 N causes an out-of-plane deformation of 1 mm at mid-height, or a deformation-to-length ratio of $1/746=0,0013$.

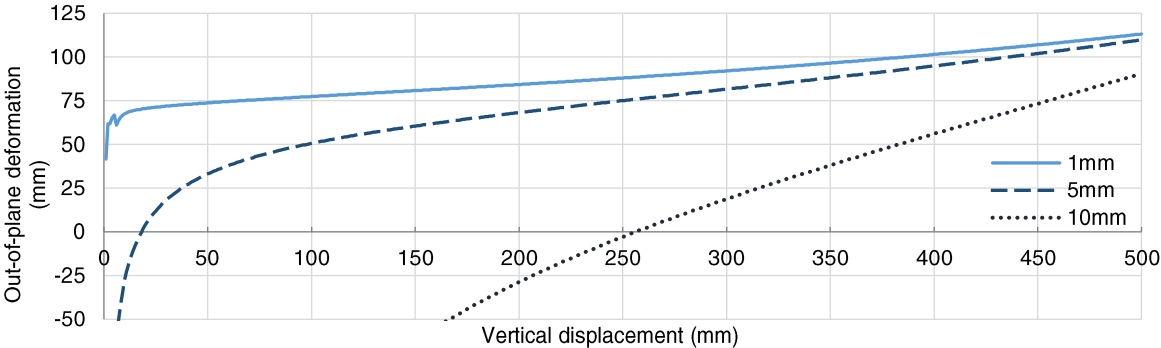


Figure 86 – Study on the initial imperfection

5.3.5.3. Numerical results

The numerical results provide valuable insight on the out-of-plane deformation, which could not be measured in the experiments. Figure 87 shows the out-of-plane deformation at mid-span as a function of the vertical displacement. There is a negligible relative difference of around 0,10 mm between the out-of-plane deformations in the centre of the section compared to the edge, which remains almost constant throughout the whole analysis. An important observation is the very steep increase of deformation for the first 50 mm of vertical displacement.

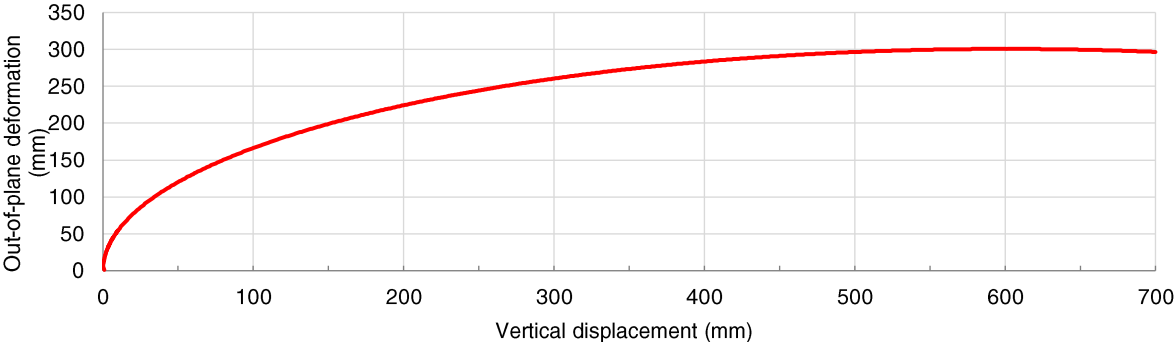


Figure 87 – Out-of-plane deformation at the centre versus vertical deformation

Figure 88 illustrates the deformation with a side view, produced with the post-processor “midas FX+ for DIANA” with the “actual deformation” option. A qualitative view of the principal stresses σ_1 is also added to each position to complement the graphs presented later; in Figure 88, the blue represents no tension and red the maximum tension, which is presented below for each case. Some important data can be retrieved from these numerical results: no compression occurs at the outer layer of the shell element, only tension; the length that is subjected to very high stresses is much longer than just the mid-height area of the glass plate; there is a significant accumulation of stresses in the edges compared to the centre, which is gradually dissipated as the deformation increases; there is not a significant curvature near the rollers, which present a rotation of around 90° at 400 mm of vertical displacement; at the end of the analysis, at 700 mm of vertical deformation, the rollers almost touch each other, presenting a rotation angle of 125° .

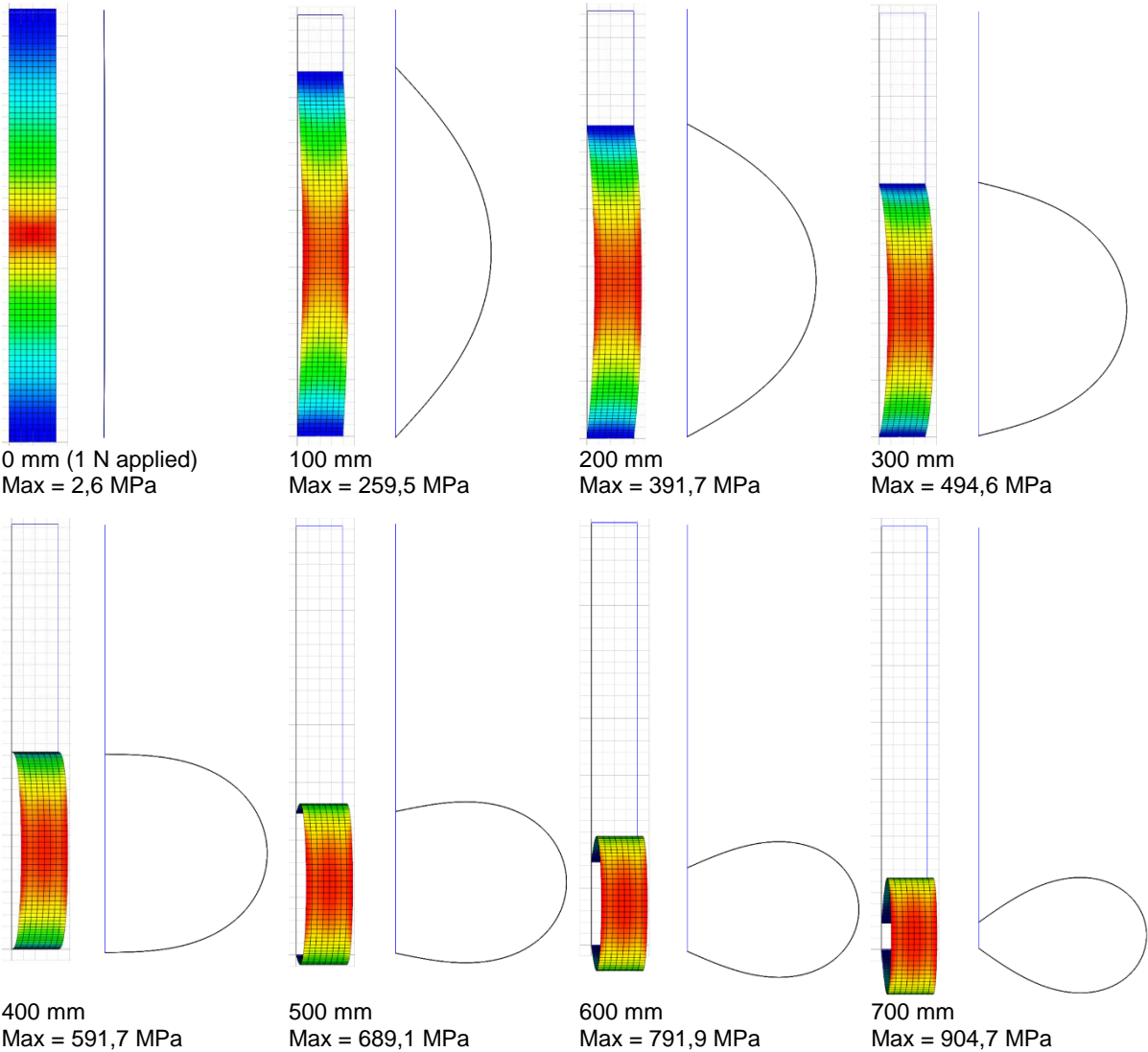


Figure 88 – Side view of the plate deformation and 3D view of principal stress σ_1 , along its vertical deformation

In terms of force, the numerical model presents slight differences of behaviour comparing with the experimental results (Figure 89), particularly regarding the triggering of instability. For both experimental and numerical data, buckling starts at around the same applied force, but while experimental results

reveal an increase of force and then a sudden drop with the buckling, the numerical results initially present a lower force with a much smoother increase of deformation. Then, the behaviour stabilizes and the curves become almost parallel, with an offset of around 5,5 N to 6,5 N. It is noteworthy to mention that the overall behaviour reflected by the experimental and numerical curves is consistent with the (expected) stable buckling behaviour of an elastic material.

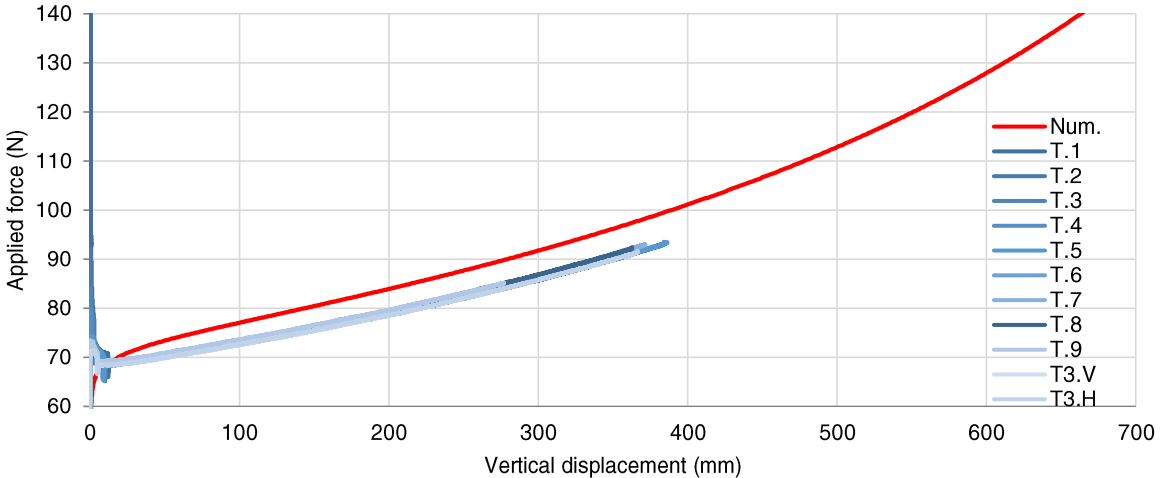


Figure 89 – Applied force vs. vertical displacement, comparison of numerical and experimental values

In terms of axial stress, the numerical behaviour seems remarkably close to the experimental results, as presented in Figure 90. However, as depicted in Figure 91, a more detailed analysis shows that the stress ratio between numerical and experimental tests starts at around 1,35 and slowly converges to around 1,17. For the assessment of such ratio, two of the tests with more data were chosen, one with relatively lower values of stress and the other with higher ones, to provide an interval of the ratio. The slight oscillation of the ratio is caused by differences of scale in the x-axis of the numerical and experimental results and do not represent the actual stress distribution

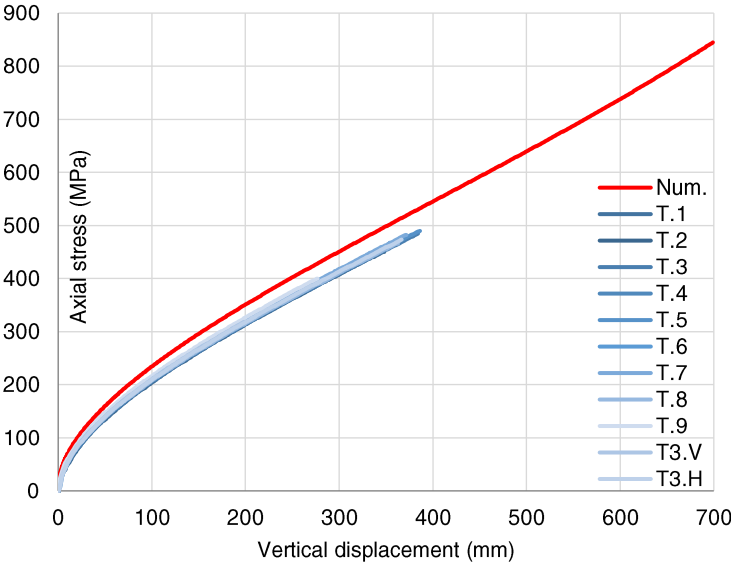


Figure 90 – Stress at centre of outer surface vs. vertical displacement, comparison with experimental values

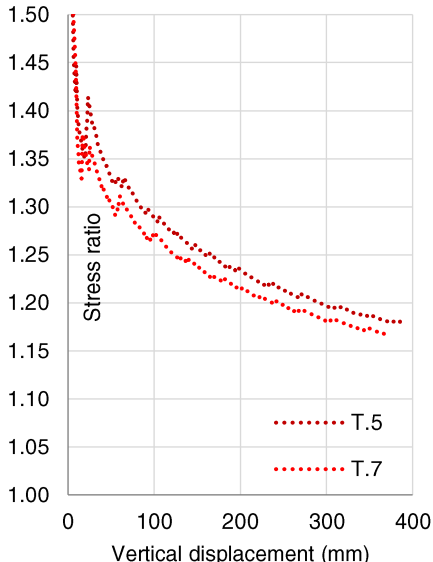


Figure 91 – Ratio of numerical and experimental values

The offset visible in the stress values corroborates the difference already observed in the force graph (Figure 89) and can be explained by the slit of the roller allowing some movements of the plate. The force required to trigger the buckling lowers which, force-wise corresponds to an increase of the effective length of buckling. Furthermore, the out-of-plane deformation is limited by the actual length and even diminished by the plate not being clamped, thus lowering the stresses at the surface. The movements inside the slit, its consequences and a possible way to prevent them, is geometrically investigated in detail later (5.3.7).

Regarding the vertical stress profile, Figure 92 displays both numerical and experimental stress values for the centre stress (A) and the strain gauges distanced 100 mm (B) and 200 mm (C) from the centre. It also presents a stress ratio for each type of analysis between the centre stress (A) and the remaining. Consequently, the relative values “A’ Num.” and “A” are always 1,00.

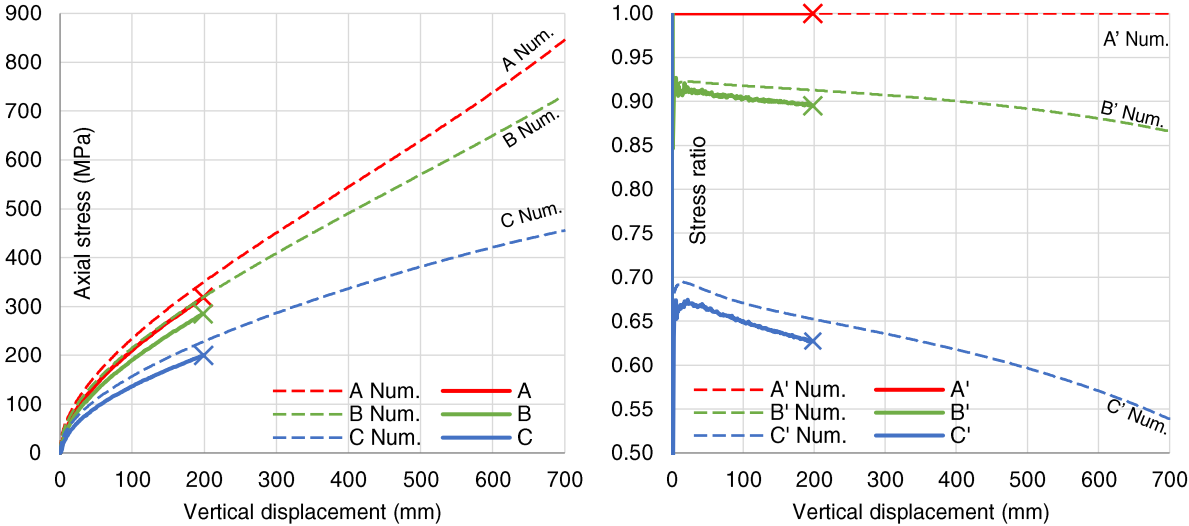


Figure 92 – Numerical and experimental vertical distribution of stress vs. vertical displacement; comparison and ratio (T3.V)

The stress ratio is very similar and almost parallel and is useful to demonstrate the already mentioned hypothesis of different effective lengths in both tests: the 100 mm of spacing does not represent the same relative distance. In fact, there is a small difference between numerical and experimental values, which increases with the distance to the centre. In terms of stress distribution, one can conclude that the experimental sample behaves as if its effective length is lower than the numerical: for the same absolute distance to the centre, the experimental stress ratio is smaller, meaning that the referred absolute distance corresponds to a larger relative distance.

In Figure 93 a similar analysis is performed, but focusing on the horizontal profile of axial stresses. Despite the referred offset, the overall behaviour of experimental and numerical curves is also quite similar. For the width of the section, the ratio is almost identical, even for such a detailed scale as the one presented. This also supports the hypothesis put earlier regarding the influence of the rollers: they influence the effective height of the plate, but do not affect the behaviour of the remaining length of the plates.

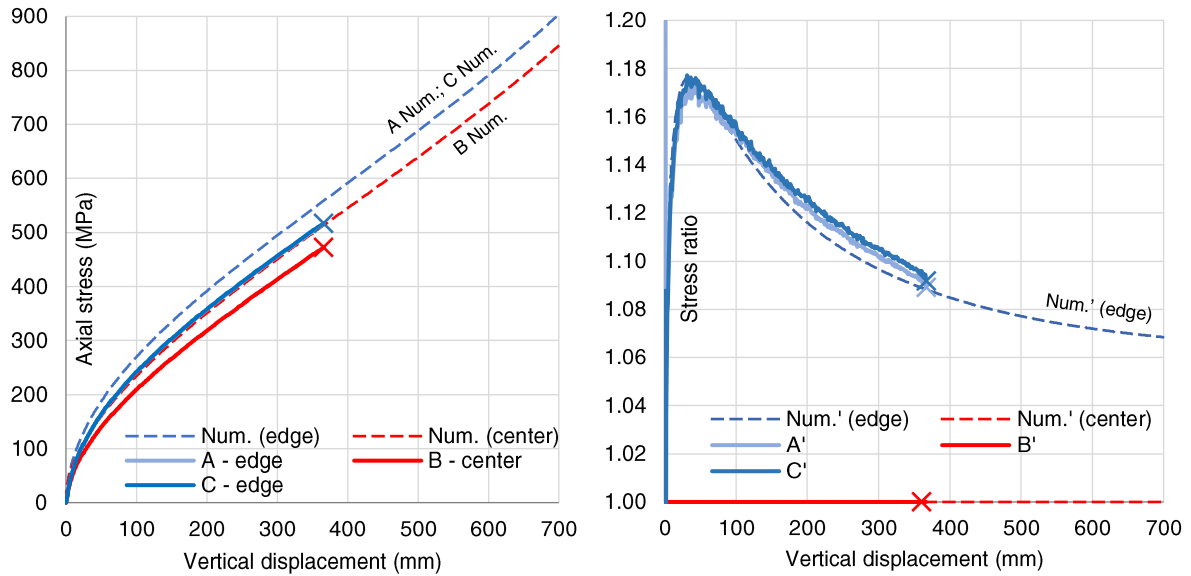


Figure 93 – Numerical and experimental horizontal distribution of axial stress vs. vertical displacement; comparison and ratio (T3.H)

5.3.6. Analytical assessment

The goal of this section is to compare both the experimental and numerical results with an analytical assessment. Results of both analyses are considered and compared to validate the whole test. Dimensions and properties of the section are stated in 3.3.

The flexural buckling of a column starts when the Euler critical load is reached, which can be predicted based on Equation (6). The calculated critical load of 70 N is very close to what was observed experimentally, where all values lay in the interval from 68,4 N to 69,2 N. If an average value of 68,8 N is considered, an effective length of 752,4 mm is obtained.

$$N_{cr,E} = \frac{\pi^2 EI_{11}}{L_{cr}^2}; \frac{\pi^2 * 74\,000 * 53,33}{(746\,mm)^2} = 70,0\,N; \quad (6)$$

$$L_{cr}^2 = \frac{\pi^2 * 74\,00,0 * 53,33}{68,8\,N} = (752,4\,mm)^2$$

The bending moment and the stresses at mid-span can be computed from equations (7) and (8). The influence of the geometrical nonlinearity, responsible for the bending moment, is evident; the vertical force divided by the area is responsible for less than 1 MPa of the axial stress (for $\sigma = 1\,MPa$, $F = 160\,N$).

$$M_{nonlinear} = F_{vertical} \cdot \delta_{out-of-plane} \quad (7)$$

$$\sigma_{max} = \frac{F_{vertical}}{A} + \frac{M_{nonlinear}}{W} \quad (8)$$

If both equations are combined, the stress as a function of the applied force and out-of-plane deformation is given by equation (9). The out-of-plane deformation is then given by equation (10).

$$\sigma_{max}(F_{vertical}, \delta_{out-of-plane}) = F_{vertical} \cdot \left(\frac{1}{160,00} + \frac{\delta_{out-of-plane}}{53,33} \right) \quad (9)$$

$$\delta_{out-of-plane}(F_{vertical}, \sigma_{max}) = 53,33 \cdot \left(\frac{\sigma_{max}}{F_{vertical}} + \frac{1}{160,00} \right) \quad (10)$$

Therefore, equation (10) was applied to the experimental results: for increasing vertical deformation, the corresponding measurements of axial stress and vertical force were considered. Analytical results are plotted together with numerical and experimental results in Figure 94. It can be seen that the analytical out-of-plane deformations are initially slightly lower than the numerical ones, but at around 250 mm of vertical displacement they become very slightly higher. The experimental results are in close agreement with the numerical (and analytical) values; as expected, due to the influence of the slits, the experimental out-of-plane deformations are slightly lower than the numerical ones.

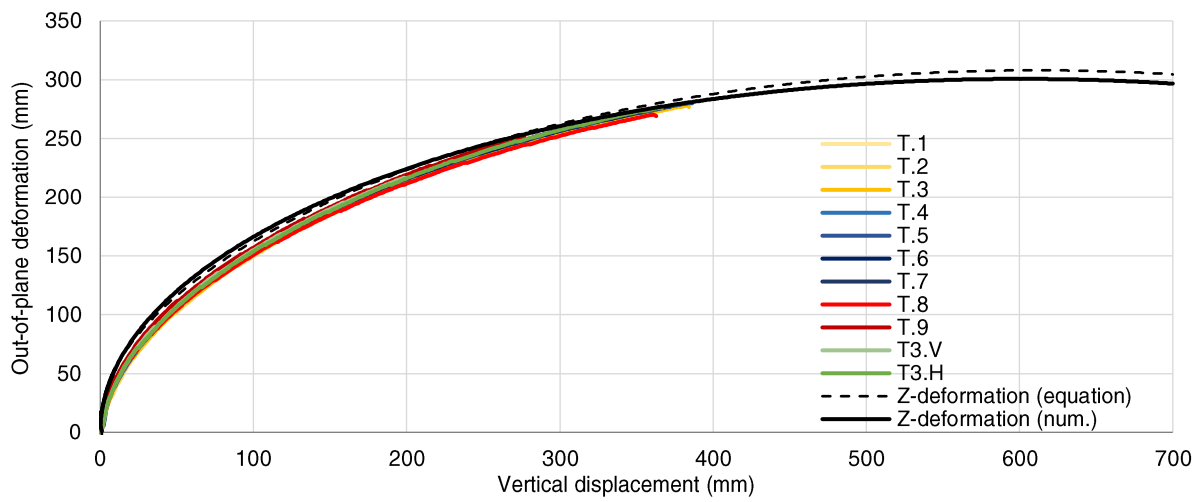


Figure 94 – Out-of-plane deformation as a function of the vertical displacement, comparison of numerical results and calculated results from experimental values

5.3.7. Proposed setup

The slit of the roller that was described before did not reach the centre of the roller and the plate was not clamped. These two factors limited the performance of the buckling test. Figure 95 depicts a geometrical analysis concerned with the geometry of the slits. The figure was created on AutoCAD with the dimensions of the setup to study the geometry of the clamps. It assumes that the curvature of the glass near the rollers is not significant when considering a length similar to the depth of the slit (7 mm). The grey line shows the axis of the plate, also assuming no deformations. Regardless the experimental tests, the figure illustrates some of the problems involved with the geometry of the slit, namely:

- First, the glass-metal contact is located on very thin lines – neither glass nor metal are able to redistribute the stresses created at the contact lines, perhaps even punctually in some prominences of the metal.
- Second, the centre of the roller is not aligned with the axis of the plate – if the curvature of the plate is considered it would further increase this distance. As it no longer behaves as a clamped connection, the out-of-plane deformation is reduced as the plate finds a way to display a less stressed configuration. It also makes the plate more unstable to applied vertical loads; thus, an outcome similar to having a bigger effective buckling length.

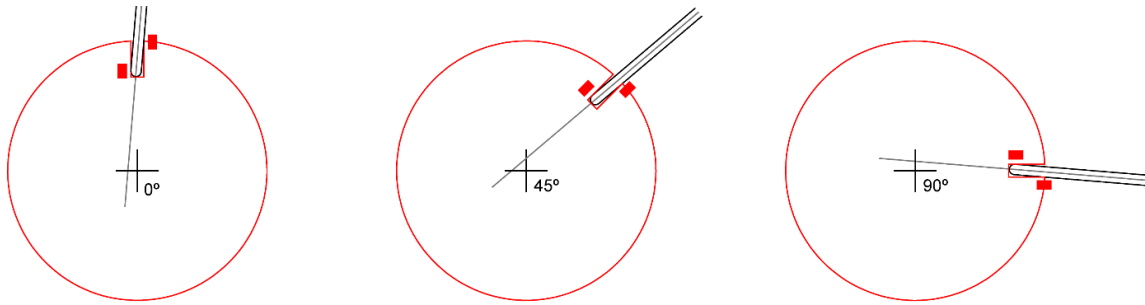


Figure 95 – Contact areas (red) between glass and metallic roller for different rotation angles

Aiming at correcting the above mentioned problems, an alternative version of the clamp was designed by introducing a broader slit. The extra width proposed, besides easing the execution of a deeper slit reaching the centre of the cylinder, allows the introduction of a neoprene band to avoid direct contact between glass and metal and hence preventing stress concentrations.

Figure 96 illustrates the proposed setup and the insertion of the referred neoprene band, which provide the following potential advantages: (i) the lower elastic modulus provides a much better (more uniform) stress distribution; (ii) the applied loads are rather low and the area of contact between glass and neoprene is able to lower the stresses in the neoprene band, so no significant deformations are expected; (iii) the behaviour is close to clamped, depending on the elastic modulus of the neoprene, but allows removing the glass shatters after the collapse¹⁰; (iv) the centre of the roller is coincident with the end of the glass plate, making the height of the setup the same as the height of the plate; (v) finally, it has the advantage of increasing the range of thicknesses possible to test, being enough to couple the glass thickness with an appropriate thickness of the neoprene band.

The proposed geometry also has advantages in terms of standardization as having the end of the glass at the centre of the rollers allows to replicate the setup with similar rollers' radii; the only reasons that led to using a 7 mm slit in a roller with a radius of 25 mm were technical limitations. Furthermore, the width of the rollers should be fit to test specimens with dimensions as specified in EN 1288-3 (1100 x 360 mm). As such, that width should be larger than 360 mm.

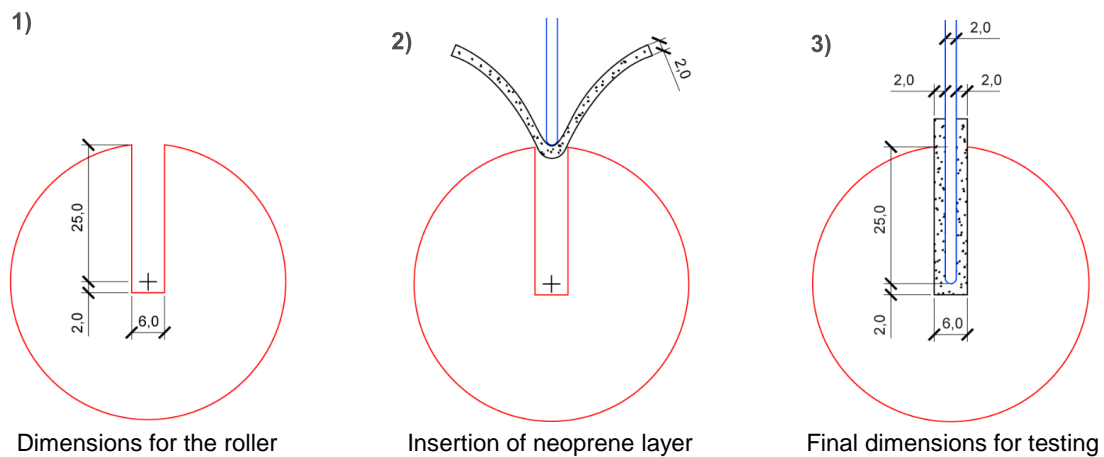


Figure 96 – Side view of the proposed roller with detail of insertion of neoprene band

¹⁰ As opposed to the first version of the setup, which also had a clamped connection and shatters were very hard to remove from the slit (see 5.3.3)

The proposed geometry seems to offer many benefits over the former setup, mainly leading to a design compliant with standard sizes and providing a much closer agreement with the theoretical behaviour expected for well-defined boundary conditions. To conclude, the proposed design is an upgraded version of the one that was used in the tests and could stand as a standard test.

5.4. Proposal of a new test to assess the strength of thin glass: tension test

5.4.1. Motivation

The two tests setups developed and presented in the previous sections provided interesting insights on the behaviour of thin glass and on the procedures to test it. However, both tests presented problems regarding their application or standardization.

The four-point bending test is a rather complex test to perform correctly due to the high forces at stake and the very thin section that quickly becomes unstable, even with lateral constraints.

The buckling test was helpful to understand the buckling behaviour, the forces involved, the distribution of stresses and the influence of a slit wider than the glass, all of which can be useful for future studies on connections and possible applications. The test was fairly easy to set as the geometrical nonlinearities are easily predictable and are even used as part of the test principle, leading to very consistent test results. Although the test may have been compromised by the contact of the glass with the metal along a very thin line, the proposed version of the clamp (which was not possible to test) would prevent that from happening and would lead to a performance much closer to what was predicted in the numerical analysis. However, the setup is closely related to the minimum curvature radius of the glass plate, which depends on its thickness and the ultimate strength of glass. Hence, very thin plates or the ever-growing strength of glass highly difficult the experimental determination of the ultimate strength and might compromise the applicability of this test.

Therefore, an alternative testing method, the tension test, was designed and is presented in the next subsection. The goal of this test setup is to be able to be applied to any thickness and strength, and become the standard for the testing of thin glass. However, due to time limitations, it was not possible to assess this test, so no experimental results can be shown.

5.4.2. Objectives of the new proposed test

The main goal of the tension test is to study the behaviour of glass under pure tension and to determine its ultimate strength. It is important to understand whether the strength is uniform over the whole plate or if there are flaws that can compromise it. Finally, this investigation was complemented with the study of the load transfer from glass to another element, specifically through the use of glued connections.

The main particularity of this test is that it is not prone to any kind of instability and nonlinearity. It can be applied to any thickness that it will provide the result of the ultimate strength.

This test has the advantage of subjecting almost all the length of the plate to the maximum stress. It is also a fairly easy test, without a complex setup and whose results are simple to understand, calculate and even extrapolate to a realistic application. In fact, it does not require any instrumentation besides

the test machine, as the applied force divided by the area equals the stress on the plate. Additionally, the deformations could be used to verify the stresses with the Hooke's Law by employing either a strain gauge or an image-based equipment to measure deformation of the glass.

The difficulties lie in this specimen being a uniform rectangle with the same section along the whole length; usually, specimens used for tensile tests have a dog-bone shape (with a thicker and broader part), so that even though it transfers the force to the machine and stress concentrations may develop, this does not occur at the critical section. However, that is not possible in the glass samples. Therefore, a glued connection is proposed, which also has some difficulties: it is important to avoid stress concentrations or the failure of the glue, which under the extremely high loads required might be a challenge. It is very likely that the collapse starts either at the transition from the glued zone to the free zone or in the glued zone itself, as all the stress concentrations happen in this area. Such problems might be overcome if using a glue with low elastic modulus, a relatively low yielding tension and presents a high elongation at failure that allows the distribution of stresses.

5.4.3. Description of the test method

The setup consists of two pairs of metallic plates that are glued with a proper adhesive to both sides of the glass plate, a pair for each extremity of the plate. The metallic plates assure the connection of the glass specimen to the tensile machine; this connection is done through a steel cylinder inserted in a hole of the same radius in the metallic plates (Figure 97).

This setup requires metallic plates, which are designed to allow for a tolerance of 10 mm expanding from each side of the glass plate, with a total width of 100 mm. This tolerance is optional, but allows for a better connection near the edges of the glass plate. As removing the shatters and glue from its surface may not be an easy process (it may require heat), the plates have to be stiff enough to be separated from the glass without altering its form. Furthermore, tools or chemicals for scraping the glue residues are required. To speed the process of testing, more than a pair of plates should be available.

The machine used should have a tensile force higher than the 100 kN that the *Zwick 100* can apply, as it is not assured that the maximum load of the former causes the breakage of the Leoflex plates: for the cross-section geometry of plates tested, the maximum stress caused by this machine is 625 MPa, which is below the 800 MPa stated by the glass manufacturer (AGC). To reach that stress, it is required a force of 128 kN (see next section for a deeper study on the applied force).

To design the setup for the ultimate strength of the glass, a 1,50 safety coefficient over the value stated by most manufacturers to date (see 2.5) is considered. Therefore, the setup should be able to withstand 1200 MPa in the plate, or 192 kN.

First of all, concerning the metallic setup, as steel has a yield stress of 400 MPa, it would be enough that the two plates were 1,5 mm thick each. However, it is proposed that they have 15 mm each to ease the transfer of the loads to the cylinder and to avoid deformations by being subjected to a much lower stress. While stresses are spread near the glass, there is an accumulation near the cylinder as it transfers all the force. In fact, a quick and simplified calculation shows that if the cylinder has a diameter

of 30 mm and two sides with a width of 15 mm, totalizes a projected area of 900 mm² and resists to a maximum applied force of 360 kN.

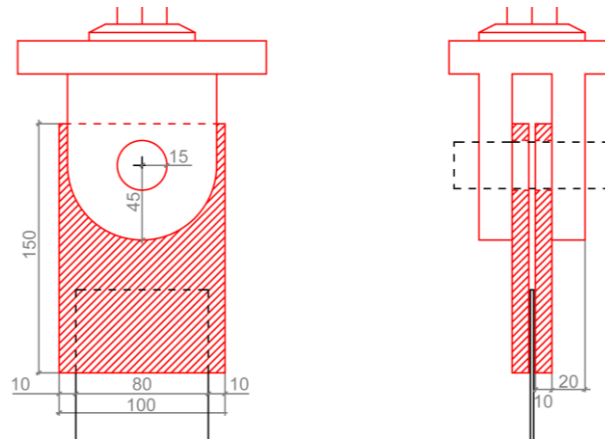


Figure 97 – Tension test setup, front and side view

In terms of gluing, a search on adhesives for glass and metal revealed some options. It was chosen an appropriate one as an example, the “Ultra Light-Weld® 431 High-Temperature and Moisture-Resistant Glass-to-Metal Bonding Adhesive” produced by DYMAX®. The relevant characteristics for this product for this analysis, after curing, are the modulus of elasticity, $E = 573 \text{ MPa}$, the “tensile compression shear glass-to-stainless steel”, $\tau = 23 \text{ MPa}$, and an elongation at break of 61%. Other steel-glass adhesives were studied by Nhamoinesu & Overend (2012), but none had such a high strength. Analytically, to be able to resist to a force of 192 kN and assuming a uniform distribution of stresses (although in glued connections there are concentrations of stress near the edges), it is required that each bonded surface of the glass has an area of 4173 mm², which translates to the 80 mm of width and 53 mm in length (hence, a lower bound).

5.4.4. Numerical assessment of the test

The numerical test had the main goal of predicting the behaviour of the glued connection and the distribution of stresses. An example of the test is modelled and post-processed in midas FEA 2016, following the ideas described in the former section.

The finite elements used were solid elements to retrieve data on variations of stresses along the three dimensions. Another option would be the use of plain strain elements, modelling the lateral section of the glass. This model assumes an infinite width for the cross section and is far lighter and faster to process numerically; however, a more complete approach was preferred to start with and eventually calibrate the simpler version. The mesh was composed by cubes of 1,00 mm³ - the sensitivity study showed it was the best solution between a very heavy model and an excessively coarse mesh.

The geometry of the model is a simplification based on the horizontal symmetry of the setup with the plane of symmetry at mid-span. Therefore, the model consists of a glass plate with dimensions of 355x80x2 mm³ and two glue plates at each of its sides, with 60x80x2 mm³. This simplification reduces the number of elements to half, lightening the model considerably.

The glass was modelled as a linear material with elastic and shear moduli of 74 GPa and 30 GPa respectively. The glue was modelled as a nonlinear elasto-plastic material with a von Mises yield tension

of 23 MPa and an elastic modulus of 574 MPa, as indicated in the product data sheet (DYMAX, available in the appendix E.1). Neither the Poisson ratio nor the shear modulus were indicated, but the study by Nhamoinesu & Overend (2012) on similar glass-steel adhesives revealed a range of values for the Poisson's ratio from 0,29 to 0,48. Therefore, these two Poisson's ratios are used to study its impact on the behaviour of the test and cover the whole interval of options.

No information on the optimal thickness of glue was found on the product data sheet, just an indication of the time of cure versus the depth of the glue with a range until 7 mm. In the literature concerning steel-glass adhesives, two relevant articles (Nhamoinesu & Overend, 2012; Nhamoinesu, *et al.*, 2014) base all of their tests on 3,00 mm thick samples; on the other hand, Cruz *et al.* (2014) carried out the tests in samples of 0,30 mm. The thickness of the glue was set at 2,00 mm, making it possible to understand the development of deformation and stresses through its thickness using the 1,00 mm cubes as solid finite elements – further analyses on the thickness of the glue are required, both in terms of optimal thickness, as well as the effect it has on the distribution of stresses in this tension test.

Regarding the boundary conditions, depicted in Figure 98, all the nodes of the bottom surface were restrained in the z-direction; one edge was restrained in the x-direction and another one in the y-direction. The analysis performed was nonlinear so, in terms of loads, a displacement of 5 mm was applied to all the nodes of the outer surface of both glue panels in 25 load steps of 0,20 mm.

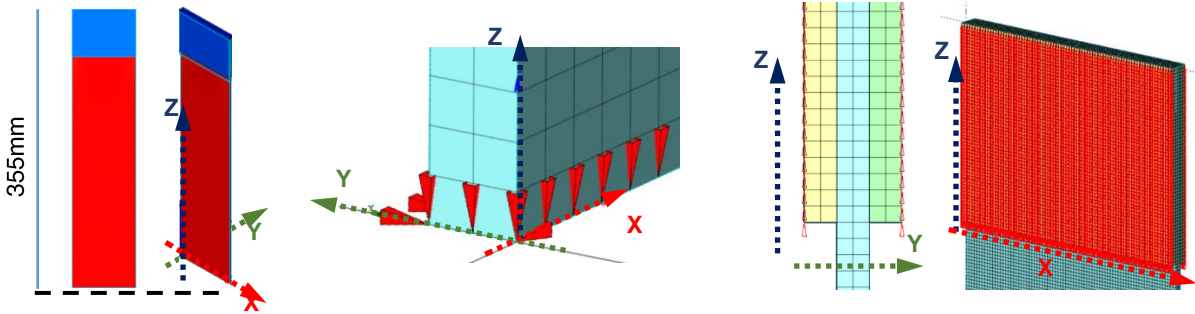


Figure 98 – Overall model, boundary conditions (bottom surface) and displacement loads (side view and perspective)

In terms of results, the overall behaviour of the test is illustrated in Figure 99. It depicts a deformed configuration at true scale with the development of the principal stresses in a qualitative way, focused on the smoothness of the development of the stresses, which will be quantified in later analyses. Some points are worth noting, such as the increase of the stressed length as the displacement increases and the significant intensification of the glue deformation from 3 mm to 4 mm and even more from 4 mm to 5 mm. Regarding the front view, it is fairly homogeneous with slightly higher values towards the centre.

In the analysis of the force applied vs. the displacement at the outer surface of the glue (Figure 100), it is evident that: (i) as expected, the Poisson's ratio is not relevant for the applied force vs. displacement and (ii) the adhesive yields at 127 kN. Assuming a uniform distribution of stresses, if the applied force is divided by the section area of the glass plate, the average stress is 793,8 MPa; if divided by the total surface area of the glued connection, the average is 13,2 MPa. However, the stress distribution is not uniform and was also investigated. From Figure 100, six points are highlighted and presented in more detail in Table 11 as they are used to illustrate the analyses of the stress distribution later in this section. Note that the last point (6) is in a yielding phase, so all phases are covered in the stress analyses.

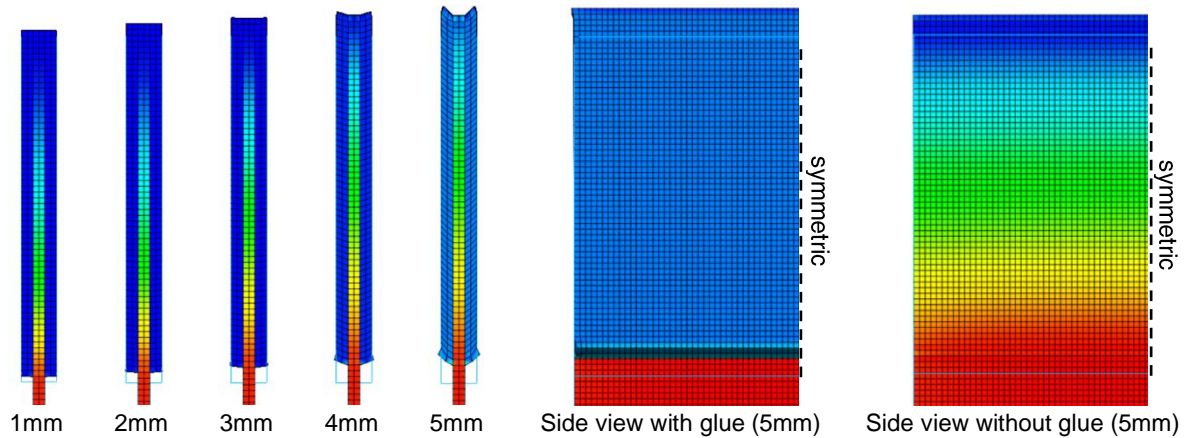


Figure 99 – Deformation of the glue and development of the principal stresses vs. vertical displacement: side and front view ($\nu = 0,29$)

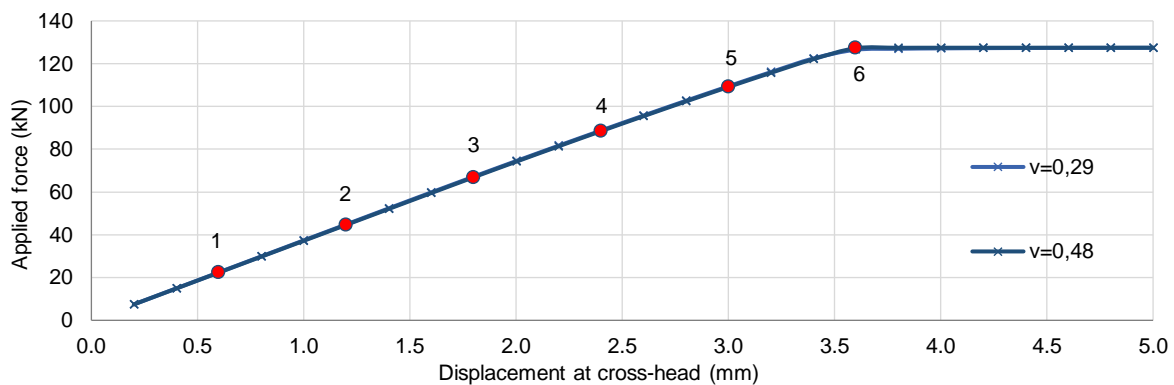


Figure 100 – Applied force vs. vertical displacement at the outer surface of the glue (half of cross-head displacement)

Table 11 – Ultimate values of displacement, force, strain and stress for each test

Number	Displacement (mm)	Applied force (kN) ($\nu = 0,29$)	Applied force (kN) ($\nu = 0,48$)
1	0,6	22,43	22,31
2	1,2	44,86	44,63
3	1,8	67,17	66,88
4	2,4	88,74	88,45
5	3,0	109,44	109,11
6	3,6	(yielding) 126,52	(yielding) 127,25
-	5,0	(yielded) 127,43	(yielded) 127,47

The analysis of the stresses developed in the glass surface was carried out by plotting the values of the principal stress σ_1 on the centre (C) and on the edge (E) for the six points presented in Table 11 over a profile of 80 mm starting from the top of the glass plate and for a Poisson's ratio of 0,29 (Figure 101) and 0,48 (Figure 102). The stresses reach the 800 MPa and are quite homogeneous, without relevant spikes. The glued area has 60 mm of length and the transition introduces a small perturbation in the stress that is more pronounced for the higher value of Poisson's ratio. The centre stresses are higher near the transition and lower near the top of the plate; the length where centre stresses are predominant is progressively larger as the loads increase and for higher values of Poisson's ratio.

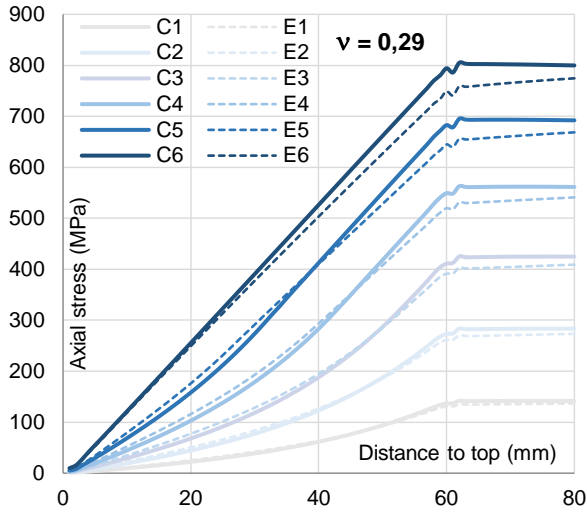


Figure 101 – Evolution of centre (C) and edge (E) axial stresses in the glass, vertical profile ($\nu = 0,29$)

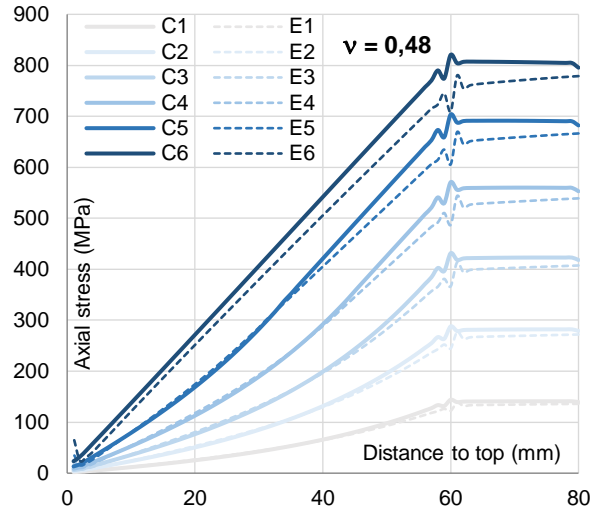


Figure 102 – Evolution of centre (C) and edge (E) axial stresses in the glass, vertical profile ($\nu = 0,48$)

A similar analysis was carried out about the surface shear stress profile over the glued length (60 mm). For the six different load/displacement values listed in Table 11, the shear stresses at the centre and at the edge along the glued length were computed for $\nu = 0,29$ (Figure 103) and $\nu = 0,48$ (Figure 104).

It can be seen that there is no significant difference between the shear stresses obtained for the two different values of the Poisson's ratio, except for some details. The yielding occurred for stresses of 13,3 MPa, which is in agreement with the von Mises yield parameter and demonstrated in equation (11).

$$\sigma_y = \sqrt{3} \sigma_{shear}; \sigma_{shear} = \frac{23}{\sqrt{3}} = 13,3 \text{ MPa} \quad (11)$$

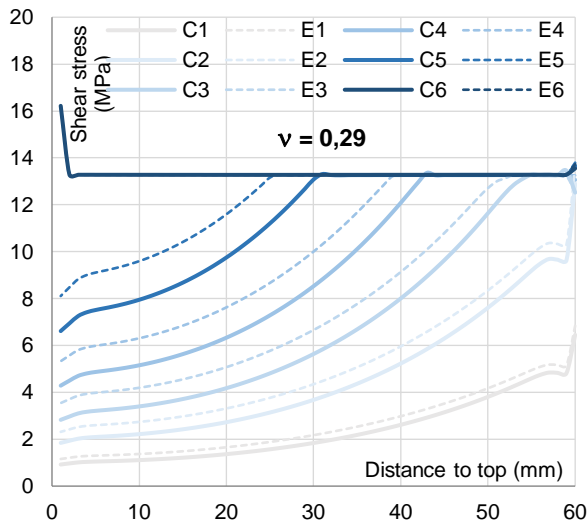


Figure 103 – Evolution of centre (C) and edge (E) shear stresses in the glue, vertical profile ($\nu = 0,29$)

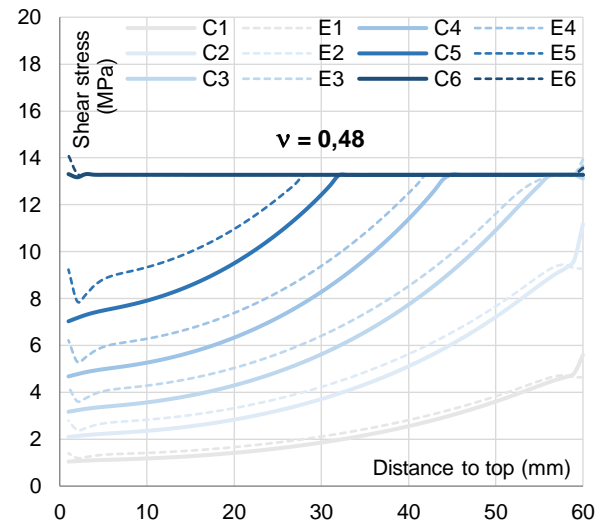


Figure 104 – Evolution of centre (C) and edge (E) shear stresses in the glue, vertical profile ($\nu = 0,48$)

A complementary but insightful analysis is available in the Appendix E.2, where instead of presenting the shear stresses, two similar graphs plot the principal stresses σ_1 . In this case, the stress distribution is considerably different for the two values of the Poisson's ratio, particularly regarding the stress ratio from the centre to the edge. Also, a detailed illustration of the deformation and of the stress concentration at

some particular nodes is shown. Hence, the Poisson's ratio has no relevant impact on the axial stresses on the glass nor on the shear stresses on the glue; however, it has considerable influence on the principal stresses on the glue and the homogeneity of the stress distribution: for a Poisson's ratio of the adhesive closer to that of glass (i.e., the adhesive with Poisson's ratio of 0,29) a better response is obtained.

5.4.5. Summary

The tension test was proposed to solve the shortcomings of the previous destructive tests in determining the tensile strength of thin glass. The objectives are to study the glass under pure tension and to determine its ultimate strength; secondarily, to study the load transfer from glass to another element. The setup is simple and does not require any other instrumentation than the record of the force applied by the traction machine. The numerical analysis corroborated the viability of the test.

5.5. Concluding remarks

In this chapter, two destructive tests to determine the tensile strength of thin glass were assessed: the in-plane four-point bending test and the buckling test. Then, based on the results obtained, an alternative test was proposed, the tension test.

For the in-plane four-point bending test, the objectives and the basic test setup were first presented; next, due to the successive difficulties encountered in testing thin glass, an overview of the several iterations between setup modifications was presented, as well as the results of preliminary tests; finally, a numerical analysis of this test was presented, which focused mostly on the lateral torsional buckling of the glass pane being tested.

For the buckling test, the objectives and the test setup were initially presented; then, the preparation of the tests and the results of the experiments were presented. Subsequently, the numerical analysis conducted to simulate the tests was presented. Finally, a modified setup was proposed, addressing the weak points of the test setup used.

The final part of the chapter presented a proposal of an alternative test, the tension test. The motivation was the discussion of the two destructive tests performed and of their potential and limitations in determining the tensile strength of thin glass. The objectives and the setup of this test were described and its potential was confirmed based on a numerical analysis.

6. Conclusions and future developments

6.1. Conclusions

This section presents the main findings of this study, including those from the non-destructive and destructive tests and concludes with an overall reflection on the application of thin glass to building and construction. The next section proposes a series of future developments in this topic.

Starting with the non-destructive tests, specifically the **tin side detector test**, the results obtained were inconclusive and indicate that the test as performed is not appropriate for chemically tempered thin glass. The factors that might have thwarted the readings were (i) the reduced thickness, which may not be enough to block the UV light and still cause some fluorescence in the tin of the opposite side, and (ii) the chemical temper, as it may reduce the tin concentration on the surface. Testing either a thicker sample of chemically tempered glass or a float thin glass would provide further insights on the influence of each parameter, but none of these materials were available. In conclusion, although a more advanced detector with digital capabilities could possibly provide a deeper insight of the differences of tin concentration at the surface, with the model employed that was impossible to discern with the naked eye.

Regarding the **SCALP test**, for the Leoflex glass, a significant offset was found between the magnitudes of the values provided by the producers to the ultimate stress (from 600 MPa to 800 MPa, see appendix A), those obtained from the mechanical tests (around 450 MPa to 500 MPa¹¹, see 5.3.4) and the results of the SCALP test (200 MPa). Although those values cannot be directly compared (according to equation (2), the actual strength of glass can be estimated based on the surface stress and the strength of annealed glass), it is clear that the method failed to provide the real value of the surface stress. It also did not detect any difference between the two sides of the plate, rendering the study of the influence of the tin in the surface stress inconclusive. Sometimes, the fitting of the optical retardation to the actual results, which is then inverted to calculate stresses, was far from perfect, mostly at the surface, leading to inaccurate results. Besides the inversion method¹² and the characteristics of the specimen itself, the cleaning of the surface and the correct immersion of the polariscope prism can have significant influence in the results, hindering the readings at the surface. Comparing to Hödemann *et al.*, (2016), whose SCALP results are around 1 000 MPa, the major differences are the depth of the layer achieved in the chemical tempering and the inversion method used, besides slight modifications to the polariscope itself.

About the depth of the layer (DOL), it was verified that it has a strong negative correlation with the surface stress. In the Appendix A, such a relationship is suggested in the graph of DOL and compressive stress (Figure A-2). It is also clear that the DOL is a very important parameter for good readings and the magnitudes commonly used in commercial glasses seem too superficial for the current SCALP model. Still, the values attained are in accordance to what is prescribed by the producers:

- AGC Leoflex: 50-70 μm (experimental value), 35-80 μm (technical specifications, *cf.* A.1);
- SCHOTT Xensation: 110 μm (experimental value), >50 μm (technical specifications, *cf.* A.2);
- Hödemann, 2016: 365 μm (the glass thickness was 15 mm) (Hödemann *et al.*, 2016).

¹¹ Strength values are a lower bound as there might have been an upper limit imposed by the setup of the test.

¹² As mentioned in 4.3.2, the inversion process turns the optical retardation registered into the stress profile.

About the destructive tests, the **four-point in-plane bending test** required a significant development of the setup, including several iterations, which focused mainly on increasing the stiffness of the lateral constraint. Many preliminary tests on aluminium plates revealed considerable proneness to buckling and were used to adjust the setup for testing glass samples. Another factor that played a role and is hard to standardize is the compression that the lateral constraints apply in the glass, offering resistance to the free vertical deformation of the glass specimen.

The only preliminary test performed on a glass plate was compromised by a flaw at the edge of that specific specimen, but the pre-collapse behaviour was also far from expected: the compressibility of the rubber bands under the supports remarkably influenced the force vs. displacement behaviour, which can also have been influenced by the (lateral) compression and consequent drag of the lateral constraints; in addition, the load head was fixed, thus introducing unbalanced loads. No experimental results were retrieved from this test. However, a cylindrical loading head was designed and built. Consequently, a final version of the setup was proposed and is fully ready for further testing, should an investigation focused on the edge be developed in the future.

To retrieve correct data, the use of additional strain gauges or LVDTs could be useful. Placing a strain gauge under the bottom edge of the glass plate and one at the top would help to provide the value of the maximum stress and understand the (possible) interference of rubber bands. Although it should be visible in the force vs. displacement graph, placing other strain gauges in the referred critical spots of the top edge (see 5.2.3), such as at mid-span between supports and near the supports would help to understand if buckling happened. Introducing a set of LVDTs would provide the deformation of the neoprene bands, allowing to discount it from the deformation of the glass panel only: one LVDT measuring the mid-span deformation and two over both extremity supports would be enough.

The numerical study showed that buckling causes an increase of stresses on the top edge of the glass plate. The analyses performed did not account for the influence of the continuous lateral constraint, which, in the experiments, had a higher stiffness near the supports. So, even though the numerical maximum stress occurs near the supports, it is likely that the mid-span is the critical point. At a more general level, the analyses showed that the setup is prone to buckling, which, once occurs, deeply affects the stress distribution and originates wide range of stress values.

Concerning the **buckling test**, the setup used allows for very significant deformations and the test principle is based on the geometrical nonlinearities, which are not a problem as in the four-point bending test. Regarding the experimental tests performed, the behaviour and results were very consistent. Concerning the maximum stress, the average value measured at the centre of the 10 samples is 445 MPa; it should be noted that the actual strength values are expected to be higher. These results provided 5% probabilistic values of $f_{k,Normal} = 362$ MPa for a normal distribution, and $f_{k,Weibull} = 325$ MPa for the 2-parameter Weibull distribution. In terms of stress distribution, the maximum stress developed at the edges of the plate at the mid-height section; when the sample collapsed, the stress at the edge (at mid-height) was 1,09 times higher than at the centre. If this factor is taken into account, the ultimate stress at breakage has an average value of 485 MPa and a characteristic value of 394 MPa or 514 MPa, for the normal and 2-parameter Weibull distributions, respectively. It is also worth mentioning that the maximum stress attained with this

test was 490 MPa (at the center), which would translate into around 534 MPa at the edges (considering the coefficient of 1,09). In this test the shatters of the collapsed glass plates were very small, almost powder-like.

The experimental responses measured in these tests were in good agreement with the numerical and analytical predictions. In terms of force, the Euler (analytical) critical load was 70 N, and in the tests the instability started at around the same applied force, around 68 N; however, the triggering of buckling in the experiments involved a relatively sudden change of behaviour, whereas in the numerical simulation the change in the load vs. displacement response was much smoother. From then on, the numerical and experimental load vs. displacement curves became parallel, differing by only around 5,5 N to 6,5 N for the different tests. Regarding the stress response, the numerical simulation retrieved a similar overall behaviour to that measured in the experiments, although it provided higher stress values – the ratio between predicted-to-measured stresses was initially 1,40 and it progressively decreased to 1,15. This ratio was also observed in the vertical and horizontal stress profiles measured in two of the specimens.

In spite of the above-mentioned success, the plate was not fully clamped in the rollers' slits and this had some influence in the experimental behaviour, which justifies the differences to the numerical results. This factor (i) makes the plate more unstable and start buckling at a lower load; (ii) causes the out-of-plane deformation to reduce as the plate finds a way to display a less stressed configuration, therefore lowering the stresses for the same applied load and (iii) the transition from glass to metal done by the slit, which was neglected, causes the stress distribution to behave as if the lengths of the numerical and experimental tests were different.

Moreover, and more importantly, the collapse seems to have been caused by the contact of the glass plate with the rollers, as attested by video frames and by a geometrical analysis of the supports area. The glass/metal contact is located on very thin lines and there is not any material to prevent the stresses concentrations that are developed. It seems that the unstable configuration of the glass plates in the slits was the critical point and most likely limited the maximum stress attained in the tests.

A corrected version of this setup was proposed as the standard for the buckling test. This version has two main differences from the one that was actually tested: a neoprene band is used inside the slits to better distribute the stresses between glass and metal, preventing or at least considerably limiting any stress concentrations; the slit is deeper and wider, which not only makes it easier to execute, but also allows the plates to reach the centre of the roller and also the insertion of the neoprene band. This setup allows for wider specimens and different glass thicknesses if paired with the correct thicknesses of the neoprene bands. Presumably, the behaviour of such experiments will follow closer the numerical analysis. It is also much easier to replicate with rollers of different radii.

To finish the research program, an alternative test is proposed, the **tension test**, which seems to be the one with the most potential in terms of application and standardization, provided that the issues concerned with the glued connection are dealt with correctly. The numerical study revealed that the nonlinearity and long elongation of the adhesive used to bond the glass plate to the metallic plates provides a very homogeneous load transfer from the glass being tested to the outer surface of the metallic plate of the test fixture. There are some important points regarding the behaviour of the adhesive

in the numerical tests: with a von Mises yielding stress of 23 MPa and a bonded length of 60 mm, values of stress in glass reached 800 MPa, which are quite in line with the values aimed at, without any significant stress concentration; the Poisson's ratio of the adhesive is not a key factor, although values closer to that of glass are recommended for their homogeneous stress distribution. The main advantages of this test over the former two are the following: (i) the thickness or strength of the thin glass samples cannot compromise the collapse as the curvature radius is not involved; (ii) the portion of the glass area subjected to the maximum stress compared with the total area is much higher; (iii) the test is dominated by a geometrically linear behaviour; and (iv) the yielding of the adhesive allows for a quite homogeneous load transfer, and although it introduces some nonlinearity in the force-displacement response, the stress develops linearly in most of the glass area.

To conclude, the **potential of the thin glass for construction** was confirmed. In fact, several of its properties were evident in the aforementioned tests: thin glass has a significantly higher strength value than those of other types of glass, it is flexible and light-weight. Structural uses of thin glass can be bolder than current uses, namely in curved panels, under tension applications or longer spans. Still, prior to using thin glass as a structural material, several lines of research should be investigated and are addressed in the next section.

6.2. Future Developments

This section describes in more detail the research required related to testing methods, but also introduces some broader topics in the field of thin glass that are worth being further developed. Therefore, the section is divided in: (i) non-destructive tests, (ii) destructive tests, and (iii) thin glass structural behaviour.

i. Non-destructive tests

Non-destructive tests have the great advantage of keeping the sample intact. If confirmed to be a valid method to determine the strength of thin glass, they could replace destructive tests. In that case, in the limit, the quality and strength of all plates could be examined at virtually no cost.

The **tin side detector test** does not fulfil the above mentioned requirements as it does not provide the value of the strength and is limited to samples produced with only one process (float). However, a conclusive investigation on the influence of the tin on the strength of thin glass would provide relevant data for design, namely on deciding the material surface that shall be subjected to the maximum tensile stresses. Such tests should, in a first phase, use a more advanced detector, namely with digital capabilities, to verify if there is still tin and, if tin is indeed found, use other methods (destructive or non-destructive) to determine the strength of their tin and air sides by systematically testing similar samples.

On the other hand, the **SCALP test**, and more generically the photoelastic methods, seem to have potential to replace destructive tests in the future as the standard. Yet, in this research it became clear that the SCALP requires a considerable development to better determine the surface stress on chemically tempered thin glasses with reduced DOL. The research and consequent introduction of curved ray inversion instead of the current method (straight ray inversion) can also be a short-term step

forward. To conclude, a testing device with a principle similar to SCALP, the laser sheet scattered light method (Castellini *et al.*, 2012), seems to be the future of non-destructive strength testing for thin glass, but needs to provide valid results of the surface stresses of chemically tempered thin glass.

ii. Destructive tests

Destructive tests are less dependent on technological advancements. However, generically, the adaptation of a standard setup for glass or the use of a new setup require investigations on the distribution of stresses on the tested samples.

This dissertation showed that the **in-plane four-point bending** test is very complex to perform, as it is very difficult to overcome several sources of nonlinearities in the response. If further developed, this setup should use a much stiffer lateral constraint than the one tested in this research; one line of research to explore is the characterization of the edge of the thin glass specimens.

Regarding the **buckling test**, further developments should use the proposed version of the setup. In another topic, a study on the size of the sample, possibly per thickness of thin glass, could serve as a guideline to employ this method in the future. In fact, increasing the height of the sample has two consequences: (i) a lower critical load to cause the buckling, but (ii) a bigger out-of-plane deformation; both affecting the bending moment and the respective stresses. The width of the sample was also concluded to influence the stress distribution. Further developments should incorporate such a study to assess the conditions under which this test is viable.

Finally, the **tension test** proposed in this dissertation has many subjects to develop. As the best option to become a standard test, further developments should progress in that sense: to define the parameters for the adhesive, in terms of thickness and elastic modulus, and to investigate and optimize the metallic parts proposed, confirming experimentally and numerically its viability. Short-term developments should include an experimental test to provide data other than computational models.

iii. Thin glass structural behaviour

In order to apply thin glass in structural applications, several questions need to be answered. Therefore, future studies should investigate the following aspects:

- the most effective connections for both thin glass/thin glass and for thin glass/other materials;
- the behaviour of laminated thin glass members;
- the fatigue behaviour of thin glass and, if laminated, of its interlayer, as adaptive and dynamic applications require good fatigue performance;
- the evolution with time of the compressive stress in chemically tempered thin glass;
- the development and consequences of flaws on the strength of chemically tempered thin glass.

7. Bibliography

- Aben, H., & Guillemet, C. (1993). *Photoelasticity of Glass*. Berlin: Springer-Verlag.
- Aben, H., Anton, J., & Errapart, A. (2008). Modern Photo elasticity for Residual Stress. (B. P. Ltd, Ed.) *Strain* 44, 40-48.
- Aben, H., Anton, J., Errapart, A., Hödemann, S., Kikas, J., Klaassen, H., & Lamp, M. (2010). On non-destructive residual stress measurement in glass panels. *Estonian Journal of Engineering*, 16, 150-156.
- AGC. (2012). *Technical Specifications - Leoflex(TM)*. AGC.
- AGC Electronics America. (n.d.). *Leoflex Brochure - Shaping the Future*. AGC Electronics America.
- Albus, J., & Robanus, S. (2015). Glass in Architecture - Future developments. *Detail*.
- Anderson, T. (2005). *Fracture mechanics: fundamentals and applications*. CRC Press.
- Anton, J., Errapart, A., Paemurru, M., Lohegnies, D., Hödemann, S., & Aben, H. (2012). On the inhomogeneity of residual stresses in tempered glass panels. *Estonian Journal of Engineering*, 18,3-11.
- ASM International (1997). *Materials Selection and Design - ASM Handbook* (Vol. 20). ASM International.
- Blank, K., Durkop, D., Durchholz, M., Gruters, H., Helmich, G., & Senger, W. (1994). Strength tests of flat glass by means of four point bending. *Glastechnische Berichte* 67, 9-15.
- Bos, F. (2009). Failure Behaviour of Glass Beams under Various Loading Conditions; Comparisons of Safety. *Glass Performance Days 2009 Proceedings* (pp. 290-296). Glass Performance Days.
- Bos, F. P. (2009). *Safety Concepts in Structural Glass Engineering - Towards an Integrated Approach*. Delft: TU Delft. PhD thesis in Architecture.
- Bos, F., & Veer, F. (2005). The Laminated Glass Column. *Glass Processing Days 2005*. Tampere, Finland.
- Brill, R. H. (1963). *Ancient Glass*. Scientific American.
- C. R. Laurence Co., Inc. (n.d.). *Tin side detector - MODEL# TS1301*. C. R. Laurence Co., Inc.
- Cartz, L. (1995). *Nondestructive Testing*. USA: ASM International.
- Castellini, P., Stroppa, L., & Paone, N. (2012). Laser sheet scattered light method for industrial measurement of thickness residual stress distribution in flat tempered glass. *Optics and Lasers in Engineering*, 50, 787-795.
- Colombin, L., Jelli, A., Riga, J., Pireaux, J. J., & Verbist, J. (1977). Penetration depth of tin in float glass. *Journal of Non-Crystalline Solids*, 24, 253-258.
- Cook, R. D. (1995). *Finite Element Modelling for Stress Analysis*. United States of America: John Wiley & Sons, Inc.
- Corning. (2015). *First Corning® Gorilla® Glass windshield featured in Ford GT*. Retrieved from Corning: <https://www.corning.com/worldwide/en/innovation/corning-emerging-innovations/gorilla-glass-for-automotive-ford-gt.html>
- Corning. (2016 a). *Corning - How it's Made*. Retrieved from Corning: <http://www.corning.com/>
- Corning. (2016 b). *Corning - The Glass Age*. Retrieved from Corning: <http://www.corning.com/>

- Cruz, P. J., Pardal, R., & Valente, I. B. (2014). Experimental study of structural adhesives for a steel-glass connection. *glasstec*. Düsseldorf, Germany
- De Jong, B. S., Beerkens, R., van Nijnatten, P., & Le Bourhis, E. (2011). *Ullmann's Encyclopedia of Industrial Chemistry - Glass, 1.Fundamentals*. Wiley-VCH Verlag.
- Dean, G., & Crocker, L. (2001). *The Use of Finite Element Methods for Design with Adhesives*. Teddington, Middlesex, United Kingdom: National Physical Laboratory.
- DYMAX. (n.d.). *Ultra Light-Weld 431 - Product Data Sheet*. DYMAX.
- EN 1288:2000 *Glass in building - Determination of the bending strength of glass*. Brussels: European Committee for Standardization (CEN).
- EN 1863-1:2011 *Glass in building. Heat strengthened soda lime silicate glass. Definition and description*. Brussels: European Committee for Standardization (CEN).
- EN 12150-1:2015 *Glass in buildings – Thermally toughened soda lime silicate safety glass*. Brussels: European Committee for Standardization (CEN).
- EN 1748-1: 2012 *Glass in buildings - Special basic products - Borosilicate glasses - Part 1: Definitions and general physical and mechanical properties*. Brussels: European Committee for Standardization (CEN).
- Feldmann, M., & Kasper, R. (2014). *Guidance for European Structural Design of Glass Components*. Luxembourg: European Commission - Joint Research Centre.
- Ford (2015, December). *Ford and Corning introduce industry-first Gorilla Glass hybrid windshield technology on all-new Ford GT supercar*. Retrieved from Ford: <https://media.ford.com/content/fordmedia/fna/us/en/news/2015/12/15/industry-first-gorilla-glass-hybrid-windshield-on-all-new-ford-gt.html>
- GlasStress Ltd. (2013). *SCALP Instruction Manual Ver. 5.8.2*. GlasStress Ltd.
- Griffith, A. A. (1921). *The Phenomenon of Rupture and Flow in Solids*. London: Philosophical Transactions of the Royal Society of London, 221, 163-198.
- Gy, R. (2013). Stress corrosion of silicate glass: a review. *Journal of Non-Crystalline Solids*, 316, 1-11.
- Haldimann, M., Luible, A., & Overende, M. (2008). *Structural Use of Glass*. Zurich: IABSE.
- Hödemann, S., Valdmann, A., Anton, J., & Murata, T. (March 2016). Gradient scattered light method for non-destructive stress profile determination in chemically strengthened glass. *Journal of Materials Science*, 51, 5962-5978
- Holzinger, P. (2011). Thin glass technology for insulating glass production. *Glass Performance Days*. Finland: GPD.
- Hundevad, J. (2014). Thin Glass: Super lightweight glass structures - a study . *GlassConGlobal - Innovation in Glass Technology* (pp. 324-337). Philadelphia: GlassCon.
- Jandl, M. (2015). Quadruple IG-Unit with thin glass membranes. *Glass Performance Days 2015*, (pp. 31-33).
- Jiang, L., Guo, X., Li, X., Li, L., Zhang, G., & Yan, Y. (2012). Different K⁺-Na⁺ inter-diffusion kinetics between the air side and tin side of an ion-exchanged float aluminosilicate glass. *Applied Surface Science*, 265, 889-894.
- Lambert, L. B. (2005). *Bulletin for the History of Chemistry, Vol 30*. Division of History of Chemistry of the American Chemical Society.

- Louter, P. C. (2011). *Fragile yet Ductile: Structural Aspects of Reinforced Glass Beams*. Delft: TU Delft. PhD thesis in Architectural Engineering.
- Maniatis, I., Nehring, G., & Siebert, G. (2014). *Studies on determining the bending strength of thin glass*. ICE Publishing. *Structures and Buildings*, 169, 393-402.
- McGraw-Hill. (2003). stress-optic law. (n.d.). In McGraw-Hill, *McGraw-Hill Dictionary of Scientific & Technical Terms, 6E*. The McGraw-Hill Companies, Inc.
- Mognato, E., Schiavonato, M., Barbieri, A., & Pittoni, M. (2016). Process influences on mechanical strength of chemical strengthened glass. *Challenging Glass 5*. Ghent, Belgium.
- Neugebauer, J. (2016). Determining of Bending Tensile Strength of Thin Glass. *Challenging Glass 5*. Ghent, Belgium.
- Nhamoinesu, S., & Overend, M. (2012). The Mechanical Performance of Adhesives for a Steel-Glass Composite Façade System. *Challenging Glass 3*. TU Delft: Challenging Glass 3.
- Nhamoinesu, S., Overend, M., Silvestru, V., & Englhardt, O. (2014). The mechanical performance of adhesively bonded steel-glass composite panels - Medium-scale tests and numerical models. *Challenging Glass 4* (pp. 269-276). London: Taylor & Francis Group.
- Nijse, R., & Brincke, E. t. (2014). Glass Columns. *Challenging Glass 4* (pp. 625-632). Lausanne: Taylor & Francis Group.
- Oikonomopoulou, F., Veer, F., Nijse, R., & Baardolf, K. (2014). A completely transparent, adhesively bonded soda-lime glass block masonry system. *Journal of Facade Design and Engineering*, 201-221.
- Phillips, C. J. (1941). *Glass: the miracle maker*. New York: Pitman Publishing Corporation.
- Rasmussen, S. C. (2012). *How Glass Changed the World - The History and Chemistry of Glass from Antiquity to the 13th Century*.
- Raymond, R. (1986). *Out of the fiery furnace. the impact of metals on the history of mankind*. The Pennsylvania State University Press.
- Rogers, F., & Beard, A. (1948). *5000 years of glass*. Philadelphia & New York: J.B. Lippincott Company.
- Santos, F. A., C., B., & Sacadura, M. (2016). Adaptive glass panels using shape-memory alloys. *Challenging Glass 5*. Ghent, Belgium.
- Schiavonato, M., Mognato, E., & Redner, A. S. (2005). Stress Measurement, Fragmentation and Mechanical Strength. *Glass Processing Days 2005*. Tampere, Finland.
- Schneider, J. (2015). Thin Glasses - A future envelope? *Conference on Building Envelopes*. Delft: TU Delft.
- SCHOTT. (2014). *Technical Glasses - Physical and Technical Properties*. SCHOTT.
- Spitzhüttl, J., Nehring, G., & Maniatis, I. (2014). Investigations on determining the bending strength of thin glass. *Challenging Glass 4 & COST Action TU0905 Final Conference* (pp. 521-530). Leiden: CRC Press/Balkema.
- Timm, C., & Chase, J. (2014). Thermally curved glass for the building envelope. *Challenging Glass 4* (pp. 141-149). Lausanne: Taylor & Francis Group.
- TNO DIANA. (2015, September and October). *DIANA Manuals*. Retrieved from <http://tnodiana.com/DIANA-manuals>.

Valarinho, L. (2010). *Comportamento estrutural de vigas mistas vifro-GFRP*. Master thesis in Civil Engineering, Instituto Superior Técnico, DECivil, Lisboa.

Valarinho, L. (2016). *Flexural Behaviour of Laminated Glass Members and Development of Glass-GFRP Composite Beams*. PhD thesis in Civil Engineering, Instituto Superior Técnico, DECivil, Lisboa.

Vallée, T., R. Correia, J., & Keller, T. (2006). Probabilistic strength prediction for double lap joints composed of pultruded GFRP profiles - Part II: Strength prediction. *Composites Science and Technology*, 66, 1915-1930.

Vandebroek, M. (2014). *Thermal Fracture of Glass*. Gent & Antwerpen: Universiteit Gent & Universiteit Antwerpen. PhD thesis in Civil Engineering.

Wiederhorn, S. M. (1971). *Environmental Stress Corrosion Cracking of Glass*. Washington: National Bureau of Standards.

Wilcox, D. I., Akarapu, R. K., Gulati, S. T., Widjaja, S., & Antimonov, M. (2013). 63.1: Biaxial Stress in Thin Glass during Ring-on-Ring Testing with Large Deflections. *SID Symposium Digest of Technical Papers*, 874–876.

Appendix

A. Specifications for commercial thin glass

A.1. AGC Leoflex™ glass

Technical specifications

LEOFLEX™

	Clear float glass (with thermal tempering)		Leoflex™ (with chemical tempering)				
	3 mm	4 mm	0.55 mm	0.85 mm	1.1 mm	1.3 mm	2 mm
Weight (kg/m ²)	7.5	10.0	1.4	2.1	2.7	3.2	5.0
Max Compressive Strength (MPa)	max 150	max 150	> 800	> 800	> 800	> 800	> 800
Compressive marginal stress (MPa)	80	80	260	260	260	260	260
Theoretical min radius curvature* (mm)	1500	2000	90	130	170	200	400
Vickers Hardness	527	527	673	673	673	673	673
Ug value EN 673 (W/m ² .C)	5.79	5.76	5.87	5.86	5.85	5.84	5.82
Light transmission EN 410 (D65.2°) LT %	90.3	89.8	91.3	91	90.8	90.6	89.9
Solar energy transmission EN 410 (D65.2°) TE %	85.7	84.4	91.6	91.5	91.4	91.3	91
Solar Factor EN 410 (D65.2°) SF %	87.5	84.9	91.7	91.6	91.5	91.4	91.2

(*) approx. value, depending on application

Processing options

Safety	Laminating (PVB or EVA), after chemical tempering
Cutting	Straight or circular, before and after chemical tempering
Shaping and edge finishing	Edge grinding (chamfering), before and after chemical tempering
	Grinding, before chemical tempering
	Drilling, before and after chemical tempering
Special treatments	Acid-etching, before and after chemical tempering
	Silk screen printing, after chemical tempering
	Painting and silvering, after chemical tempering
	Cold bending, after chemical tempering
Insulated glazing units	Double or triple glazing

NOTE: Some glass treatments are subject to limitations and must be carried out in specific conditions. Please contact AGC for more information (see contact details at the back).

Figure A-1 Technical specifications for Leoflex™ glass produced by AGC
(source: AGC Leoflex technical specifications)

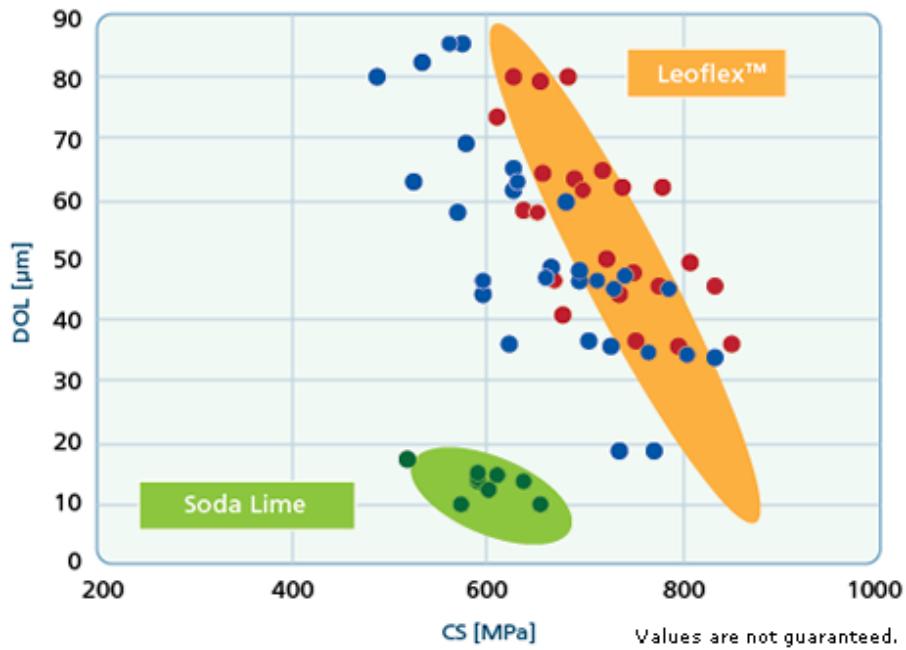


Figure A-2 - Detail of AGC Leoflex brochure: Depth of Layer (DOL) vs. compressive stress (CS)
(source: AGC Leoflex brochure)

Material Properties:

	Property	Measurement	Leoflex™	Soda Lime
Mechanical	Density	g/cm ³	2.48	2.50
	Young's Modulus	GPa	74	73
	Shear Modulus	GPa	30	30
	Poisson's Ration		0.23	0.21
	Vickers Hardness	before CT	595	533
	Vickers Hardness	after CT	673	580
Thermal	CTE	[10 ⁻⁷](50~200°C)	98	85
	Tg	°C	604	550
	Softening Point	°C	831	733
	Annealing Point	°C	606	554
	Strain Point	°C	556	511
Optical	Refraction Index	Nd	1.51	1.52
	Photoelastic Constant	nm/cm Mpa	28.3	25.6
Electrical	Volume Resistivity	log (Ω * cm)	8.4	8.5

Figure A-3 – Detail of AGC Leoflex brochure: material properties
(source: AGC Leoflex brochure)

A.2. SCHOTT Xensation® glass

SCHOTT Xensation® Cover

SCHOTT's chemically strengthened alumino-silicate glass for innovative glazing solutions

Thermal Properties	
Thermal Conductivity $\lambda_{(25\text{ °C})}$	0.96 W/(m·K)
Specific Heat Capacity $C_{p(20\text{ °C}, 100\text{ °C})}$	0.84 KJ/(Kg·K)
Coefficient of Mean Linear Thermal Expansion $\alpha_{(20\text{ °C}, 300\text{ °C})}$	$8.8 \cdot 10^{-6} \text{ K}^{-1}$ *
Transformation Point Tg	615 °C*
Annealing Point (10^{13} dPas)	635 °C
Softening Point ($10^{7.6}$ dPas)	880 °C
Working Point (10^4 dPas)	1265 °C

* cooled according to DIN

Chemical Properties		
Hydrolytic Resistance	DIN ISO 719	Class HGB 1
Acid Resistance	DIN 12116	Class S 4
Alkali Resistance	DIN ISO 695	Class A 1

Optical Properties			
Refractive Index at	588 nm (n_d)	633 nm	780 nm
Core Glass	1.508	1.506	1.502
Compression Layer			
KNO ₃ pure	1.516	1.514	1.510
Transmittance τ (Glass Thickness 0.7 mm)			
840 nm			> 91.5 %
560 nm			> 91.5 %
380 nm			> 90 %
Photoelastic Constant			29.2 nm/cm/MPa

Sheet Dimensions	
Sheet Size*:	1150 x 950 mm
	475 x 575 mm
Thickness Range:	0.5 - 3.0 mm

* other sizes on request

Mechanical Properties	
Density	2.477 g/cm ³ *
Young's Modulus E	74 kN/mm ²
Poisson's Ratio	0.215
Shear Modulus	30 kN/mm ²
Knoop Hardness HK _{0.1/20}	
Non-strengthened	534
Strengthened	639
Vickers Hardness HV _{0.2/20}	
Non-strengthened	617
Strengthened	681

* cooled according to DIN

Chemical Strengthening	
Compressive Stress	capable > 900 MPa
Depth of Layer	capable > 50 μ m
4-Point Bending Strength	cap. > 800 MPa

Figure A-4 – Technical specifications for Xensation® glass produced by SCHOTT
(source: SCHOTT Xensation® technical specifications)

B. SCALP – Preliminary tests

Prior to the testing presented in this report, an extensive set of preliminary tests was carried out to understand the influence of all the conditions that could impact the results. Hereby, this set is presented with the methodology and results attained.

The *GlasStress* SCALP software has a fairly simple interface and help section, but is quite vague in the description of the effects of each test option it provides. In addition, the stress readings obtained were very unreliable and unstable since the very beginning. In fact, the polariscope was sent to *GlasStress* company for calibration after some inconsistent test results were retrieved; in this document, all studies and results presented were done after calibration. Therefore, a considerable amount of time was spent on 1) understanding the influence of the software parameters and 2) assessing the influence of the testing conditions. This section explains these two sets of preliminary tests and the measures available to assess and validate the readings; the final part presents a test of one of the parameters.

Regarding the software parameters, the following input is required from the user: gain, measurement depth, measurement time (3 seconds by default), background (“very noisy” by default), fit method (“chemical”) and fit closeness (0,5 by default). Then, other parameters depend on the properties of the glass and are, thus, previously defined: refraction index ($RI = 1,508$), photoelastic constant ($C = 2,92 \text{ TPa}^{-1}$) and thickness (depending on glass). Only the study of the influence of gain is described in this document, as an example, but all the remaining parameters were investigated.

Concerning the testing conditions, several options were experimented, namely the following: room lights on and off; different amounts of immersion liquid on the thin glass; immersion liquid on both surfaces of the glass; glass plate in contact with the background or supported on small wood pieces; cleaning the surface of the thin glass and of the periscope with alcohol or immersion liquid; edge of the thin glass dry or wet with immersion liquid, and direction of the laser.

A very useful tool to adjust those parameters is the live video. The option *DigInt* “*activates the laser beam intensity curve on video overlay that may be used to evaluate the gain level, the size of saturated entrance/exit spots*”, as described in the software manual (*GlasStress Ltd, 2013*). This option is useful to further assess the distortion around the critical spots besides the simple video evaluation and to make the corrections before the reading (the red parallel lines indicate if the laser ray is intense enough to be recognized by the software). Figure B-1 presents an example of a very clear reading, very hard to get. It was through this tool that the refractive index was adjusted from 1,51 (specified in the product sheet, (*AGC, 2012*)) to 1,508: for this last value, the green line matched the true exit of the beam as the figure shows, while for 1,51 it was visibly off.

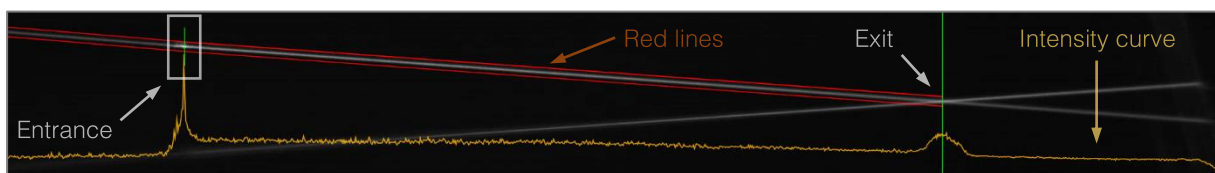


Figure B-1 - Screenshot of the video of reading 27 of Full-Length test, with *DigInt* activated [edited with +40% brightness]

Other measures for validation and calibration of the readings are the fit error and the percentage of excluded pixels. The fit error is the root-mean-square error of the fitting curve over measured retardation distribution and it is indicated that a good value is below 10; less than 20% of excluded pixels is considered as a good reading (GlasStress Ltd, 2013).

Finally, the preliminary tests were important to understand the influence of the different parameters and to set the values to be used in the software. These tests showed that most of the testing conditions had no or little relevance on the results. One of the many tests was performed to understand the influence of Gain, as soon it became evident that it was an important input option for which there were no guidelines in terms of values. With everything else constant, 20 measurements per value of gain were made on the same place, without ever touching the periscope. The choice of the Gain is also very important to achieve a proper intensity curve. The experimental results obtained are presented in Table 12. Two values of gain were highlighted from the test on position A¹³ for further studies: 25, which provided the minimum value of surface stress and the lowest value of fit error; and 75, for which the maximum value of surface stress and the lowest of standard deviation were obtained. However, in the following tests conducted in other positions, B and C depicted as examples, the influence was no longer clear. Therefore, the value was set to 25 as it presented a less saturated intensity curve in the critical points.

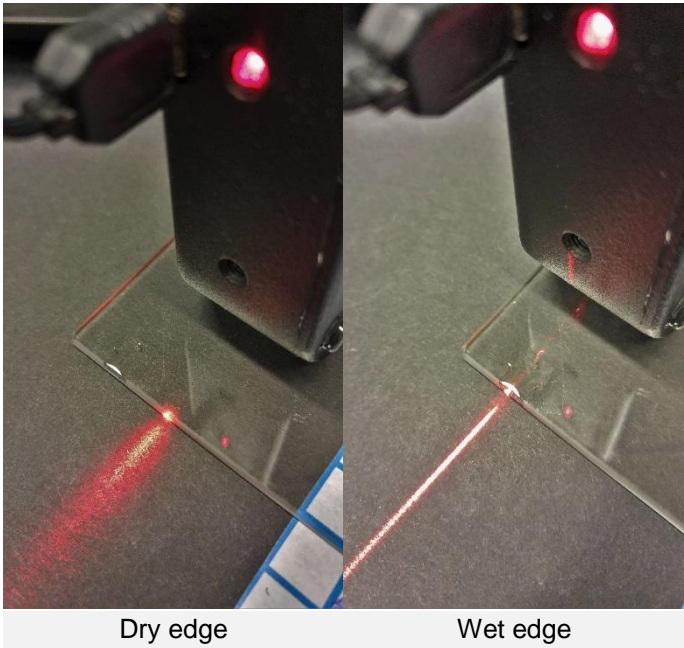


Figure B-2 – Comparison of dispersion of the laser with the dry edge and with immersion liquid on the edge

¹³ Positions A, B and C are arbitrary and are not specified as the focus of the test is the influence of a Gain; factors related to the position are constant among the different tests and therefore do not have influence

Table 12 – Results of SCALP with varying gain

#	Gain	Surface stress (MPa)	Standard dev. (MPa)	Fit Error ¹⁴ (MPa)	Excluded Pixels
A	5	-148,8	3,8	3,1	0%
	25	-143,5	8,4	2,2	0%
	50	-159,2	6,0	3,9	1%
	75	-168,2	3,3	3,1	0%
	100	-160,8	10,3	3,9	1%
B	25	-114,8	1,9	2,7	2%
	75	-118,0	2,4	3,4	0%
C	25	-114,8	3,3	2,3	2%
	75	-110,5	2,7	2,3	1%

Testing conditions: dim light on, dry edge, new glass plate, SCALP cleaned with alcohol, black background, normal amount of immersion liquid, position for test A is 10 cm from bottom edge, centred, and laser pointing to the furthest top.

Software parameters: measurement depth of 2,00 mm, all other parameters as default (see paragraphs above), 20 measurements.

To conclude this section, Table 13 presents some general findings that the preliminary tests revealed. It is important to note that the results always varied significantly and many factors were hard to control, making it difficult to draw solid/definitive conclusions.

Table 13 – Indications from the preliminary tests regarding testing conditions

Testing conditions	Influence
Cleaning of SCALP and glass	Upmost importance to guarantee a valid reading. A good cleaning is hard to achieve, particularly in the surface of the prism.
Dry or wet edge of glass	Wetting the glass edge lowers slightly the fit error: as an example, with a gain of 25, an error of 3.0 with a dry edge was reduced to 2.3 after wetting it. More tests showed some consistency in this trend. It is observable that the liquid on the edge helps the laser beam exit the glass with far less dispersion (see appendix B).
Amount of immersion liquid applied	Thin indication that lower amounts of liquid can lead to higher stresses. Very hard to test with certainty as many factors can play a role in this observation, from volume of liquid to spread on the surface. It can be that less liquid caused a worse transmission of the laser beam, resulting in a worse reading with higher values.
Direction of the laser	Seems to have little influence if the edge is too close due to reflections.
Two sides of the plate (tin and air side)	No significant difference.
Lights on or off	No significant difference.
Physical background ¹⁵	No significant difference.

¹⁴ Root-mean-square error of the fitting curve over measured retardation distribution (GlasStress Ltd, 2013)

¹⁵ Refers to tests with white or black background and also tests carried out with the glass plate simply supported so that the bottom surface was not in contact with the background

C. In-plane four-point bending test

C.1. Detailed analysis of the results for the first millimetres of deformation

Figure C-1 shows the raw force vs. cross-head displacement curves obtained in the four-point bending test, from which Figure 46 was produced (see 0). Figure C-2 depicts a detail of the first 4 mm and 50 N, showing the cyclic loading and how the glass is much more unstable than the aluminium samples. As referred in section 0, both figures reveal that the effectiveness of the load in creating a sustained displacement depends on the constraint degree of the sample (except for the glass sample).

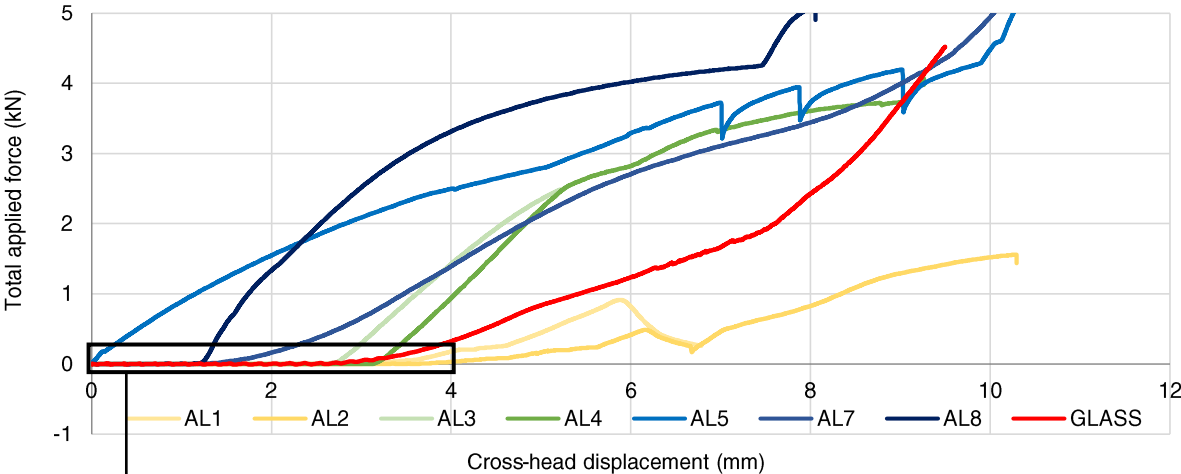


Figure C-1 – Raw force-displacement graph of the in-plane four-point bending preliminary tests

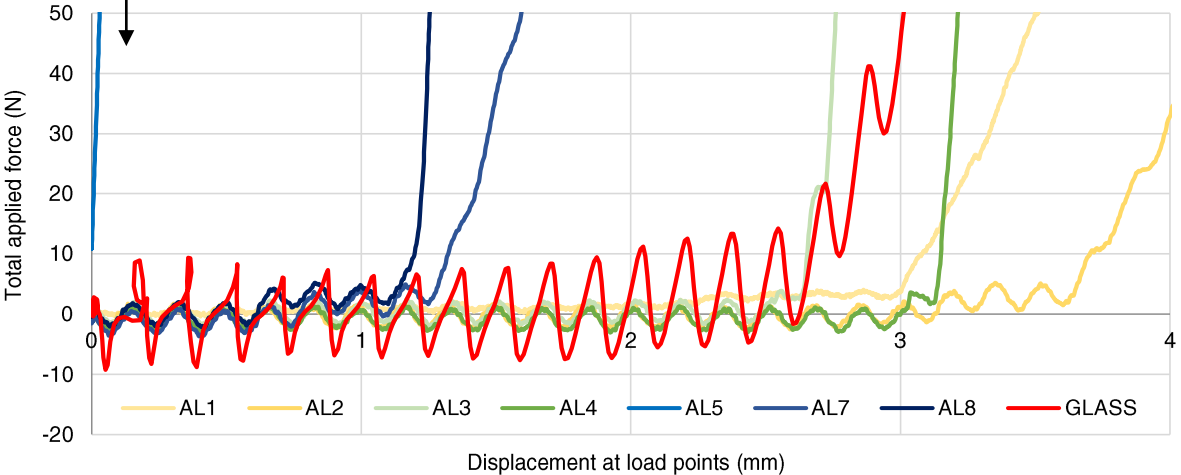


Figure C-2 – Detail of the raw force-displacement graph of the in-plane four-point bending preliminary tests

C.2. Numerical analysis with single line of nodes as lateral support

In the numerical analyses carried out to study the lateral torsional buckling (see 5.2.3 5.2.3.3), the supports constraining the out-of-plane deformation were modelled with two lines of nodes constrained instead of only a single line. To justify this decision, a new model was used for another three tests. Figure C-3 shows the model C, which is a derivation of model A obtained by removing one line of constrained nodes.

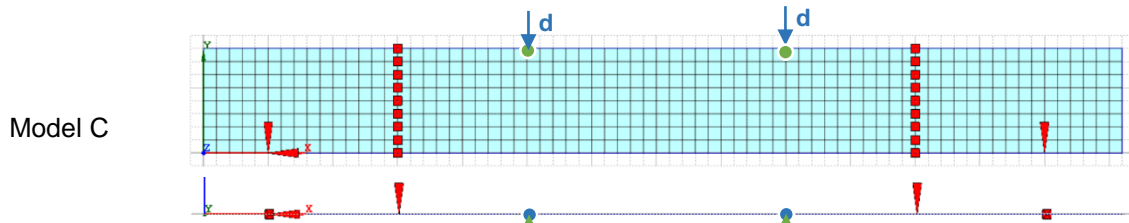


Figure C-3 – Model with shell elements with supports in the out-of-plane direction, side and top view: only outer supports in one line of nodes

The three tests carried out were: “Aluminium 150MPa”, “Glass, no side force” and “Glass, with side force”, all modelled with shell elements. The first two tests consisted of applying a vertical displacement at the load points without any imperfection. The former introduced an out-of-plane total force of 1 N proportional to the displacement to replicate an eccentric loading, similar to what was done in the analyses 2 and 3 presented in section 5.2.3. Figure C-4 illustrates the results of these numerical analyses and already illustrates the problem of having only one line of nodes as supports constraining the out-of-plane deformation: the curvature is almost constant over the whole length and the supports work as an axis, not limiting the rotation at all.

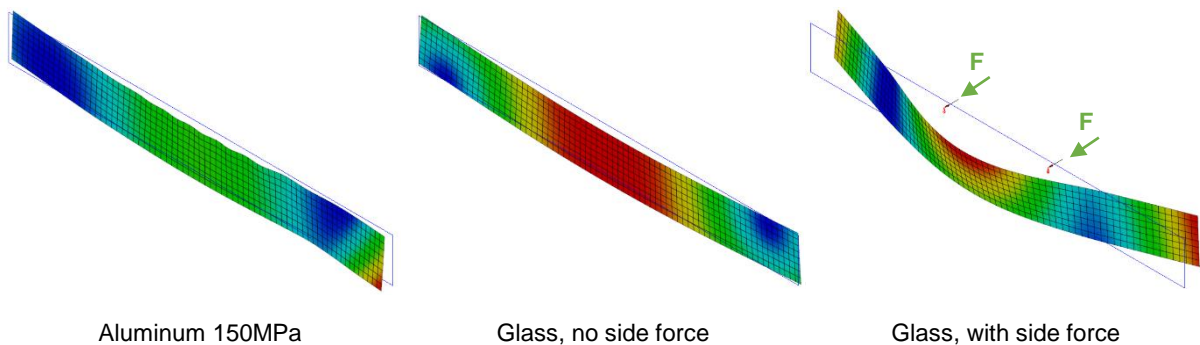


Figure C-4 – Absolute displacement for 100mm of vertical displacement at loads (TDtXYZ) [analysis 1,2,3]

Finally, Figure C-5 compares these three analysis with the analysis of Aluminium AL150 modelled with plane stress elements and assuming no lateral torsional buckling (5.2.3) to highlight the differences. The graph clearly reveals the consequences of allowing the rotation in the supports: the glass with no side force behaves linearly, as expected; however, when a small out-of-plane force is applied, the glass buckles almost instantaneously. Concerning the aluminium, while for the first 7 mm the behaviour is identical, then the force applied drops for the analysis with shell elements.

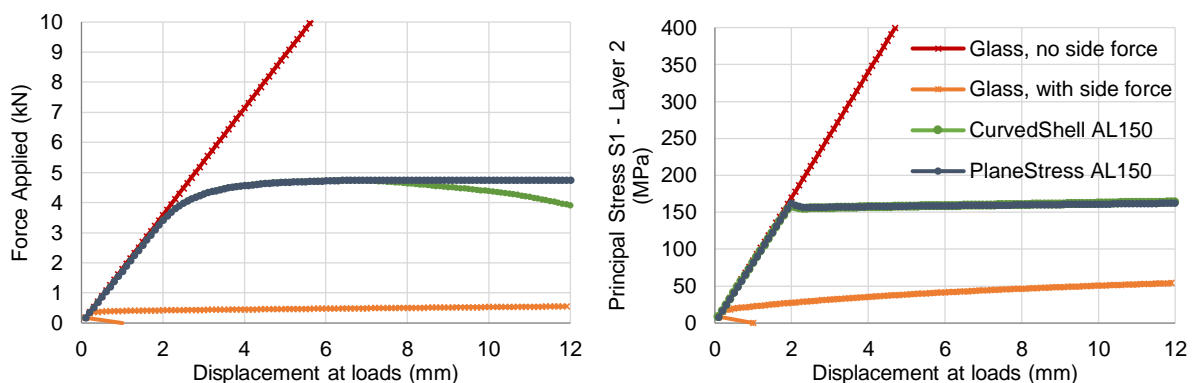


Figure C-5 – Applied force and principal stresses vs. vertical displacement at loads for different finite elements, materials and loads applied

C.3. Numerical analysis of lateral instability with aluminium – setup 3

The final numerical analysis carried out to study the lateral instability, analysis 4 (see 5.2.3), was repeated with aluminium AL150 instead of glass, but only for the case of 1 N of out-of-plane force applied. Figure C-6 shows the three layers of the shell element and the stresses developed after yielding. Figure C-8 presents the principal stresses vs. the vertical displacement at loads, where yielding is very clear. As the sections are the same and the Young's moduli are very similar, it can be concluded that the yielding precedes the buckling. Indeed, when the glass was tested it only buckled when a displacement of over 5 mm was reached (see Figure 63).

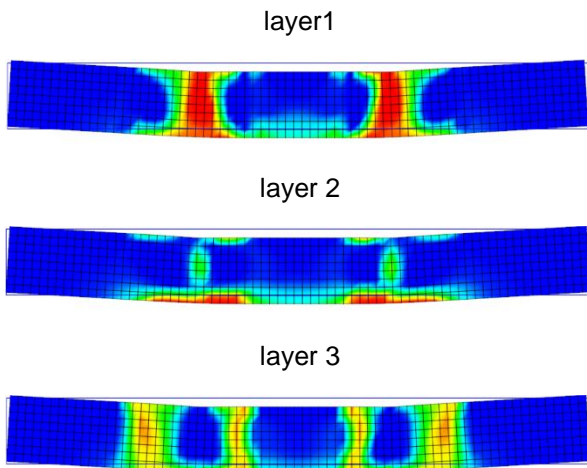


Figure C-6 – Distribution of the principal stress for the three layers of the shell element at 100 mm of displacement

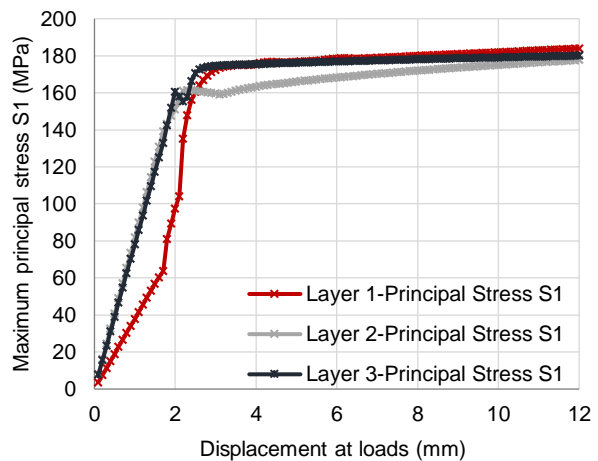


Figure C-7 – Principal stress for the three layers of the shell element vs. vertical displacement at loads

Figure C-8 shows that the applied force only reached 3 kN before yielding when, in the case of glass, it was above 9 kN when it buckled (Figure 65).

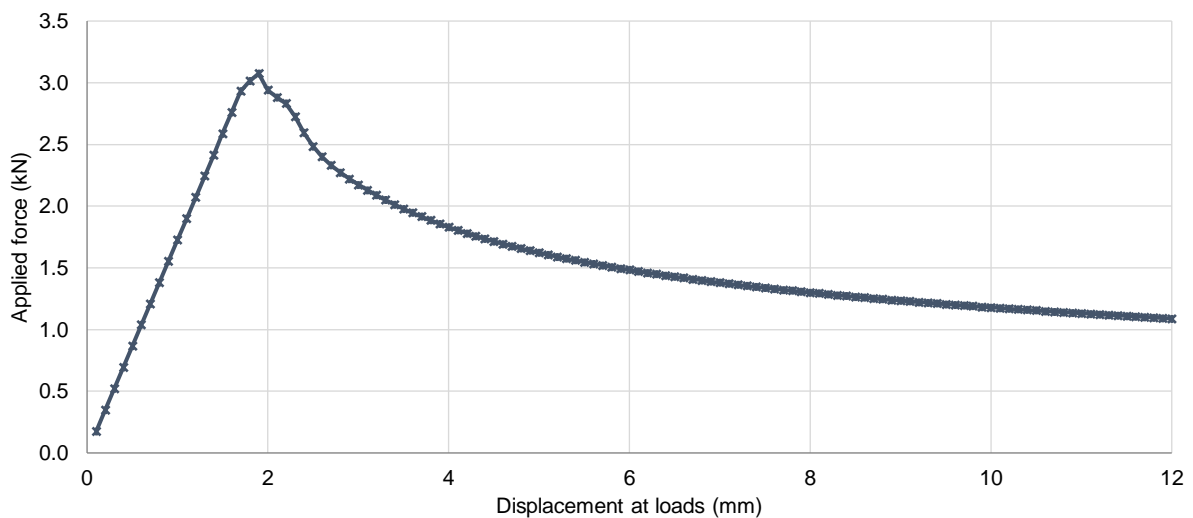


Figure C-8 – Applied force vs. displacement at loads for aluminium

D. Buckling test

D.1. Detailed analysis on the first millimetres

A very important part of the instability analysis is the moment when the instability starts. In the graph presented in Figure 74 (see 5.3.4) the global behaviour of the tests is shown. The graph in Figure D-1 is restricted to the first 4 mm of vertical displacement and from 60 N to 100 N of applied force, highlighting the area where instability starts. A series of sudden drops in the force is visible, probably resulting from adjustments of the glass plate inside the slit.

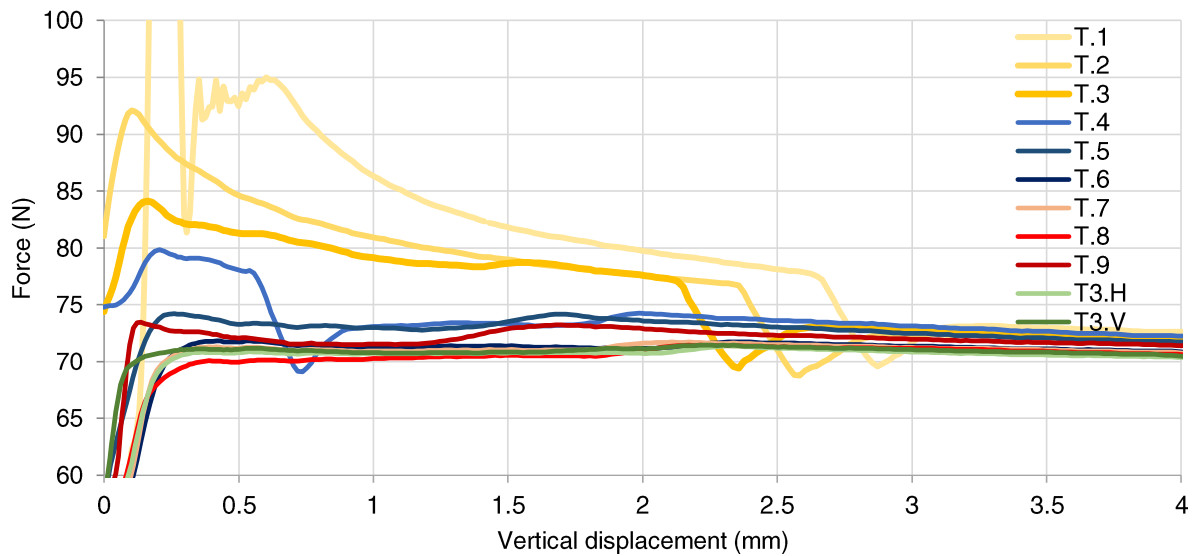


Figure D-1 – Detailed analysis on buckling: first millimetres of vertical displacement (instability)

Also for the numerical analysis (see 5.3.5), Figure D-2 draws attention to the beginning of the instability and compares it with the experimental results (detail of Figure 89). This graph focused on such a small interval of applied force making visible a very slight drop in the force applied at a point with an amplitude below 1 N.

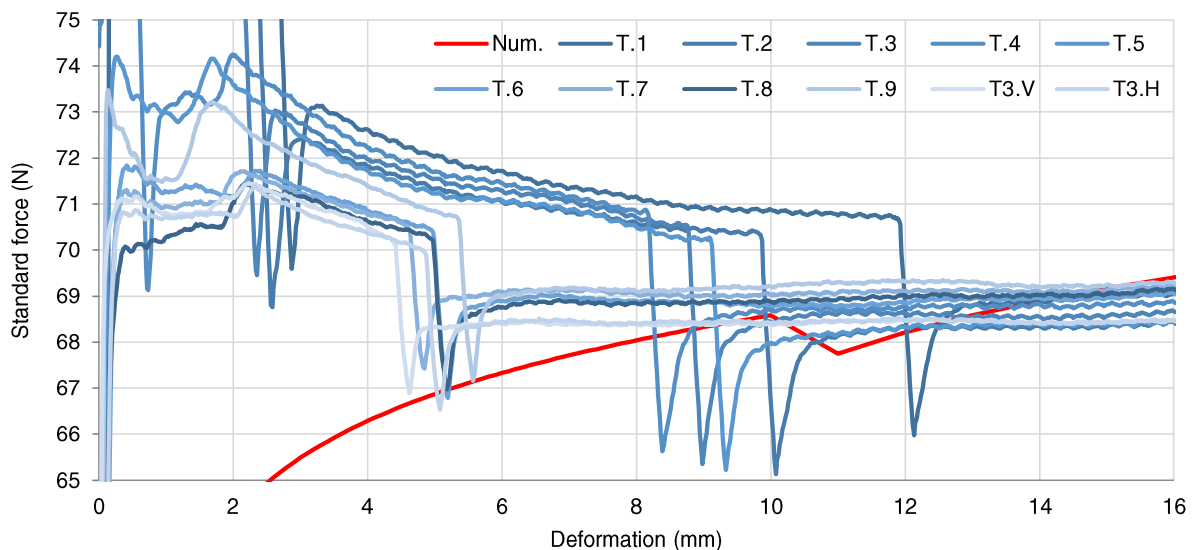


Figure D-2 – Detailed analysis on buckling: first millimetres of vertical displacement with numerical analysis

D.2. Video frames of the buckling test

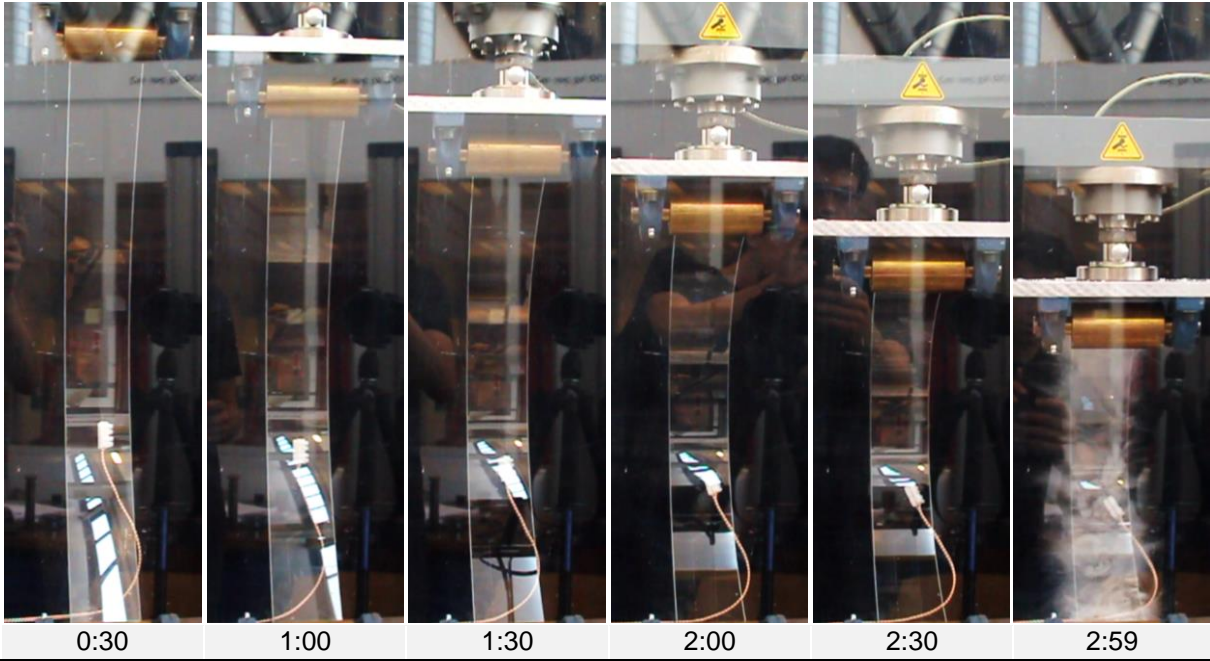


Figure D-3 – Behaviour and collapse of glass – front view [camera 1]

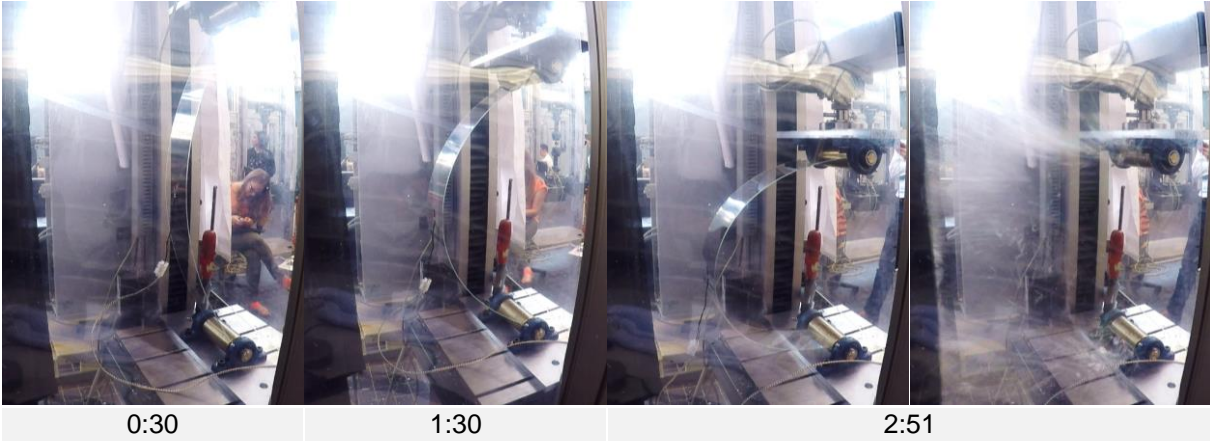


Figure D-4 – Behaviour and collapse of glass – side view [camera 2]

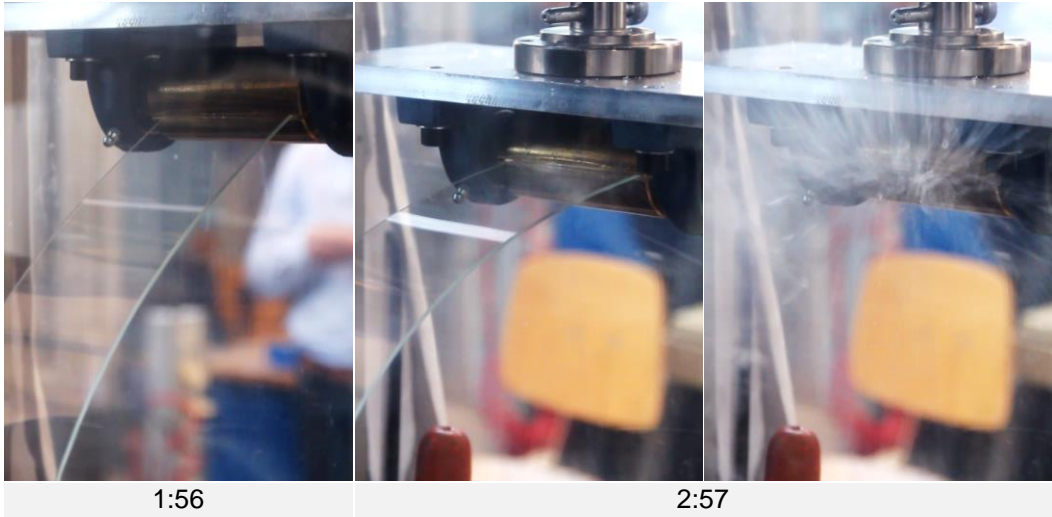


Figure D-5 – Behaviour and collapse of glass – top roller [camera 3]

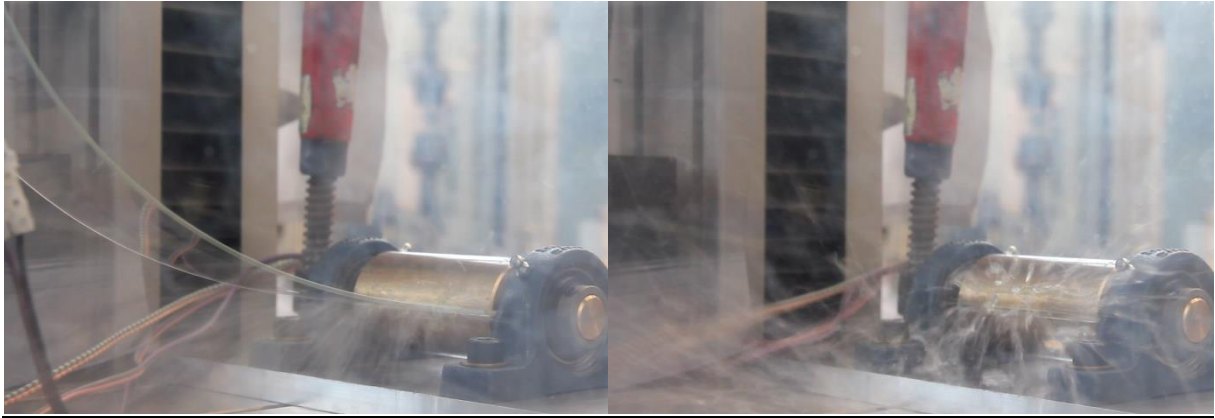


Figure D-6 – Collapse of glass – bottom roller [camera 4]

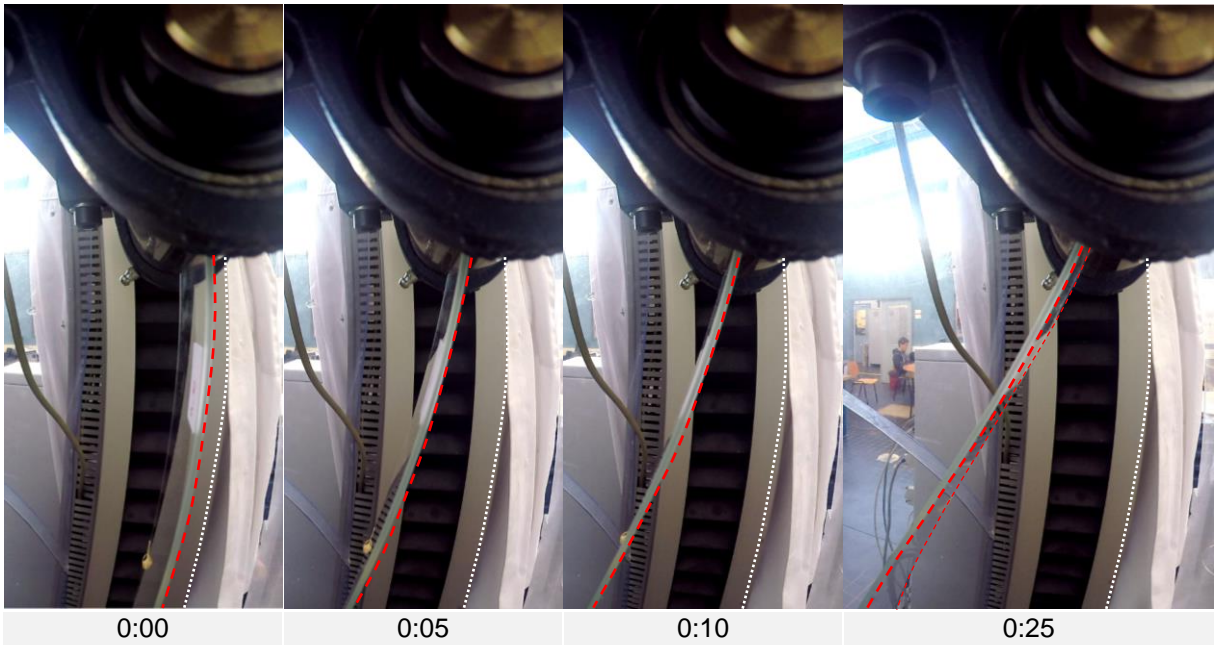


Figure D-7 – Original frames of GoPro video focusing on top roller - first seconds (fisheye effect not-corrected) [camera 5]

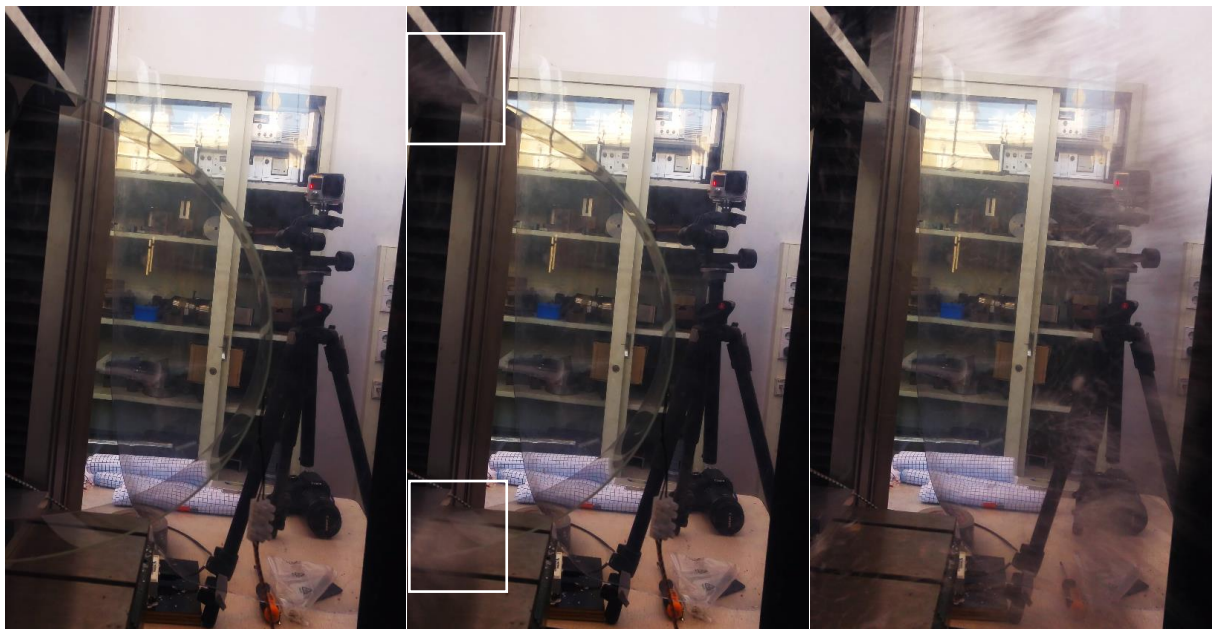


Figure D-8 – Collapse of the glass – visible the start at the rollers in the centre picture [camera: LG G4]

E. Tension test

E.1. Glass adhesives: DYMAX Ultra Light-Weld® 431



Ultra Light-Weld® 431 High-Temperature and Moisture-Resistant Glass-to-Metal Bonding Adhesive

UNCURED PROPERTIES *		
Property	Value	Test Method
Solvent Content	No Nonreactive Solvents	N/A
Chemical Class	Acrylated Urethane	N/A
Appearance	Colorless Transparent Liquid	N/A
Soluble in	Organic Solvents	N/A
Density, g/ml	1.04	ASTM D1875
Viscosity, cP (20 rpm)	500 nominal	ASTM D1084

CURED MECHANICAL PROPERTIES *		
Property	Value	Test Method
Durometer Hardness	D70	ASTM D2240
Tensile at Break, MPa [psi]	27 [3,900]	ASTM D638
Elongation at Break, %	61	ASTM D638
Modulus of Elasticity, MPa [psi]	570 [82,000]	ASTM D638
Tensile Compression Shear, MPa [psi]	—	—
Glass-to-Glass	31 [4,500]	DSTM D250 [‡]
Glass-to-Stainless Steel	23 [3,300]	DSTM D251 [‡]

OTHER CURED PROPERTIES *		
Property	Value	Test Method
Refractive Index (20°C)	1.50	ASTM D542
Boiling Water Absorption, % (2 h)	4.4	ASTM D570
Water Absorption, % (25°C, 24 h)	1.5	ASTM D570
Linear Shrinkage, %	0.78	ASTM D2566
Glass Transition T _g , °C	115	ASTM E831

* Not Specifications
 N/A Not Applicable
 ‡ DSTM Refers to Dymax Standard Test Method

ADHESION	
Substrate	Recommendation
ABS acrylonitrile-butadiene-styrene	✓
CAP cellulose acetate propionate	✓
PA polyamide	✓
PC polycarbonate	✓
PCTG poly(cyclohexylene dimethylene terephthalate)glycol	✓
PEBA polyether block amide	✓
PEEK polyetheretherketone	✓
PET poly(ethylene terephthalate)	✓
PETG poly(ethylene terephthalate)glycol	✓
PI polyimide	✓
PVC poly(vinyl chloride) (Rigid and Flexible)	✓
SAN styrene-acrylonitrile	✓
Ceramic	✓
Glass	✓
Aluminum	✓
Stainless Steel	✓
Copper	✓
Brass	✓
FR-4	✓

✓ Recommended Adhesive o Limited Applications
 st Requires Surface Treatment (e.g. plasma, corona treatment, etc.)

DEPTH OF CURE

The graphs below show the increase in depth of cure as a function of exposure time with two different lamps at different intensities. A 9.5 mm [0.37 in] diameter specimen was cured in a polypropylene mold and cooled to room temperature. It was then released from the mold and the cure depth was measured. These depths are only due to light cure.

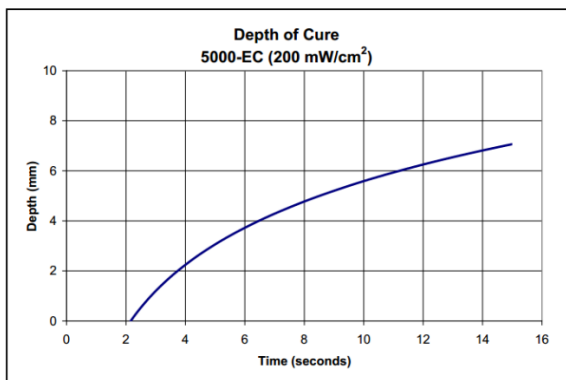


Figure E-1 – Product datasheet for DYMAX Ultra Light-Weld® 431 (source: DYMAX)

E.2. Analysis of the principal stress in the glue

This appendix presents a complementary analysis on the principal stresses σ_1 developed on the glue.

The values of the principal stress σ_1 on the centre (C) and on the edge (E) for the six points presented in Table 11 were plotted over a profile of 60 mm starting from the top of the glass plate and for Poisson's ratios of 0,29 (Figure E-2) and 0,48 (Figure E-3).

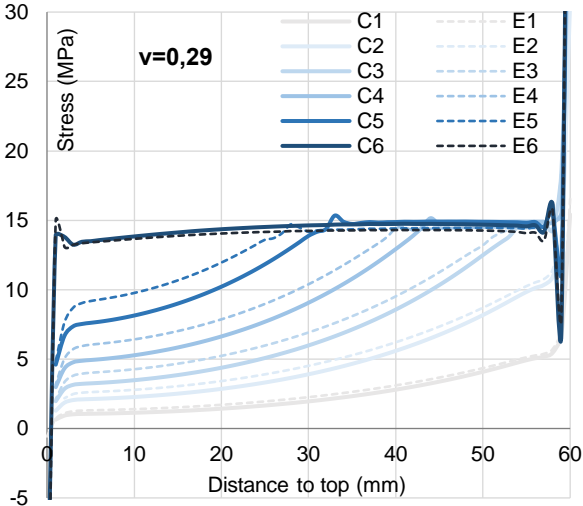


Figure E-2 – Evolution of centre (C) and edge (E) principal stresses in the glue, vertical profile (Poisson ratio=0,29)

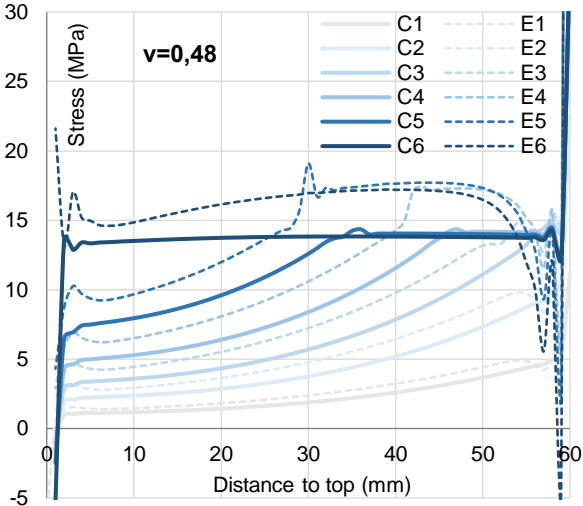


Figure E-3 – Evolution of centre (C) and edge (E) principal stresses in the glue, vertical profile (Poisson ratio=0,48)

The graphs are somewhat different from those presented in 5.4.2. It is clear that the principal stress distribution is rather different: while for $v=0,29$ the centre stress is always bigger than the edge stress, for $v=0,48$ the opposite happens. In fact, it is confirmed that the larger the difference between the Poisson's ratio of the glue and glass the more significant the concentration of stresses near the edges are. It is also interesting to notice that the stresses do not reach a yielding plateau as the shear stresses, but still display some curvature and the edge stresses for $v = 0,48$ surpass that value.

One obvious particularity is the fact that the nodes at the extremes present very significant stress peaks. Figure E-4 illustrates the reason for that: besides shear stresses and the geometrical singularity, those nodes are subjected to other stresses, namely peeling stresses.

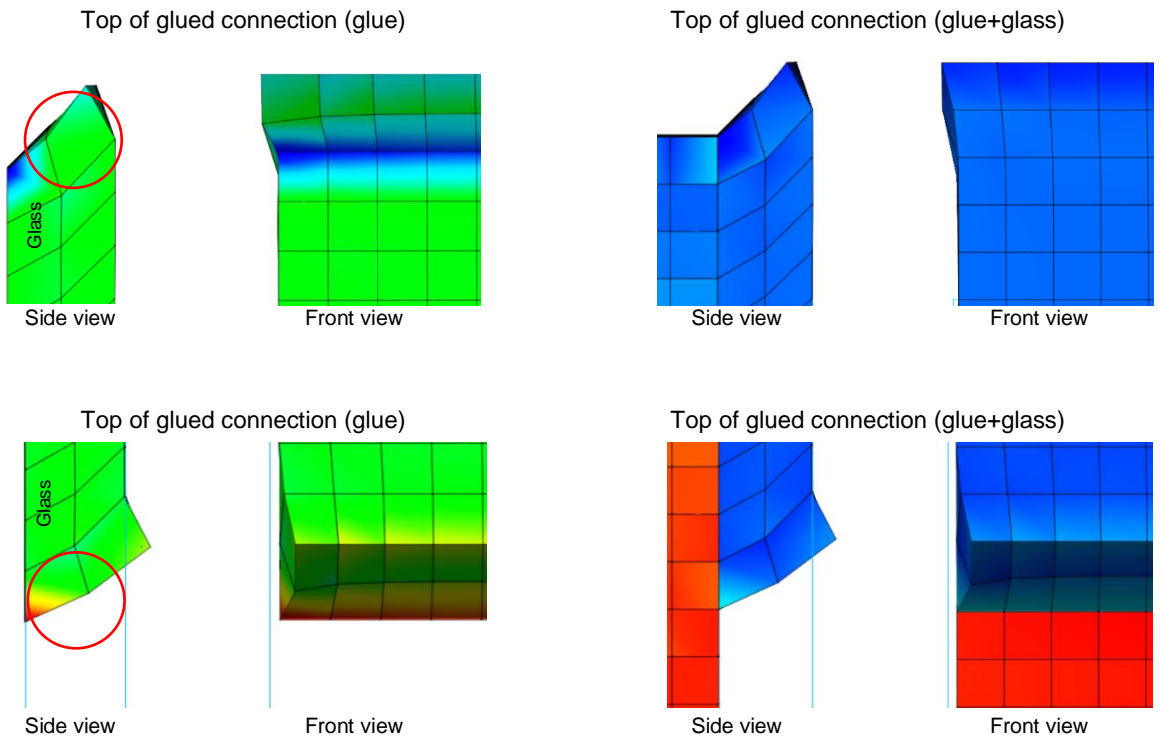


Figure E-4 – Detail of the first nodes of the glued connection ($d=60\text{mm}$) revealing very high values of stress (plot $v=0,29$)